

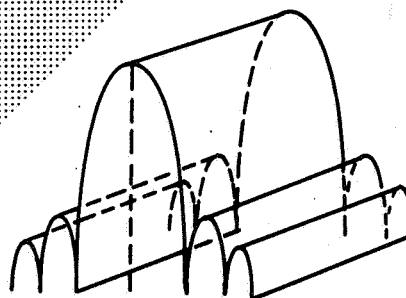
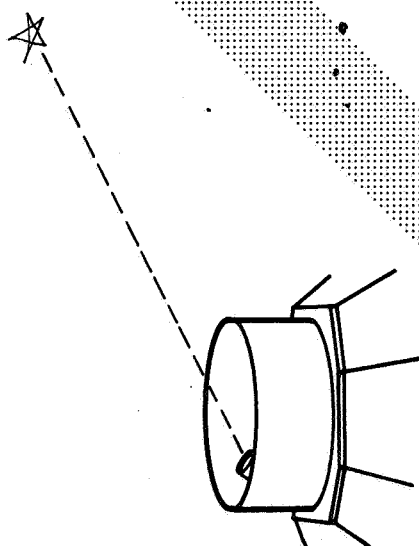
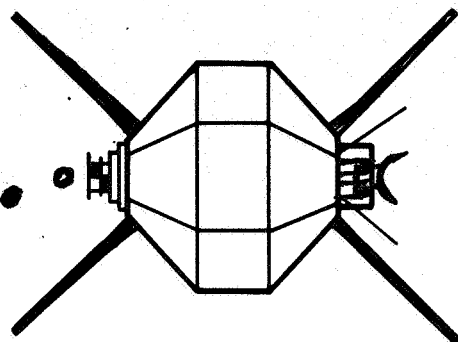
13 JULY 1966

WDL-TR2962
VOLUME V
EXPERIMENT

Ni

FAN BEAM NAVIGATION SATELLITE STUDY

157A
2B
NASA CR-85003



FACILITY FORM 602
N67-31433
(ACCESSION NUMBER)
162
(PAGES)
CR-85003
(NASA CR OR TMX OR AD NUMBER)

(THRU)
1
(CODE)
21
(CATEGORY)

CONTRACT
NUMBER
NASW-1368

Submitted to

HEADQUARTERS NATIONAL AERONAUTICS AND SPACE ADMINISTRATION
WASHINGTON, D.C.

PHILCO. | WDL DIVISION
A SUBSIDIARY OF Ford Motor Company | PALO ALTO-CALIFORNIA
HOUSTON-TEXAS

807 44232

WDL TECHNICAL REPORT 2962
FAN BEAM NAVIGATION SATELLITE STUDY

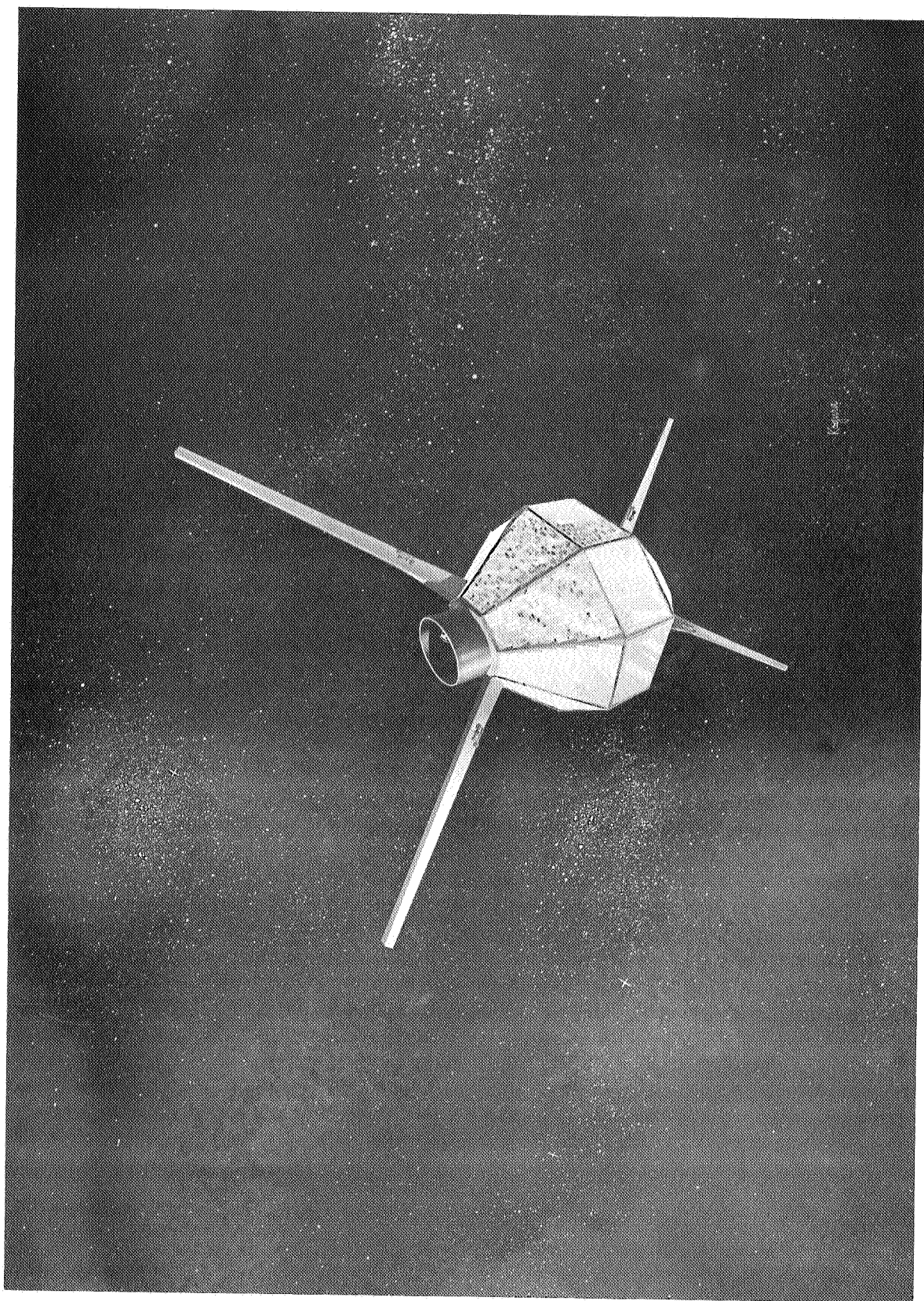
Volume V
PROGRAM PLAN FOR A
FAN BEAM NAVIGATION TEST SATELLITE

13 July 1966

Contract No. NASW-1368

Submitted to:
Headquarters
National Aeronautics and Space Administration
Washington, DC

Prepared by
PHILCO CORPORATION
A Subsidiary of Ford Motor Company
WDL Division
Palo Alto, California



CONTENTS

| <u>Section</u> | | <u>Page</u> |
|----------------|--|-------------|
| 1 | SYSTEM DESCRIPTION AND PROGRAM SUMMARY | 1-1 |
| 1.1 | General Description | 1-2 |
| 1.1.1 | Program Task | 1-3 |
| 1.1.2 | Program Requirements | 1-6 |
| 1.2 | Program Objectives | 1-6 |
| 1.2.1 | General | 1-6 |
| 1.2.2 | Primary Mission Objectives | 1-6 |
| 1.3 | Predicted Performance | 1-8 |
| 2 | PROGRAM PLAN | 2-1 |
| 2.1 | Satellite Development | 2-1 |
| 2.2 | Launch Vehicle | 2-1 |
| 3 | DESIGN CONCEPTS | 3-1 |
| 3.1 | Antenna Design | 3-1 |
| 3.1.1 | Antenna Structural Analysis | 3-1 |
| 3.1.1.1 | Introduction | 3-1 |
| 3.1.1.2 | Analysis | 3-1 |
| 3.1.2 | Satellite/Antenna Integration | 3-11 |
| 3.1.2.1 | Mechanical Design | 3-11 |
| 3.1.2.2 | Satellite/Antenna Configuration | 3-13 |
| 3.1.3 | Antenna Electrical Design | 3-20 |
| 3.2 | Star Detector Design | 3-27 |
| 3.2.1 | NavSat Star Detector System | 3-27 |
| 3.2.2 | Details of Design and Construction | 3-33 |
| 3.2.2.1 | Optical System | 3-33 |
| 3.2.2.2 | Assembly | 3-35 |
| 3.2.2.3 | Detector and Signal Processing | |
| | Electronics | 3-36 |
| 3.2.2.4 | Command and Other Electronics | 3-41 |
| 3.2.3 | Calibration Testing | 3-44 |
| 3.2.4 | Installation Checkout | 3-46 |

CONTENTS (Continued)

| <u>Section</u> | | <u>Page</u> |
|----------------|--|-------------|
| 3.3 | Nutation Damper Integration | 3-49 |
| 3.4 | Electrical System Design | 3-54 |
| 3.4.1 | Introduction | 3-54 |
| 3.4.2 | Design Requirements and Constraints | 3-54 |
| 3.4.2.1 | Design Requirements | 3-54 |
| 3.4.2.2 | Operational Modes | 3-57 |
| 3.4.3 | Basic Electrical System Description | 3-59 |
| 3.4.3.1 | Power Subsystem | 3-59 |
| 3.4.3.2 | Fan Beam Transmission System | 3-62 |
| 3.4.3.3 | Command Subsystem | 3-67 |
| 3.4.3.4 | Telemetry Subsystem | 3-68 |
| 3.4.3.5 | Star Detector Subsystem | 3-71 |
| 3.4.3.6 | Event Timer | 3-80 |
| 3.4.4 | Electrical System Performance | 3-81 |
| 3.4.4.1 | Introduction | 3-81 |
| 3.4.4.2 | Fan Beam Transmission Subsystem | 3-81 |
| 3.4.4.3 | Telemetry Subsystem | 3-83 |
| 3.4.4.4 | Star Detector Subsystem | 3-86 |
| 3.4.4.5 | Command Subsystem | 3-86 |
| 3.4.5 | Power Management | 3-91 |
| 3.4.5.1 | Solar Array Performance | 3-31 |
| 3.4.5.2 | Battery Performance | 3-94 |
| 3.4.5.3 | Charge Control | 3-100 |
| 4 | MISSION PLAN | 4-1 |
| 4.1 | Experiment Plan | 4-1 |
| 4.2 | Mission Analysis | 4-2 |
| 4.2.1 | Orbit Selection | 4-2 |
| 4.2.2 | Orbit Profile | 4-7 |
| 5 | DATA HANDLING SYSTEM | 5-1 |
| 5.1 | Data Handling System Concept | 5-1 |
| 5.2 | Spin Axis Determination Using Star Detector Data | 5-3 |
| 6 | EXPERIMENT COST | 6-1 |

LIST OF ILLUSTRATIONS

| <u>Figure</u> | <u>Title</u> | <u>Page</u> |
|---------------|---|-------------|
| 1-1 | Fan Beam Navigation Experiment Satellite | 1-4 |
| 1-2 | Performance Curves Showing Accuracy vs Smoothing Times for Various Receiver Dish Sizes (Case 30, 3.2 to 25.6 Foot Dishes) | 1-12 |
| 1-3 | Performance Curves Showing Accuracy vs Smoothing Times for Various Receiver Dish Sizes (Case 30, 0.2 to 1.6 Foot Dishes) | 1-13 |
| 1-4 | Performance Curves Showing Accuracy vs Smoothing Times for Various Receiver Dish Sizes (Case 31, 3.2 to 25.6 Foot Dishes) | 1-14 |
| 1-5 | Performance Curves Showing Accuracy vs Smoothing Times for Various Receiver Dish Sizes (Case 31, 0.2 to 1.6 Foot Dishes) | 1-15 |
| 2-1 | Navigation Satellite (NETS) Program Milestone Schedule (1) - Satellite Development | 2-2 |
| 2-2 | Navigation Satellite (NETS) Program Milestone Schedule (2) - Star Detector | 2-3 |
| 2-3 | Navigation Satellite (NETS) Program Milestone Schedule (3) - Slotted Waveguides | 2-4 |
| 2-4 | Navigation Satellite (NETS) Program Milestone Schedule (4) - Nutation Damper | 2-5 |
| 3-1 | Centrifugal Loading on Boom Antenna Due to Spinning Spacecraft | 3-3 |
| 3-2 | Finite Element Approximation of Tapered Cantilever | 3-3 |
| 3-3 | Cross Section of Preliminary Honeycomb Sandwich Antenna | 3-6 |
| 3-4 | Maximum Antenna Deflection vs Antenna Length | 3-8 |
| 3-5 | Maximum Bending Stress vs Antenna Length | 3-9 |
| 3-6 | Shear Flow Distribution on Antenna Cross Section | 3-10 |
| 3-7 | Antenna Deployment Hinge | 3-12 |
| 3-8 | Satellite General Arrangement (Sheet 1 of 4) | 3-16 |
| 3-8 | Satellite General Arrangement (Sheet 2 of 4) | 3-17 |
| 3-8 | Satellite General Arrangement (Sheet 3 of 4) | 3-18 |
| 3-8 | Satellite General Arrangement (Sheet 4 of 4) | 3-19 |
| 3-9 | Schematic of Slot Arrangement for Constant Phase and Out-of-Phase Arrays | 3-23 |
| 3-10 | Cross Section of Antenna Pattern Nos. 1 and 2 | 3-24 |

LIST OF ILLUSTRATIONS (Continued)

| <u>Figure</u> | <u>Title</u> | <u>Page</u> |
|---------------|---|-------------|
| 3-11 | Cross Section of Antenna Pattern No. 3 | 3-25 |
| 3-12 | Cross Section of Antenna Pattern No. 4 | 3-26 |
| 3-13 | Star Detector Schematic | 3-28 |
| 3-14 | Solid Catadioptric Star Detector Lens | 3-29 |
| 3-15 | Typical Reticle Pattern | 3-30 |
| 3-16 | Star Detector Electronics Block Diagram | 3-37 |
| 3-17 | Star Detector Video Amplifier and Pulsed AGC Schematic | 3-38 |
| 3-18 | Star Detector Low-Voltage Converter Schematic | 3-39 |
| 3-19 | Outline Drawing of EMR Model 640C High Voltage Supply | 3-42 |
| 3-20 | Proposed Star Detector Electronics Package | 3-43 |
| 3-21 | Star Detector Calibration and Checkout Equipment | 3-45 |
| 3-22 | Schematic of a Nutation Damper | 3-50 |
| 3-23 | Damping Time History $\gamma^* = 20$ Seconds of Arc | 3-52 |
| 3-24 | Basic Electrical System Block Diagram | 3-60 |
| 3-25 | Frequency Generator | 3-63 |
| 3-26 | Traveling Wave Tube Amplifies | 3-64 |
| 3-27 | DC/DC Converter | 3-65 |
| 3-28 | DC/DC Converter (rear view) | 3-66 |
| 3-29 | Telemetry Generator Block Diagram | 3-72 |
| 3-30 | Telemetry DC/DC Converter | 3-73 |
| 3-31 | Telemetry Transmitter | 3-74 |
| 3-32 | Telemetry Transmitter (rear view) | 3-75 |
| 3-33 | Telemetry Generator | 3-76 |
| 3-34 | Telemetry Generator (rear view) | 3-77 |
| 3-35 | DC/DC Converter (top view) | 3-78 |
| 3-36 | DC/DC Converter (bottom view) | 3-79 |
| 3-37 | Waveguide Switching Schematic | 3-82 |
| 3-38 | Solar Array Power Curve | 3-93 |
| 4-1 | Predicted Change in Angular Momentum Vector Due to Magnetic Torques | 4-3 |
| 4-2 | Minimum Heliocentric Inclination Angle as a Function of Launch Date | 4-6 |

LIST OF ILLUSTRATIONS (Continued)

| <u>Figure</u> | <u>Title</u> | <u>Page</u> |
|---------------|---|-------------|
| 4-3 | Orbit Plane Trajectory Profile | 4-8 |
| 4-4 | Available Time for Experiment Evaluation as a Function of Altitude Region | 4-9 |
| 4-5 | Radial Profile as a Function of Time | 4-10 |
| 4-6 | Typical Transfer Orbit Ground Trace | 4-11 |
| 5-1 | Block Diagram for Data Processing | 5-2 |
| 5-2 | Star Sensor System, Principle of Operation | 5-4 |
| 5-3 | Typical Star Data | 5-4 |
| 5-4 | State Definition and Starting Values | 5-10 |
| 5-5 | Approximate Solution | 5-10 |
| 5-6 | Residual Time History for Perfect Model | 5-10 |
| 5-7 | Residual Time History for an Imperfect Model | 5-13 |
| 5-8 | Residual Time History for an Imperfect Model | 5-13 |

LIST OF TABLES

| <u>Table</u> | <u>Title</u> | <u>Page</u> |
|--------------|---|-------------|
| 1-1 | Satellite Characteristics | 1-5 |
| 1-2 | Program Requirements | 1-7 |
| 1-3 | Primary Mission Objectives of the NETS Program | 1-9 |
| 1-4 | Performance simulation Parameters | 1-10 |
| 2-1 | Launch Vehicle Selection | 2-6 |
| 3-1 | Stars Brighter than $M_V + 3$, 43° to 53° South of Ecliptic Plane | 3-31 |
| 3-2 | Equipment List | 3-56 |
| 3-3 | Command List | 3-69 |
| 3-4 | Telemetry Subsystem Characteristics | 3-70 |
| 3-5 | Fan Beam Link Calculations | 3-84 |
| 3-6 | Fan Beam Link Calculations | 3-84 |
| 3-7 | Fan Beam Link Calculations | 3-85 |
| 3-8 | Telemetry Subsystem Link Calculations | 3-87 |
| 3-9 | Star Detector Subsystem Link Calculations | 3-88 |
| 3-10 | Command System Link Calculations | 3-89 |
| 3-11 | Solar Array Degradation Factors | 3-92 |
| 3-12 | Environmental Degradation Factors | 3-92 |
| 3-13 | Power Subsystem Operating Modes | 3-96 |
| 3-14 | Power Subsystem Power Requirements | 3-97 |
| 3-15 | Battery Charging Availability | 3-98 |
| 4-1 | One-Year Test Program Objectives | 4-4 |

SECTION 1
SYSTEM DESCRIPTION AND PROGRAM SUMMARY

The need for a precise earth-referenced navigation capability is rapidly approaching. It has been estimated that by the year 1970 there will be sufficient aircraft aloft continuously to impose the requirement of maintaining precise information covering the location and direction of motion of each one of these aircraft.

Simultaneously, the number of ships and smaller vessels is also rapidly increasing. The need for precise navigational capability may be not as stringent for most oceangoing vessels but the requirement for reasonable accuracies with minimal equipment requirements will be a necessity.

The use of satellites for accomplishing both near-earth and inter-planetary navigation has been proposed by many authors. The mode of operation in which the satellite is used for navigation has yet to be established.

The intent of this brief summary is to outline and explain a satellite navigation experiment which may be conducted with the SCS synchronous communication satellite developed by Philco WDL. The small size and light weight of this satellite make it an ideal vehicle for implementing a Fan Beam Navigation Experiment. The proposed satellite could be launched as a primary or secondary mission on any of a number of booster vehicles.

1.1 GENERAL DESCRIPTION

The Navigational Experiment Test Satellite (NETS) Program Plan has been prepared under NASA Contract No. NASW 1368. The navigation experiment discussed results from four basic premises:

- a. The navigation concept to be tested is the fan beam as proposed by Dr. Stanley F. Schmidt in 1964.
- b. The navigation experiment shall be configured around a small spinning Synchronous Communications Satellite (SCS) developed by Philco WDL.
- c. The launch vehicle for the experiment will be open to a number of possible selections.
- d. The satellite program development time and subsystem modifications shall be kept to a minimum.

The body of this report presents a satellite design that satisfies all program requirements as stated in Section (1.1.2). An artist's conception of the proposed vehicle configuration is shown in the frontispiece. The basic satellite design and electrical system have not been changed from the SCS. However, the following items have been added to the satellite to provide the necessary essential equipment for a useful navigation experiment.

| <u>Item</u> | <u>Weight</u> |
|----------------------------------|---------------|
| Command System | 5 lb. |
| Battery System | 16 lb. |
| Star Detector | 9 lb. |
| Nutation Damper | 1.5 lb. |
| Slotted Waveguides | 5 lb. |
| Additional Telemetry Transmitter | 5 lb. |

The new satellite configuration with additional equipment added is shown in Figure 1-1 and Sheet 1 of Figure 3-8. Moment-of-inertia calculations and structural dynamic analysis have been conducted to substantiate this vehicle's structural integrity and vehicle stability at the desired spin frequency of 100 rpm.

The added items of equipment as listed above have each been studied in considerable detail to determine development times and fabrication problems. There appear to be no critical problem areas in any of these subsystems which require advancements in the state of the art or entail particularly difficult fabrication and testing problems.

The general characteristics of the satellite as currently configured are shown in Table 1-1.

The Navigation Satellite, as configured in this study, is small enough in size and weight so that it could conceivably be flown as a single primary experiment on a small launch vehicle or as a secondary experiment on a larger vehicle. This design concept is felt to offer the maximum versatility in mission planning.

1.1.1 Program Task

The NETS Program consists of a number of individual tasks. The major tasks are broken down into the following three basic areas:

- a. Satellite development.
- b. Satellite operation and data collection.
- c. Post-flight data analysis and derivation of experimental results.

The detailed tasks for areas a and b above will be discussed further in Section 2.

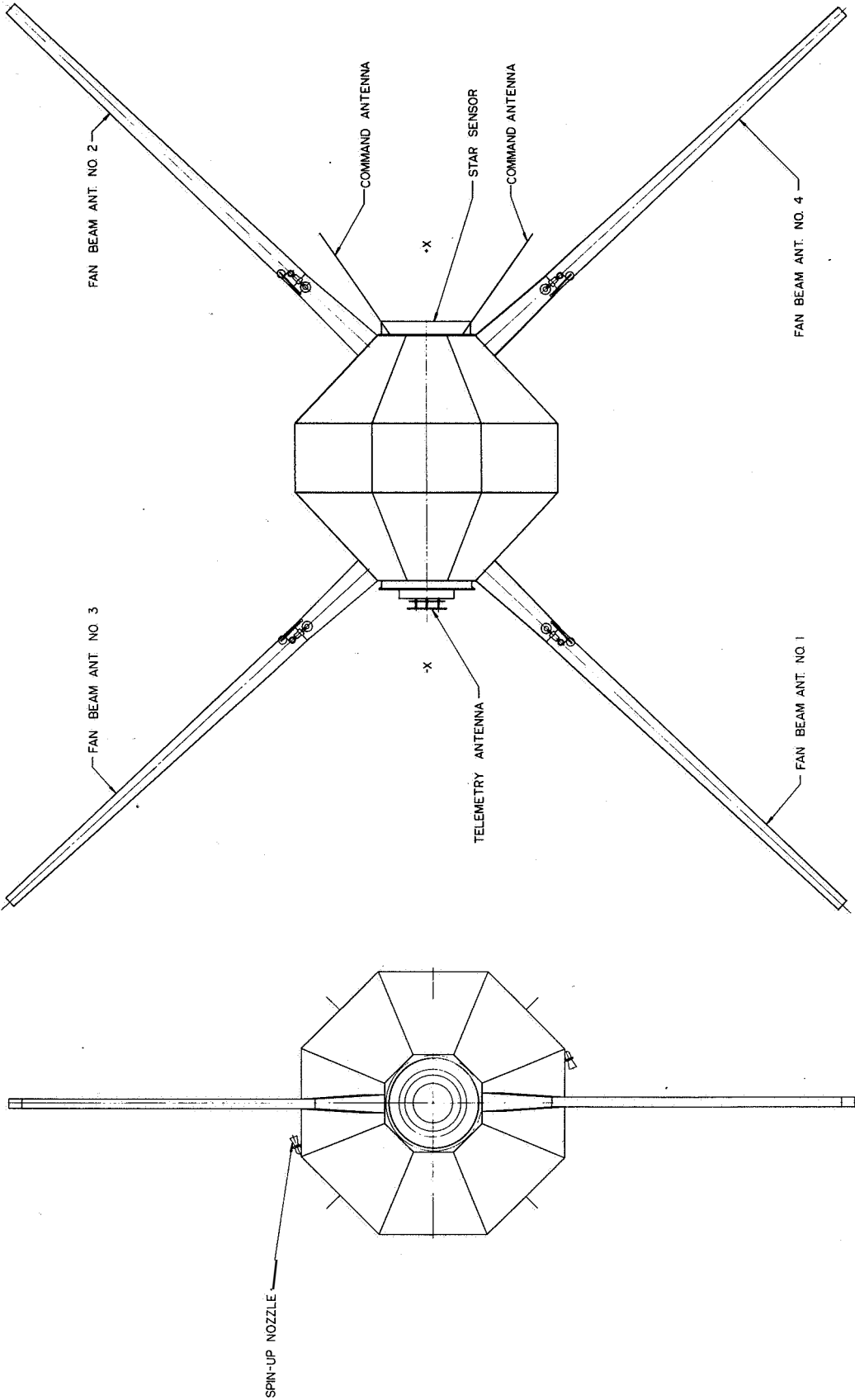


Figure 1-1 Fan Beam Navigation Experiment Satellite

Table 1-1 Satellite Characteristics

| <u>Quantity</u> | <u>Value</u> | |
|--|------------------------------|----------------|
| 1. Transmitter power output | 6 watts | |
| 2. Transmitter frequency | 2 GHz | |
| 3. Rotation rate | 1.67 rev/sec | |
| 4. Antenna beamwidth: Wide dimension | 102° | |
| Narrow dimension | 2.55° | |
| 5. Length of the fan beam antenna | 4 feet (40 slots) | |
| 6. Uncertainty in knowledge of satellite spin axis (bias error) | .1 mr | |
| 7. Uncertainty in mounting angle of the slotted waveguide (bias error) | .1 mr | |
| 8. Uncertainty in position of reference pulse (bias error) | 5 μ sec | |
| | <u>1</u> | |
| 9. Number of satellite revolutions used for obtaining a position fix. | 0-50 | |
| | $\Delta\phi$ | Sat. Alt. |
| | <u>(μrad)</u> | <u>(n.mi.)</u> |
| 10. Nonlinearity in antenna pattern resulting from antenna deflections | 1 | 19311 |
| | 32 | 5000 |
| | 300 | 2000 |

1.1.2 Program Requirements

The Fan Beam Navigation Experiment as currently defined requires several mission'peculiar items of hardware. The selected design for these hardware items and integration of new subsystems into the SCS satellite configuration should result in a satellite capable of accomplishing the various navigation experiments as defined. The detailed program requirements are indicated in Table 1-2.

1.2 PROGRAM OBJECTIVES

1.2.1 General

The problems associated with a fan beam navigational satellite have been investigated in considerable detail during the period of this study. The detailed analytical results, as documented and presented in Volumes I-IV of this Final Report, indicate the definite feasibility of implementing an operational navigation system employing these techniques. However, before any operational system is implemented, it is necessary to verify analytical predictions and gain further information on the fan beam navigation technique by accomplishing an experimental test. The satisfactory flight-test verification of the concept and acquisition of flight performance data is the real goal of the NETS program. Once this has been accomplished and the currently predicted results are verified, an operational system could be evolved rapidly.

1.2.2 Primary Mission Objectives

The primary objective of the NETS program will be to verify the predicted accuracy of the fan beam navigation technique. In view of the limited power and size of the NETS vehicle, the experiments will be conducted over a wide range of altitudes: 100 n.mi. to synchronous altitude. Since appropriate utilization of the measured fan beam passage data requires a precise knowledge of both the satellite ephemeris and its

Table 1-2 Program Requirements

| <u>Requirement</u> | <u>Specification</u> | <u>Special Hardware Required</u> | <u>Comments</u> |
|-----------------------------------|---|---|---|
| 1. Satellite Development | 1 year | Standard (SCS) Structure | Maximum use is to be made of SCS Program experience technology, components, design and documentation in the Navigation Experiment integration. The basic SCS satellite will be fabricated and modified as required at Philco WDL. Qualification test will be accomplished at the subsystem and the satellite level. |
| 2. Launch Vehicle/Site | Open/AMR | Dispenser or spin table | Proposed configuration has self-contained spin-up capability. |
| 3. Mission Lifetime | 1 year | None | For accomplishment of primary mission goals. Star Sensor Experiment may extend for a period of five years or to satellite deactivation. |
| 4. Hardware Development | State-of-the-art and flight qualified if available | | |
| 5. Tracking Station Compatibility | NASA STADAN | 8 GHz receiving equipment | May require receiver modification. |
| 6. Orbit Selection | Elliptical (100 n.mi. - synchronous altitude) $\pm 5.5^\circ$ inclination with respect to the elliptic plane. | Reorientation of dispensing vehicle | Satellite would be injected into the transfer orbit for a synchronous mission . Time of launch must be fixed to attain proper orbit inclination. |
| 7. Attitude Stabilization | Spinning satellite with nutation damper. Spin axis normal to orbit plane. | Nutation damper | Self-contained Passive Mercury Damper. |
| 8. Attitude Determination | 50-100 μ radians | Star detector | As proposed by WDL for NASA ATS-C |
| 9. Power Source | 40 watts average, 75 watts peak | Photovoltaic/battery | |
| 10. Fan Beam Antennas | Slotted waveguides 4-feet long | Honeycomb structure and waveguide | |
| 11. Telemetry Link | Two TLM transmitters at 400 MHz | | Standard SCS hardware |
| 12. Command Link | 125-150 MHz | Four whip antennas | Throughout orbit |
| 13. Orbit Determination | Less than 1 km in position | None | |
| 14. Data Collection | STADAN tracking network and smaller stations | Portable tracking stations (2' - 15') | Smaller stations could be Mascot type of mobile tracker. |
| 15. Data Processing | Digital data processing and system calibration | Software to be developed by Philco WDL. | Several data processing programs are already under development for the Star Sensor. |

spin axis, a nutation damper and star detector have been added to reduce spin-axis motions and determine spin-axis orientation. Table 1-3 shown in somewhat greater detail the primary mission objectives.

1.3 PREDICTED PERFORMANCE

The usefulness of the navigation experiment outlined is keyed directly to the accuracies of measurements which **may** be attained in orbit. Considerable analysis and digital simulations have been conducted to **determine** the best estimate of these predicted accuracy values. Extensive digital **simulation** was conducted in the following areas and the complete results may be found in Volumes **II-IV** and the **ATS** Star Sensor Report (1):

- a. Star detector simulation and data processing
- b. Simulation of the RF fan beam propagation and detection from a deflected slotted waveguide on a spinning satellite
- c. Simulation of the vehicle attitude errors and fan beam propagation and detection errors on position determination from **a** spinning satellite.

Table 1-4 shows **some** of the errors included for a typical vehicle simulation. The resulting predicted position accuracy versus central satellite revolution number is shown in Figures 1-2 through 1-5 for various diameter receivers and **two** different satellite altitudes.

(1) Final Report Phase I, Star Detector Experiment For **ATS-C**, Philco Corporation, **WDL-TR2664**, Contract No. **NAS5-9682**, 22 November 1965.

Table 1-3 Primary Mission Objectives of the NETS Program

| <u>Objective</u> | <u>Accomplished By Use Of</u> |
|--|---|
| 1. Determination of the predictability of the precise attitude and attitude time history of a spinning body. | Telemetry Data Star Detector Simulation Data Reduction Capability. |
| 2. Demonstration of the accuracy by which spin-angle information can be determined by RF sensed data over a wide range of satellite altitudes. | Ground Tracking Facilities for Detection Fan Beam Simulation Data Reduction Capability. |
| 3. Demonstration of the accuracy by which a navigator's position may be established by RF sensed information. | Objectives (1) and (2) Position Computation Facility. |
| 4. Demonstration of the degree to which precession rates can be damped using an appropriately designed nutation damper. | Objectives (1) and (2) Nutation Damper Simulation Capability. |
| 5. Demonstration of the feasibility of generation of reference signals from a star sensor. | Objectives (1) and (2). |
| 6. Determination of the potential environmental problems that could affect the accuracy of a navigation satellite system. | Objectives (1), (2), (3), (4), (5). |

Table 1-4 Performance Simulation Parameters

| <u>Parameter</u> | <u>Value/Quantity</u> | <u>Comment</u> |
|---|---|--|
| <u>Satellite</u> | | |
| 1. Spin rate | 1.67 rps | |
| 2. Reference pulse | Each revolution | Error in reference pulse = $\frac{3}{1} \mu s$. |
| 3. Spin axis orientation | Normal to orbit plane | Error in spin-axis orientation = .1 mr. |
| 4. Fan beam normals relative to satellite | 45° , 135° | Error in antenna mounting = .1 mr/antenna. |
| 5. Length of fan beam antennas | 4 ft. | 40 slots @ 8 GHz |
| 6. Type of fan beam simulation used | Analytical | See Volume II for description of equations. |
| 7. Vehicle dynamic simulation | Axially symmetric spinning body | See Volume II for description of equations. |
| 8. Satellite power | 6 watts/beam | |
| 9. Transmitter frequency | 8 GHz | |
| 10. Satellite ephemeris altitude | 5000 n.mi. and 19,311 n.mi. | Medium and synchronous altitude |
| Inclination | 0° | Equatorial orbits. |
| Eccentricity | 0^a | Circular orbits. |
| 11. Calibration Scheme | Inertially fixed fan beam normals and angular velocity vector Over time of smoothing interval | See Volume II for description of calibration techniques. |
| 12. Antenna deflection effects | 1 μrad @ h=19,311 n.mi. 32 μrad @ h=5000 n.m. | See Volume III for description of antenna simulation. |

Table 1-4 Performance Simulation Parameters (Cont.)

| <u>Parameter</u> | <u>Value/Quantity</u> | <u>Comment</u> |
|-----------------------------------|---|--|
| <u>Navigator</u> | | |
| <u>Receiver</u> | | |
| 1. Noise Temperature | 1000°K | |
| 2. Dish efficiency | 0.5 | |
| 3. Total link loss factor | 0.5 | |
| 4. Mode of detection | Amplitude | Detection at 0.6 amplitude. |
| 5. Dish size | 0.2' to 25.6' | Parametric variations in dish size. |
| <u>Motion</u> | | |
| 1. Range from sub-satellite point | 2400 n.mi. | Measured on surface of earth. |
| 2. Altitude | 36,000 ft. | |
| 3. Velocity | 600 n.mph | On a great circle path relative to a rotating earth. |
| 4. Heading | Due West | |
| <u>Method of Data Reduction</u> | | |
| 1. Method of smoothing | Time averaging of sums and differences | See Volume 11 for description of time averaging. |
| 2. Computation of a fix | Analytical technique applied at mid-point of smoothing time interval. | See Volume II for description of fix calculations. |
| 3. Number of smoothing cycles | 0-50 revolutions | |

CASE 30. FANS. SMOOTH T. ALT. 5000 N MI. ALL
 MOTIONS. W OFF .1 MRAD. DIST. 2400. AZM. 60.

7094 F11/V2-
 0065 0000

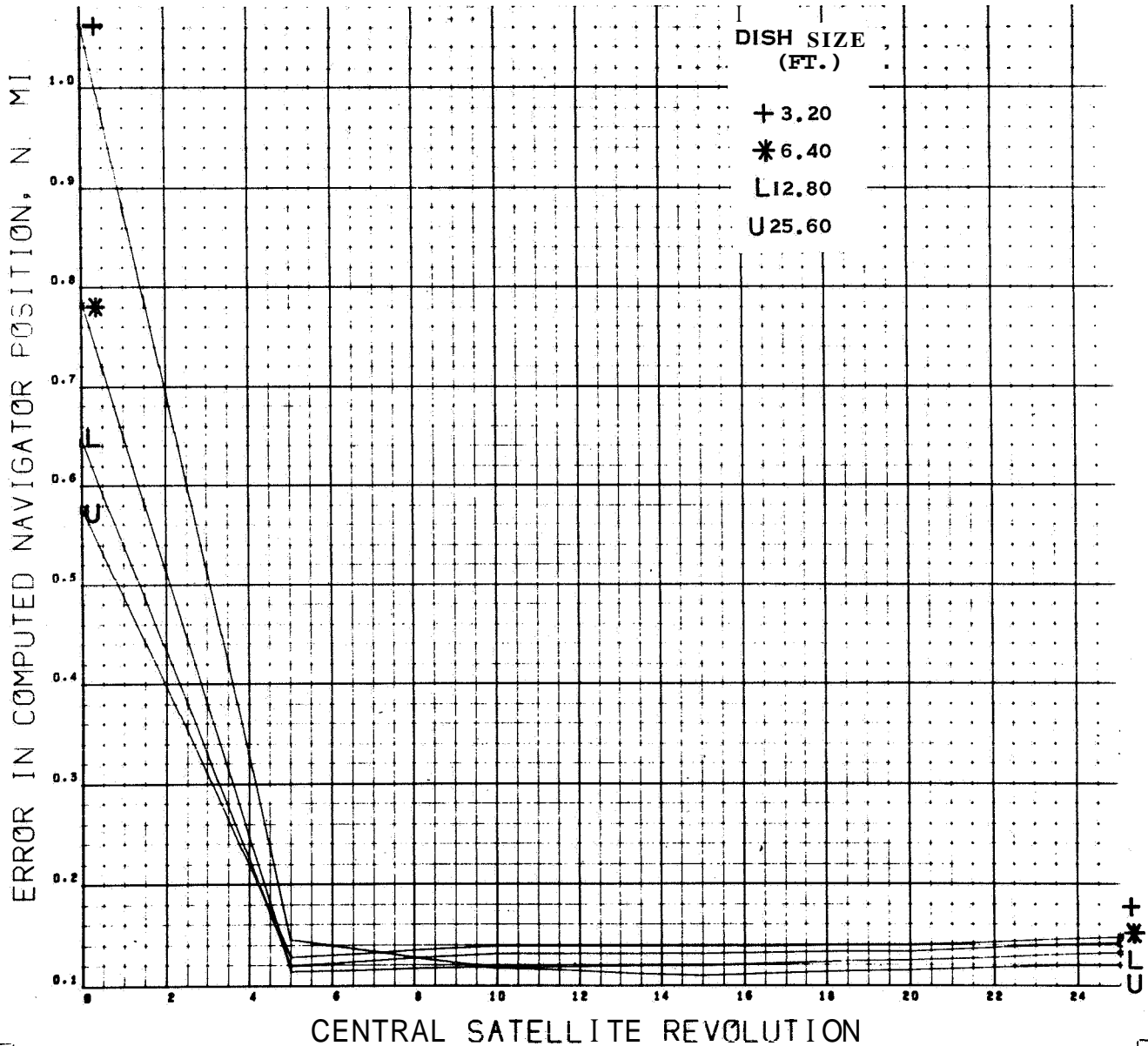


Figure 1-2 Performance Curves Showing Accuracy vs Smoothing Times for Various Receiver Dish Sizes (Case 30, 3.2 to 25.6 Foot Dishes)

CASE 30. FANS. SMOOTH T. ALT. 5000 N MI. ALL
 MOTIONS. W OFF .1 MRAD. DIST. 2400. AZM. 60.

7094 F11/V2
 0064 0000

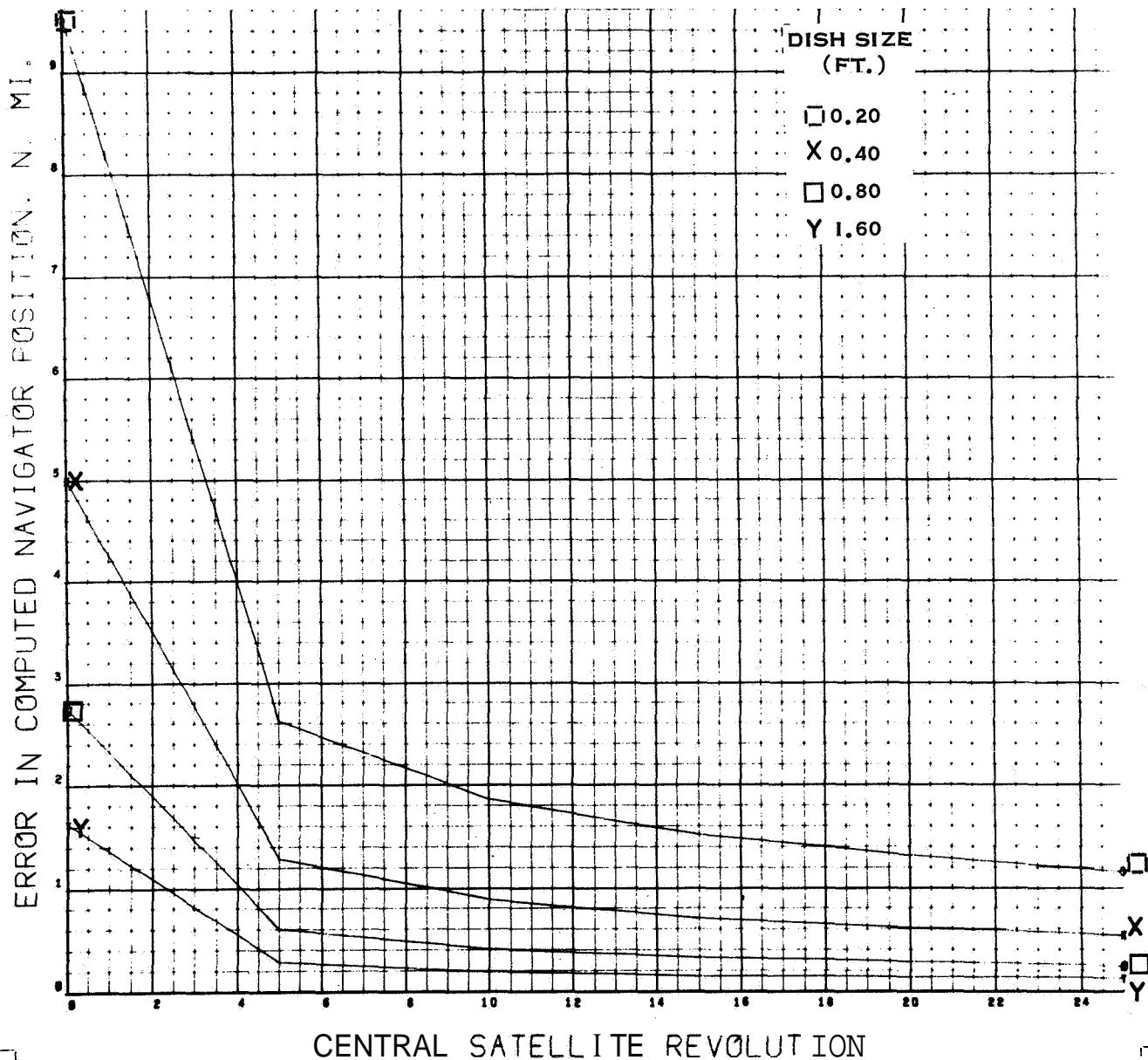


Figure 1-3 Performance Curves Showing Accuracy vs Smoothing Times for Various Receiver Dish Sizes (Case 30, 0.2 to 1.6 - Foot Dishes)

CASE 31 FANS. SMOOTH T. ALT. 19311 N MI. ALL
 MOTIONS. W OFF .1 MRAD. DIST. 2400. AZM. 60

7094 F11/V2 -
 0065 0000

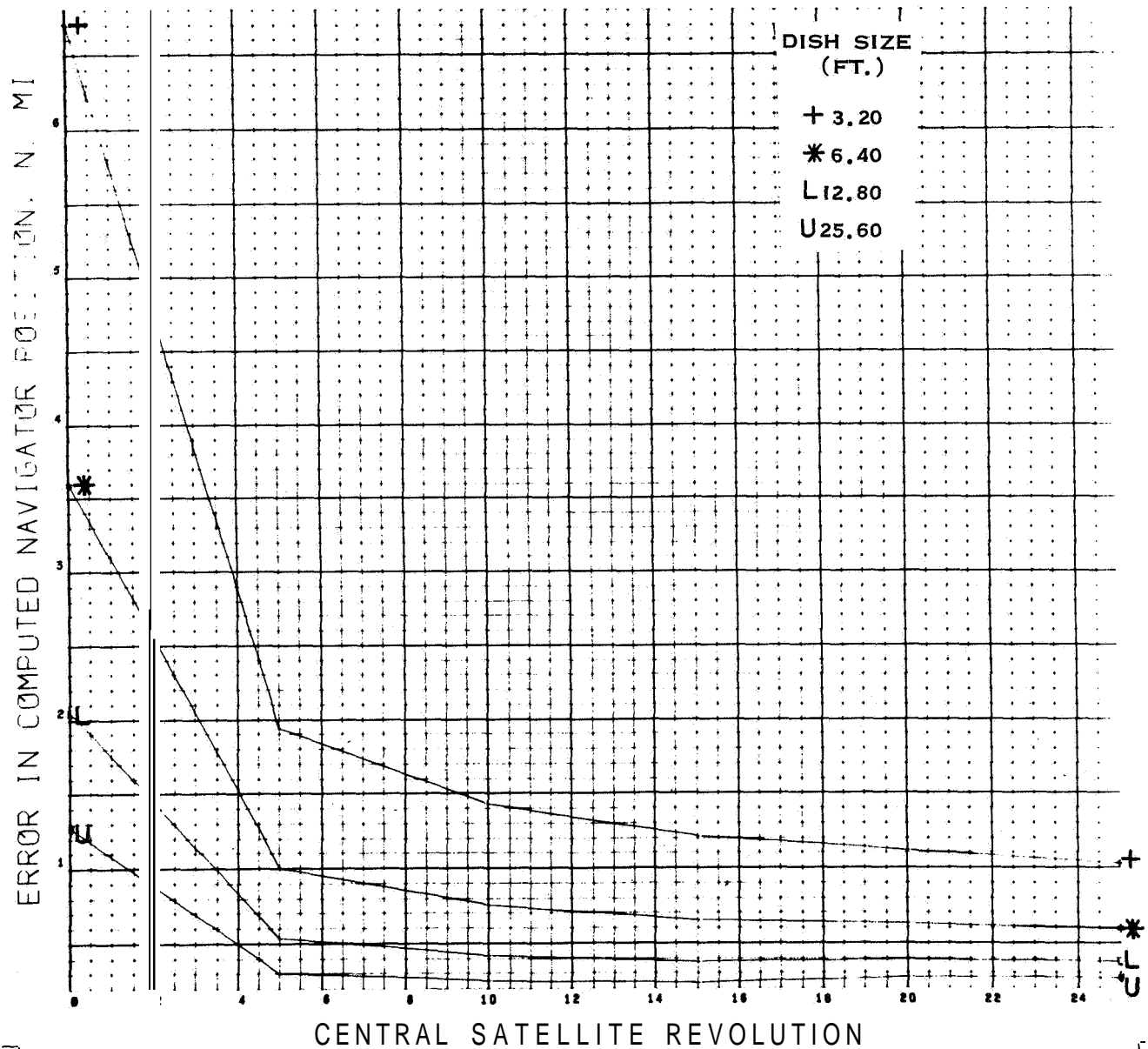


Figure 1-4 Performance Curve Showing Accuracy vs Smoothing Times for Various Receiver Dish Sizes (Case 31, 32 to 25.6 - Foot Dishes)

CASE 31 FANS. SMOOTH T. ALT. 19311 N MI. ALL
 MOTIONS. W OFF .1 MRAD, DIST. 2400. AZM. 60

7094 F11/V2
 0064 0000

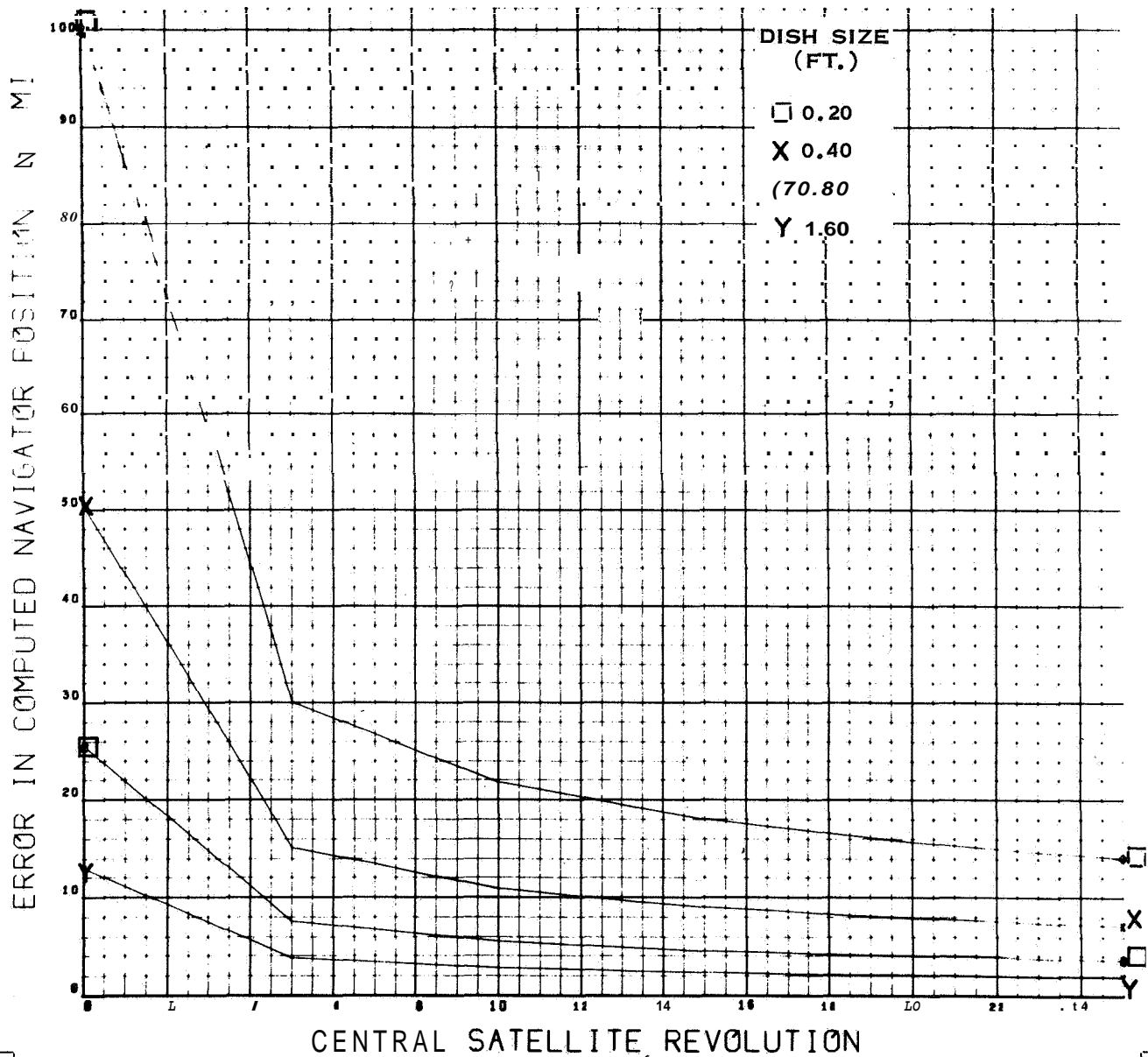


Figure 1-5 Performance Curve 8 Showing Accuracy vs Smoothing Times for Various Receiver Dish Sizes (Case 31, 0.2 to 1.6 - Foot Dishes)

SECTION 2

PROGRAM PLAN

2. I SATELLITE DEVELOPMENT

A preliminary plan for the NETS Program has been prepared based on a total satellite development time of one year. This time schedule includes auxiliary hardware development for the star sensor, nutation damper, and the slotted arrays. The majority of the remaining satellite equipment is either currently available or requires only minor modifications of existing equipment. The program plan provides for a mock-up, a qualification model, and a flight model of the satellite. Additional spare parts would be made available for various subsystems. Schedule (1) (Figure 2-1) shows the major milestones for the over-all satellite development. Schedules (2), (3), and (4) (Figures 2-2, 2-3 and 2-4) show major milestone schedules for the star detector, antennas, and nutation damper, respectively, which enable the over-all satellite development time of one year to be realistically achieved.

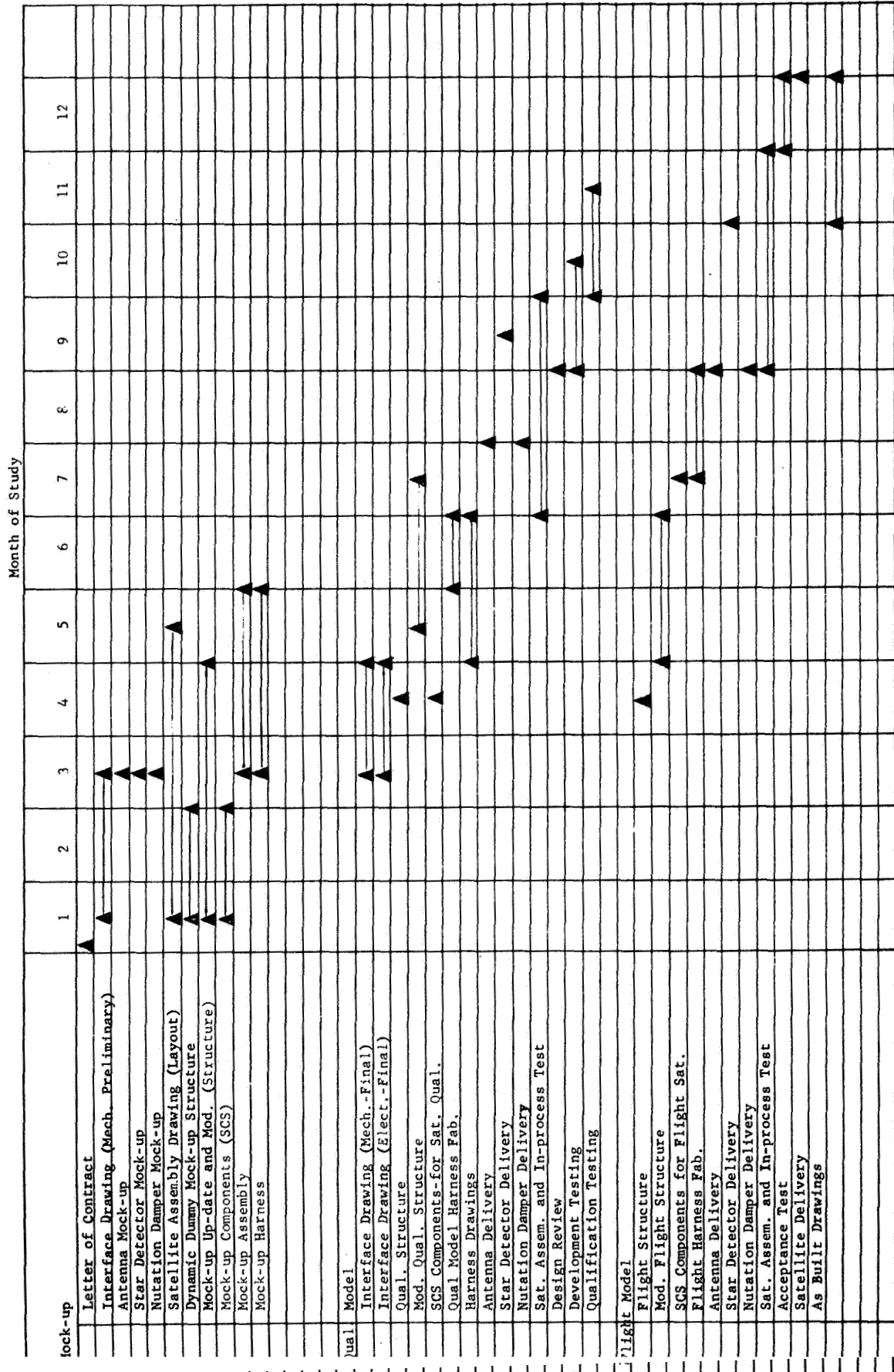
2.2 LAUNCH VEHICLE

To provide some versatility in planning of a NETS Program, the launch vehicle has been purposely left unspecified. As previously mentioned, the size and weight of the satellite permit a number of possible launch vehicles to be utilized. Table 2-1 shows some typical launch vehicle possibilities and a reasonable estimate of launch date.

Figure 2-1 Navigation Satellite (NETS) Program

Milestone Schedule (1)

Satellite Development

WDL FORM No. 791
4-62

STOCK NO. 18-900005-32

Figure 2-2 Navigation Satellite (NETS) Program

Milestone Schedule (2)

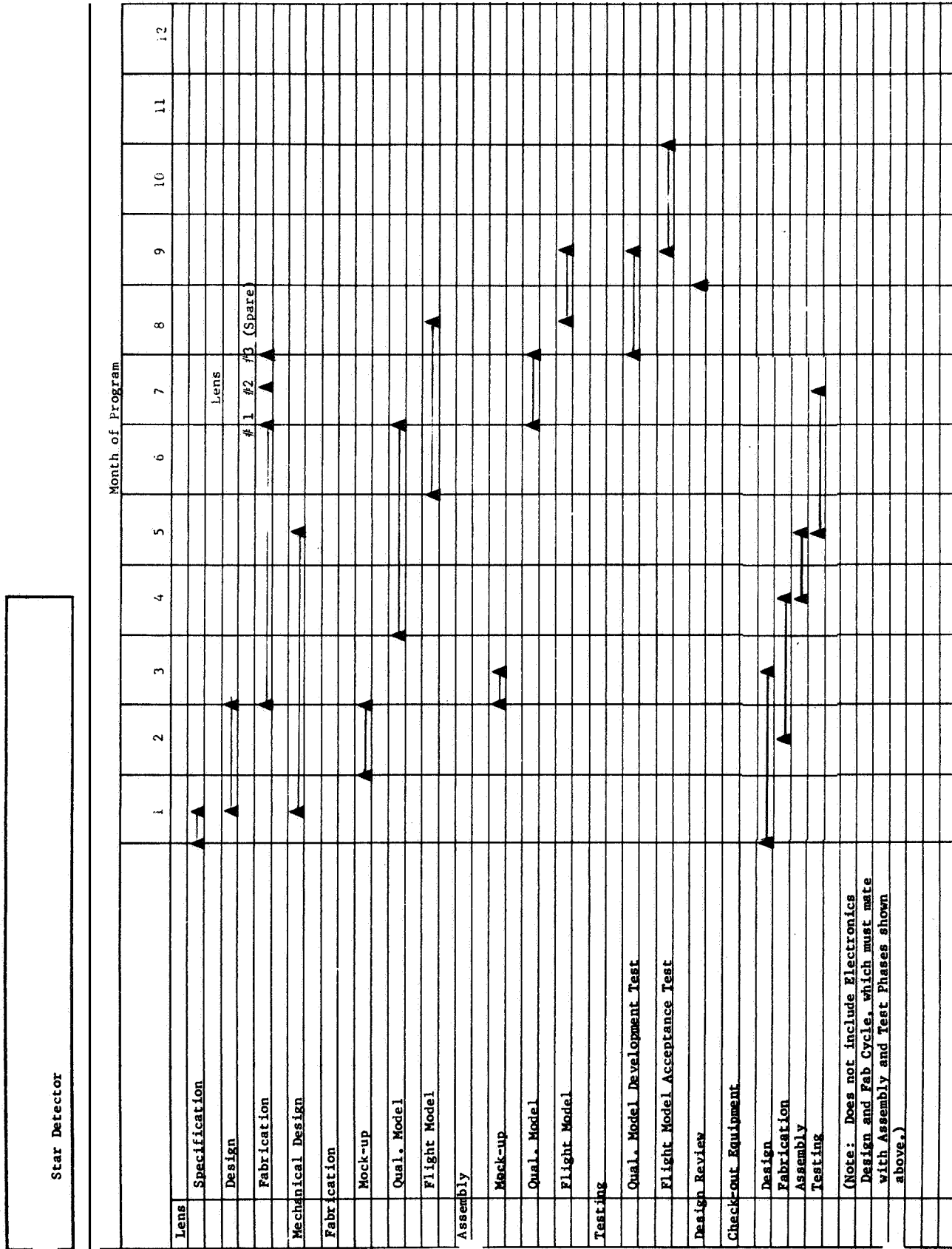
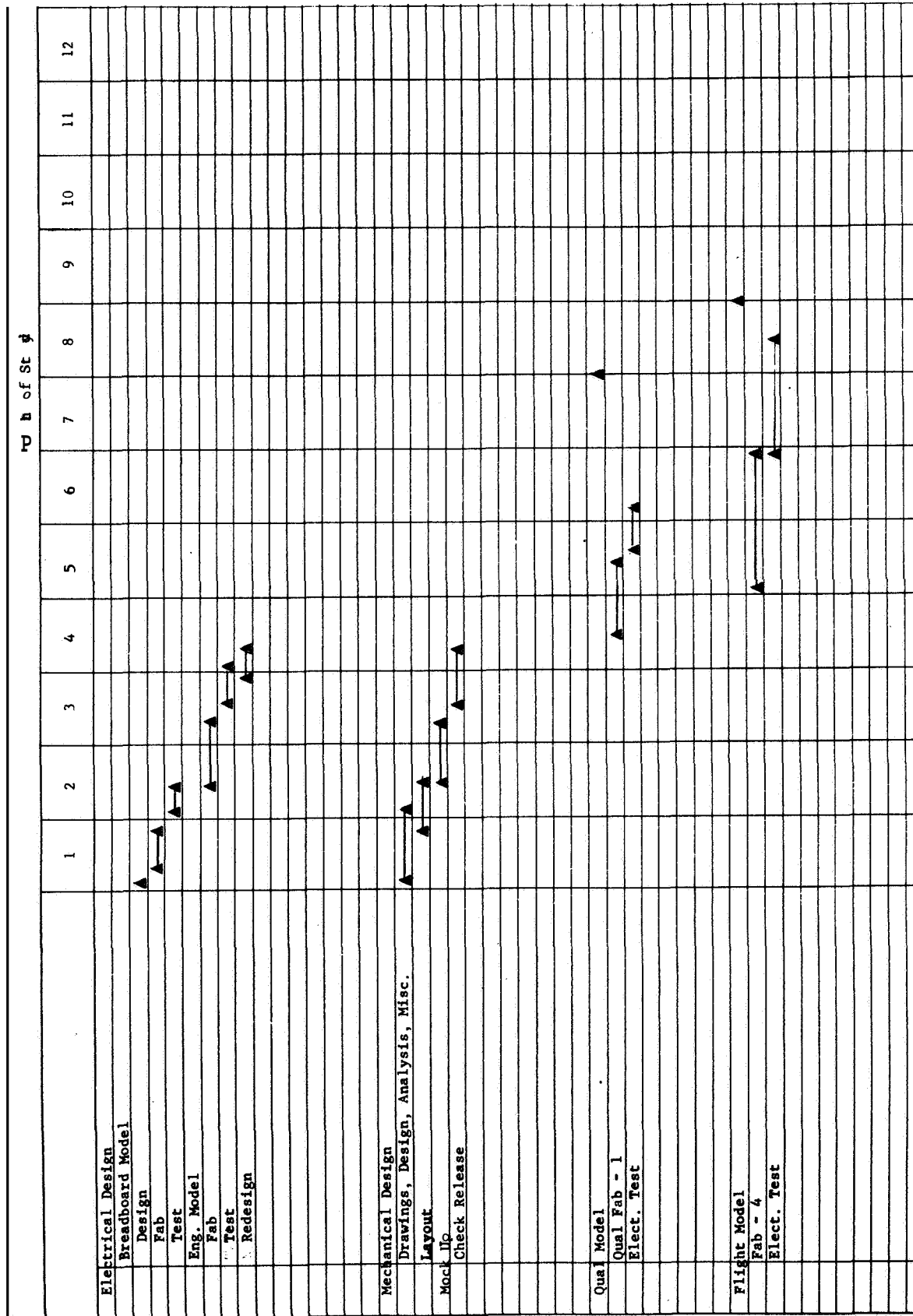


Figure 2-3 Navigation Satellite (NETS) Program

Milestone Schedule (3)

Slotted Waveguides



WDL-TR29624

Figure 2-4 Navigation Test Satellite (NETS) Program

Milestone Scheduie (4)

Nutation Damper

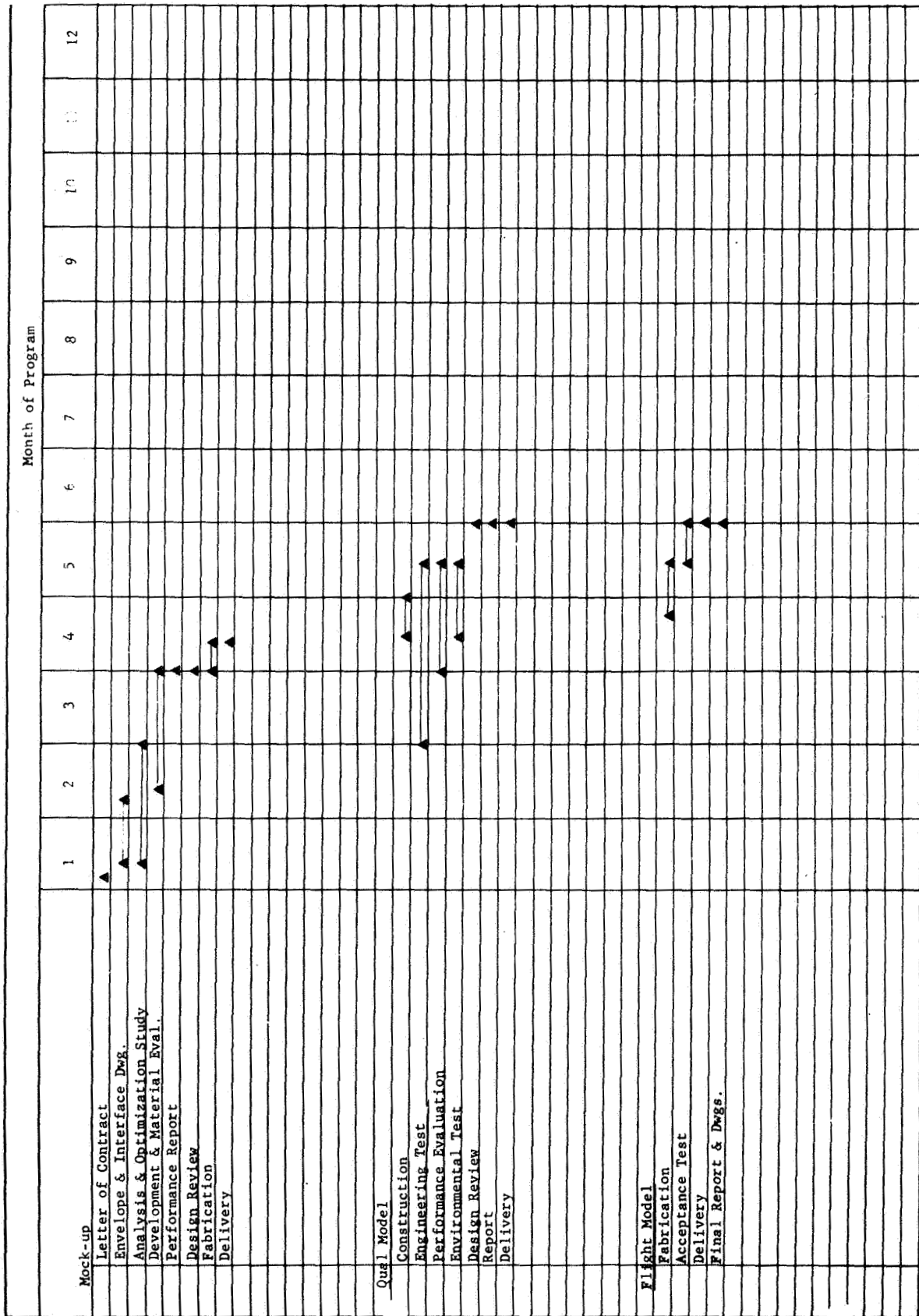


Table 2-1 Launch Vehicle Selection

| Mission Level | Launch Vehicle | Program Name | Orbit Choice (n.mi.) | Probable Launch Date ** |
|---------------------|----------------|----------------------------|----------------------|-------------------------|
| Prime Satellite | scout | NA | Elliptic 100-10,000 | Fall 1967 |
| | Thor/Delta | NA | Elliptic 100-Syn. | Fall 1967 |
| Secondary Satellite | Atlas/Agena | ATS-C | Elliptic * 100-Syn. | Early 1968 |
| | Titan IIIC | Military Comsat Program | Elliptic * 100-Syn. | ? Launch |
| | Saturn V | Apollo Application Program | Elliptic * 150-Syn. | Early 1970's |

* Separated after transfer orbit injection, but before synchronous orbit injection of primary payload.

** Referenced to Program starting date of 1 September 1966.

SECTION 3 DESIGN CONCEPTS

3.1 ANTENNA DESIGN

3.1.1 Antenna Structural Analysis

3.1.1.1 Introduction

A detailed structural analysis was performed on a cantilevered boom antenna. Equations for stress and deflection were derived. A particular antenna of honeycomb sandwich construction was investigated. It is concluded that the configuration studied is structurally feasible.

3.1.1.2 Analysis

Stress and deflection equations were determined for a cantilevered boom antenna of symmetric cross section under the centrifugal inertial loading given by $p = \rho [a + (L-X)\sin\phi]^2 \Omega^2$ shown in Figure 3-1. See table for an explanation of the symbols. This loading may be resolved into components which are normal and parallel to the longitudinal axis of the antenna. It is mathematically convenient to treat these two load components separately because they each produce different stress distributions and deflected shapes in the antenna. Due to the normal loading, the elastic curve, as described by the deflection, y , and rotation, θ , is

$$y = \frac{a \Omega^2 \cos \phi}{24E} \sum_{L=1}^m \frac{\rho_i}{I_i} \left[3\xi^4 - 4x\xi^3 \right]_{\xi_i} (\xi_i + \Delta)$$

$$+ \frac{\Omega^2 \sin \phi \cos \phi}{120E} \sum_{L=1}^m \frac{\rho_i}{I_i} \left[-4\xi^5 + 15L\xi^4 - 20xL\xi^3 + 5x\xi^4 \right]_{\xi_i} (\xi_i + \Delta)$$

List of Symbols for Figures 3-1 through 3-6

| | |
|----------|--|
| a | Radial distance to base of cantilever from satellite spin axis |
| b | Thickness of shear section in shear equation |
| c | Distance to extreme fiber from neutral axis |
| I | Moment of inertia of cross section |
| L | Length of cantilever |
| M | Bending moment |
| p | Distributed loading on antenna due to centrifugal forces |
| Q | First moment of shear area |
| v | Shear stress on cross section |
| V | Shear force |
| x | Distance along cantilever measured from free end |
| y | Lateral deflection of antenna |
| ϕ | Angle antenna forms with the spin axis |
| Ω | Spacecraft spin rate |
| θ | Bending rotation of antenna |
| ξ_i | Distance to i -th element of tapered antenna |
| Δ | Width of unit slice of tapered antenna |
| σ | Normal stresses on antenna cross section, bending or axial |

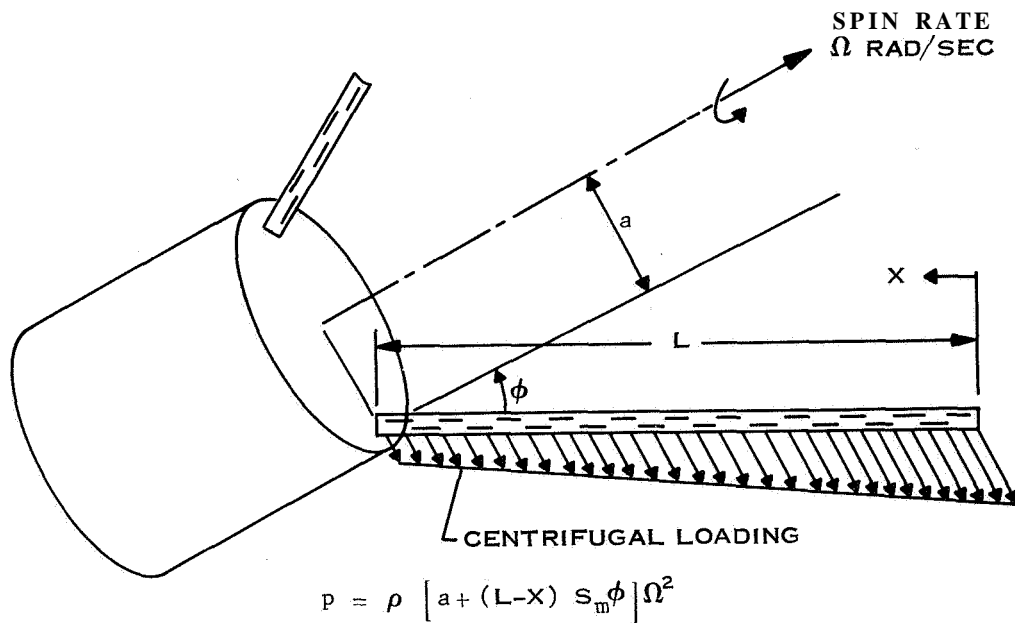


Figure 3-1 Centrifugal Loading on Boom Antenna Due to Spinning Spacecraft

m = number of elements
 n = number of elements between section x and free end

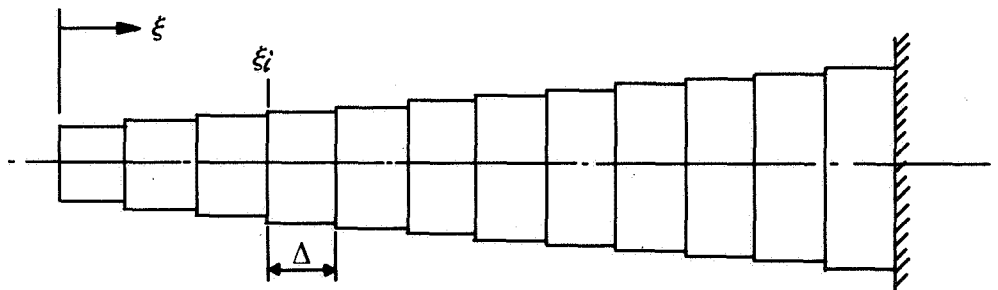


Figure 3-2 Finite Element Approximation of Tapered Cantilever

where ξ_i and Δ are variables (see Figure 3-2). The maximum deflection and rotation occur at $X = 0$. These elastic deformations cause bending moments, M , and shear forces, V , which are

$$M = \Omega^2 \cos \phi \sum_{i=1}^n \rho_i \Delta \left(a + (L - \xi_i - \Delta) \sin \phi \right) \left(X - \xi_i + \frac{\Delta}{2} \right) + \rho_i \frac{\Delta^2}{2} \sin \phi \left(X - \xi_i + \frac{2\Delta}{3} \right)$$

$$V = \Omega^2 \cos \phi \sum_{i=1}^n \rho_i \Delta \left(a + (L - \xi_i - \Delta) \sin \phi \right) + \rho_i \frac{\Delta^2}{2} \sin \phi$$

These forces are associated with internal bending stresses, $\sigma = \frac{Mc}{I}$, and shear stresses, $\tau = \frac{VQ}{Ib}$.

The parallel load component, P_p , produces elongation of the boom antenna and axial stresses which are given by

$$\delta = \frac{\Omega^2}{E} \sum_{i=1}^n \frac{\Delta_i}{A_i} \int_{\xi_i}^{\xi_i + \Delta} \rho_i \left[a \xi \sin \phi + \left(L\xi - \frac{\xi^2}{2} \right) \sin^2 \phi \right] d\xi$$

$$\sigma = \Omega^2 \sum_{i=1}^n \frac{\rho_i}{A_i} \left[a \xi \sin \phi + \left(L\xi - \frac{\xi^2}{2} \right) \sin^2 \phi \right]_{\xi_i}^{\xi_i + \Delta}$$

Observe that by appropriate choice of ξ_i and Δ , the above equations can easily be made to describe stress components of a similar structure of constant cross section. In such a case the above equations reduce to

$$y = \frac{\rho a \Omega^2 \cos \phi}{24EI} (X^4 - 4L^3 X + 3L^4) + \frac{\rho \Omega^2 \sin \phi \cos \phi}{120EI} (11L^5 - 15L^4 X + 5LX^4 - X^5)$$

$$\theta = \frac{\rho a \Omega^2 \cos \phi}{6EI} (L^3 - X^3) + \frac{\rho \Omega^2 \sin \phi \cos \phi}{24EI} (3L^4 - 4LX^3 + X^4)$$

$$M = \frac{\rho a \cos \phi \Omega^2 X^2}{2} + \frac{\rho \sin \phi \cos \phi \Omega^2}{6} (3LX^4 - X^3)$$

$$V = \rho \Omega^2 \cos \phi \left(aX + LX \sin \phi - \frac{X^2}{2} \sin \phi \right)$$

$$\delta = \frac{\rho \Omega^2}{AE} \left[\frac{a}{2} (L^2 - X^2) \sin \phi + \frac{1}{6} (2L^3 - 3LX^2 + X^3) \sin^2 \phi \right]$$

$$\sigma = \frac{\rho \Omega^2}{A} \left[aX \sin \phi + X \left(L - \frac{X}{2} \right) \sin^2 \phi \right]$$

The above equations are applicable to cantilevers of any symmetrical cross section. However, they are based on the usual elementary beam theory, i.e., small deflections, plane sections, and Hooke's Law.

To obtain an evaluation of the structural feasibility of the proposed cantilever configuration under centrifugal inertial loading, stress components were evaluated for a particular boom antenna, namely that described in Section 3.1.2.1, the mechanical design discussion. The cross-section is shown in Figure 3-3 along with some pertinent section properties. Observe that this cross section is symmetric about the A-A axis.

The structural performance of this cantilever was determined for spin rates of 100 to 180 rpm and various antenna lengths up to 100 inches. The lateral deflections are

$$y = 0.2302 \times 10^{-10} \Omega^2 (X^4 - 4L^3X + 3L^4) + .2737 \times 10^{-12} \Omega^2 (11L^4 - 15L^4X + 5LX^4 - X^5)$$

$$y_{\max} = (.8706 \times 10^{-10} L^4 + .03011 \times 10^{-10} L^5) \Omega^2$$

The maximum bending stresses are

$$\sigma_{\max} = 0.0005803 (7.50 + 0.2356 L)$$

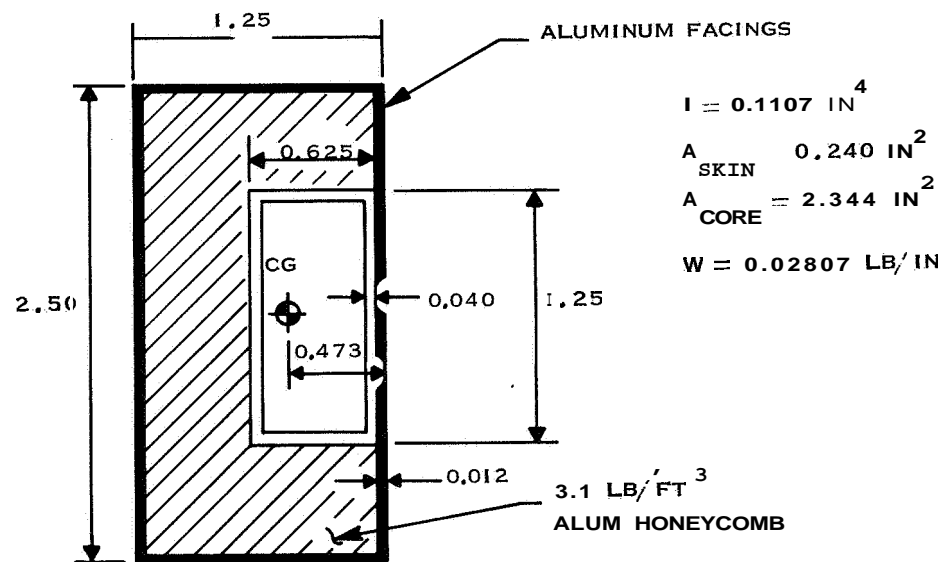


Figure 3-3 Cross Section of Preliminary Honeycomb Sandwich Antenna

Maximum deflections and bending stresses are shown in Figures 3-4 and 3-5. Axial stresses, which superimpose on the bending stresses, are of the order of several hundred psi and, hence, are negligibly small.

The shear stress distribution is somewhat vague because of the interaction of the honeycomb core and the facing material. Comparison of the relative shear stiffnesses of these two components suggested that a good approximation to the shear stress distribution could be obtained by assuming that the shear load is carried entirely by the facing material. The resulting shear **flaw** pattern due to a unit shear force is shown in Figure 3-6. For example, a boom antenna of 100 inches spinning at 180 rpm would experience a maximum shear stress of 921 psi at points f and h on the cross section.

The unsymmetrical cross section produces one other effect: torsional rotations and stresses. To evaluate these stress components, the shear center of the cross section was located. An upper-bound torsional rotation of 0.112 degrees was calculated. This was judged to be negligible compared to the bending deflections and rotations,

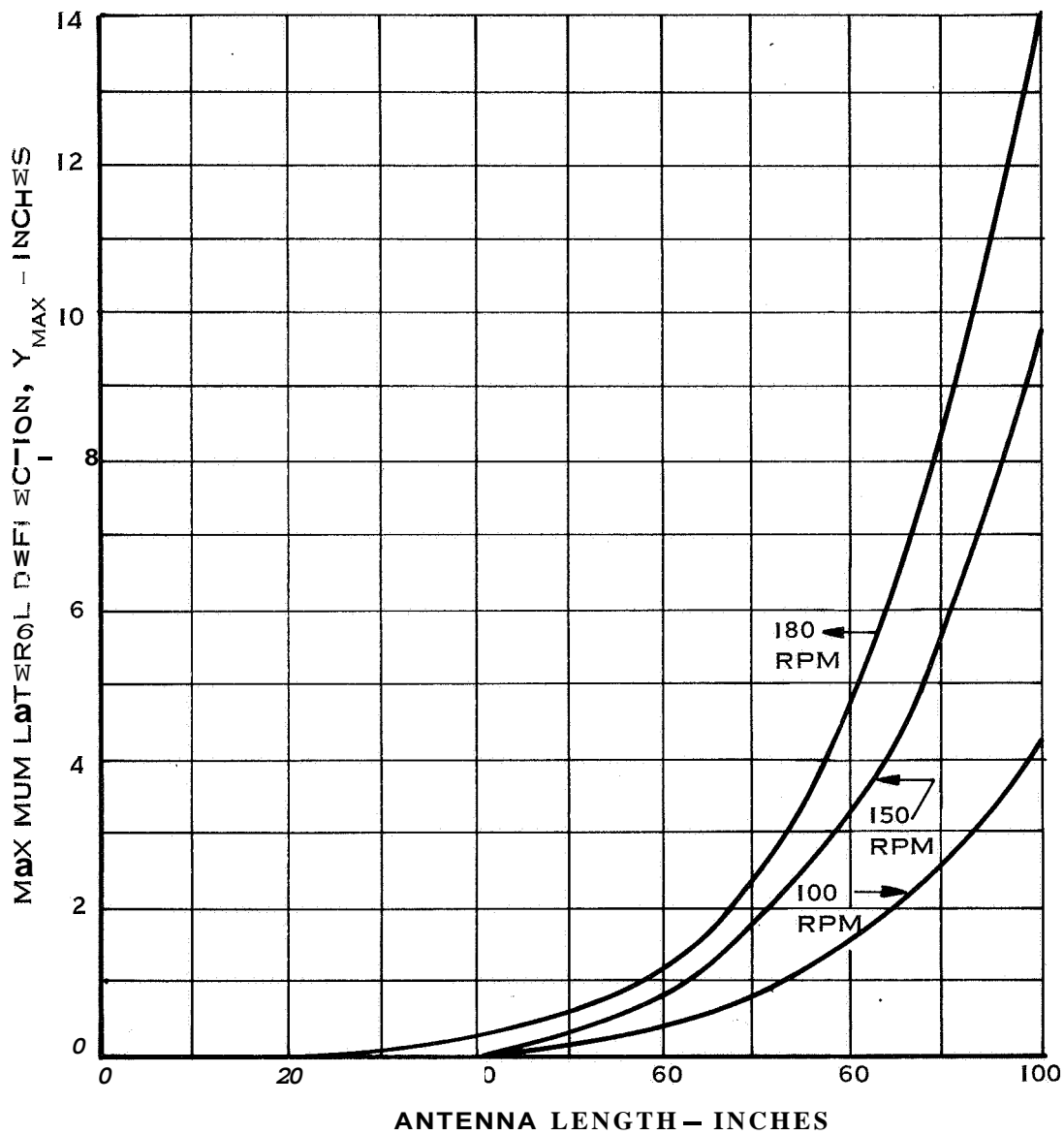


Figure 3-4 Maximum Antenna Deflection vs Antenna Length

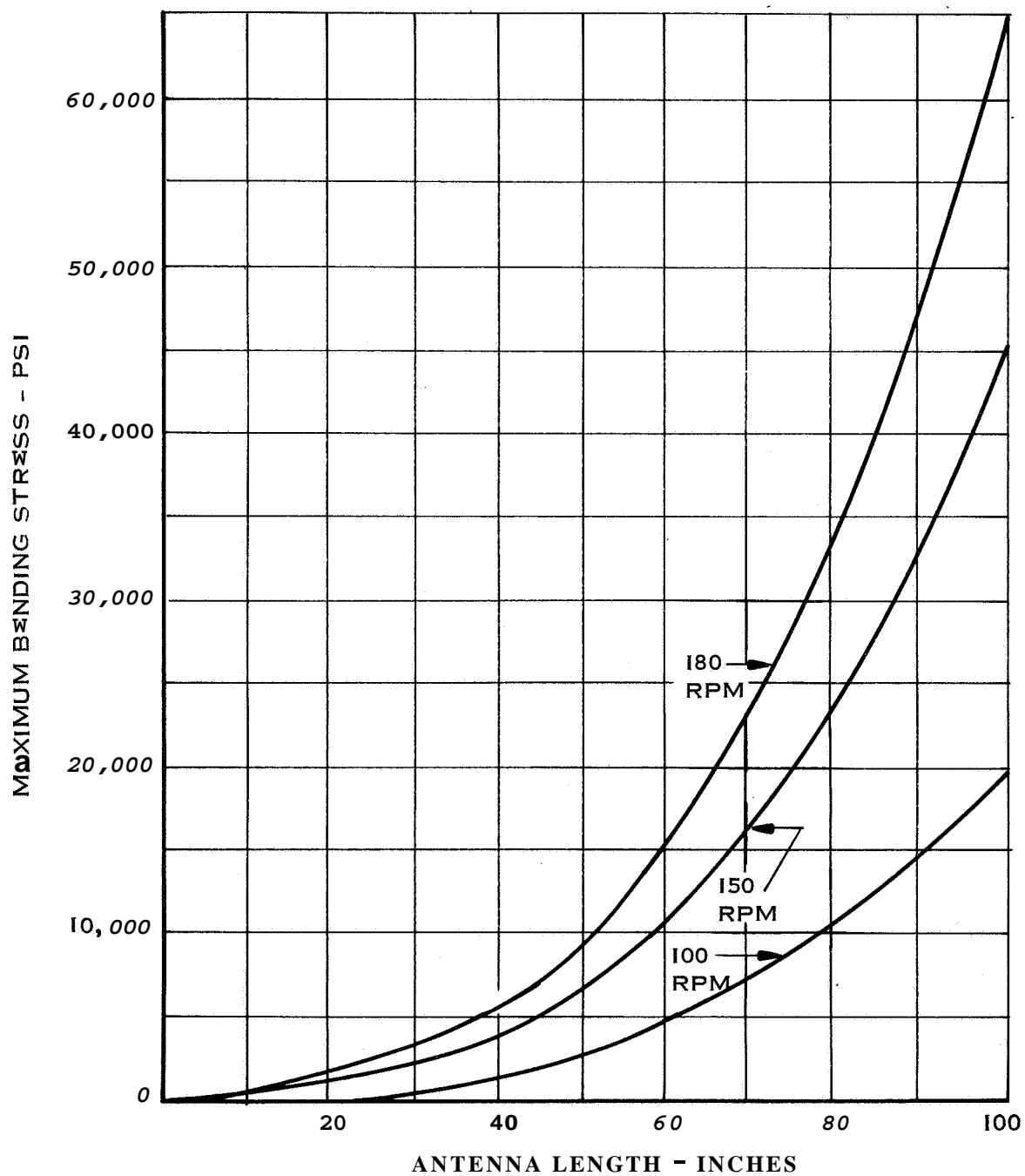


Figure 3-5 Maximum Bending Stress vs Antenna Length

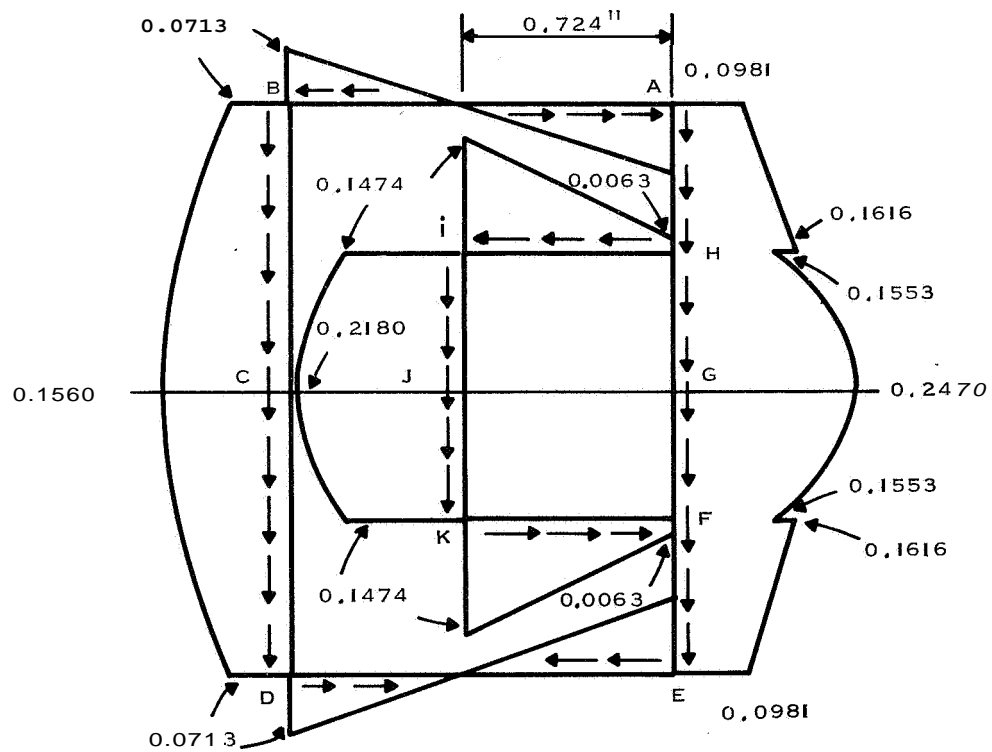


Figure 3-6 Shear Flow Distribution on Antenna, Cross Section

3.1.2 SATELLITE/ANTENNA INTEGRATION

3.1.2.1 Mechanical Design

The antennas are of waveguide/honeycomb sandwich construction, cantilevered from an extension joint, and tapered to reduce tip deflection at orbital spin rate. Each antenna is attached to its support through a double articulated, springactuated hinge. The antenna-mounted joint is a "Negator" spring motor developed by the Hunter Spring Company. It provides a rotational driving force from a pre-coiled band of spring steel wound on two spindles. The total rotation is limited to 90° by mechanical stops in the rotating spindle. The support-mounted joint is a Bendix, Utica Division, "Free Flex" pivot which uses a cross spring design. The "Free Flex" pivot is limited to 45° rotation by a mechanical stop. The antenna pivot is attached to the support pivot by parallel motion arms which allow axial shortening and locking after full rotation of both joints. With the antenna in the deployed position, a cam release allows the support arms to shorten and lock the antenna in place. This is also spring powered. Figure 3-7 shows the four positions from stowed to deployed and locked.

Mechanically the antenna consists of a waveguide, slotted to provide the required RF pattern, and supported by a variable-section honeycomb sandwich. The section varies in both width and depth to minimize deflection along its length. The minimum practical thickness of the honeycomb section, at the outboard end of the antenna, is the controlling factor in the antenna section.

The four antennas are mounted as shown in Figure 1-1 at an angle of 45° to the spin axis. They will be deployed from the folded position (Figure 3-8, Sheet 1) after separation is complete and before the spin-up equipment is activated. The antenna release mechanism is pyrotechnically actuated by a timer command.

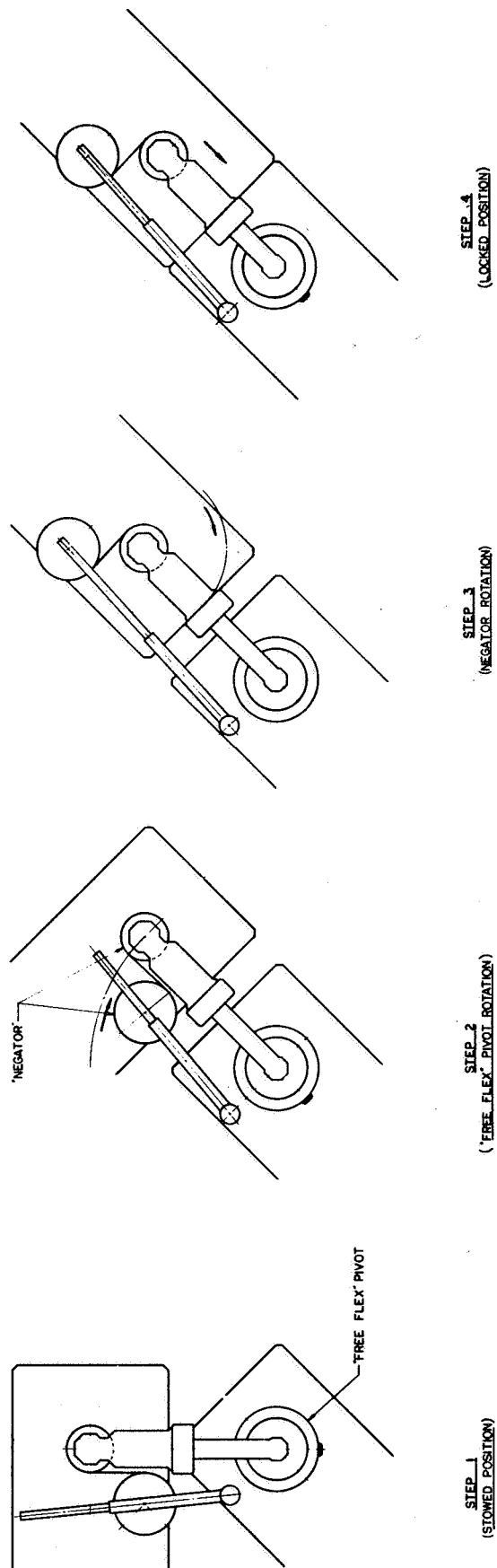


Figure 3-7 Antenna Deployment Hinge

3122 Satellite/Antenna Configuration

The satellite consists of a structure subsystem, a power subsystem, a star sensor subsystem, a telemetry subsystem, a fan beam transmission subsystem, and a command subsystem. All of these subsystems and their individual components have been flight qualified with the exception of the following items of the subsystems :

Structure Subsystem

- Antenna Support
- Antenna Extension Mechanism
- Antenna Release Mechanism

Power Subsystem

- Charge Controller
- TWTA Control
- Event Timer

Star ~~SENSOR~~ **SENSOR** Subsystem

- Power Amplifier
- Star Sensor
- DC/DC Converter

Fan Beam Transmission Subsystem

- Fan Beam Antennas

3.1.2.2.1 Structure Subsystem

The Structure Subsystem consists of the Frame and Housing, the Spin-Up Equipment and the Separation Equipment. There is no modification to Spin-Up or Separation Equipment. The Structure Subsystem will be modified to accept the four antenna supports and to allow for equipment addition and relocation.

3.1.2.2.2 Power Subsystem

The Electrical Subsystem consists of the Solar Array (eight rectangular and sixteen trapezoidal solar panels), the Power Control Unit, an Event

Timer, a Battery Pack, and a battery pack Charge Control Unit. The Solar Array wiring will be modified to optimize the power for the Fan Beam Navigation Experimental Satellite. Four trapezoidal solar panels will be modified to allow the antenna support: to protrude through them. The Event Timer and the Charge Controller are new items. The Charge Controller **senses** battery voltage level, temperature, and pressure and through a logic network controls the charge to the battery. A high-rate discharge through a dummy load is controlled by the command system. This discharge reconditions the Battery Pack.

3.1.2.2.3 Telemetry Subsystem

The Telemetry Subsystem consists of a Telemetry Transmitter, a Telemetry Generator, and a DC/DC Converter. A Coax Switch and the Telemetry Antenna are shared with the Star Sensor Subsystem. Operation of either of these two subsystems is controlled by ground commands.

3.1.2.2.4 Star Sensor Subsystem

The Star Sensor Subsystem consists of a Star Sensor, an RF Bower Amplifier, a Power Amplifier DC/DC Converter, a Telemetry Transmitter, and a Telemetry DC/DC Converter. The latter two items are identical to corresponding units in the telemetry subsystem.

3.1.2.2.5 Fan Beam Transmission Subsystem

The Communications Subsystem consists of a DC/DC Converter, a Frequency Generator, an Exciter, two TWTAs, a TWTA/Antenna Switch, and four Fan Beam Antennas. Only the antennas are new items. The DC/DC Converter supplies power to the Frequency Generator, Exciter and the two TWTA's. The Event Timer controls the duration of RF emission.

3.1.2.2.6 Command Subsystem

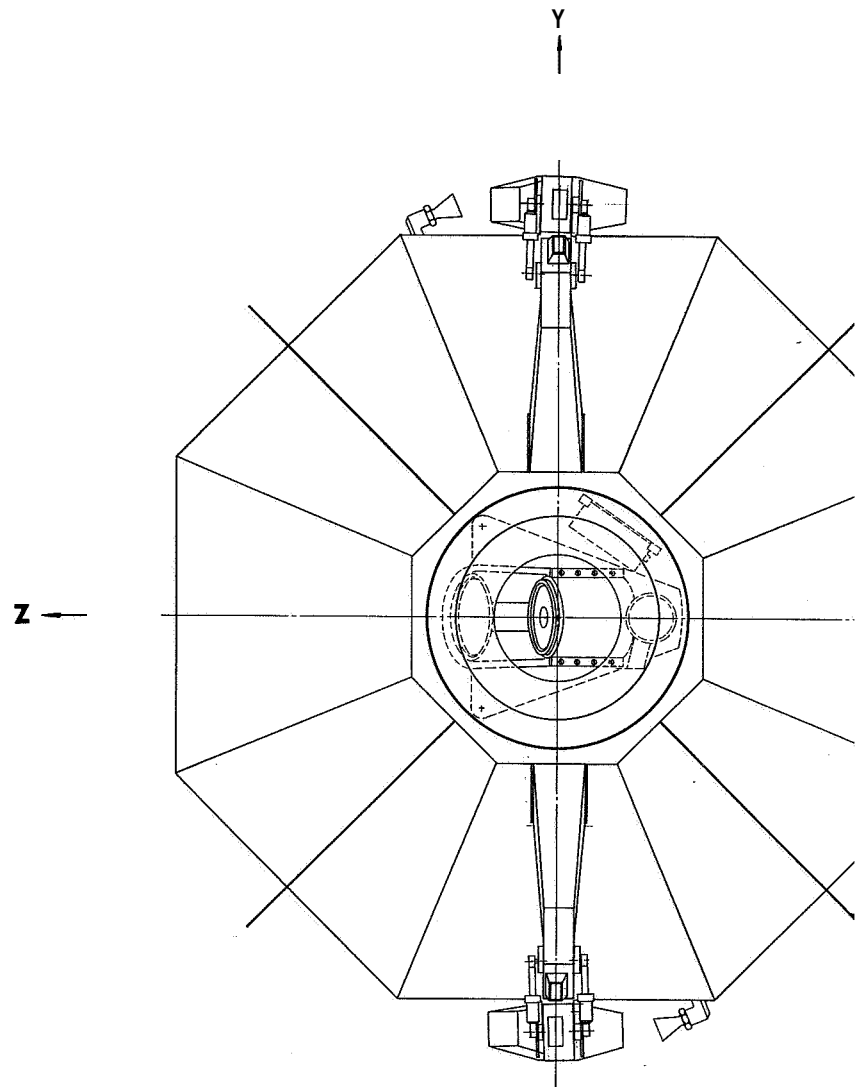
The Command Subsystem consists of four whip Command Antennas, a Command Receiver, a Command Decoder, and a Command Controller. Ground originated commands enter the receiver through the antennas. From the receiver, the signals go to the decoder which signals the controller. The controller switches power to the TWTAs through the TWTA control, cycles the batteries through the Charge Control, resets and starts the Event Timer, and controls the position of the TWTA/Antenna Switch.

3.1.2.2.7 General Configuration

The satellite, viewed along the spin axis, is octagonal in shape. The gas bottle for the spin-up gas is located in the aft end of the central cylinder along with the Nutation Damper and the Telemetry Antenna (see Figure 3-8, Sheets 1-4 inclusive). This star sensor mounts in the forward end of the central cylinder. The antenna switching unit is located in the mid portion of the central cylinder. Two antennas are mounted forward and two mounted aft on the plus and minus Y axes. Due to the moment of inertia imbalance, a maximum amount of equipment is located near the plus and minus Z axes. The mass properties including ballast weights are as follows:

| | |
|-----------|---------------------------|
| Weight | 150 lbs |
| \bar{x} | 0.0 in |
| \bar{y} | 0.0 in |
| \bar{z} | 0.0 in |
| I_x | 22,340 lb-in ² |
| I_y | 20,730 lb-in ² |
| I_z | 20,780 Lb-in ² |
| I_x/I_z | 1.075/1 |

The nominal spin rate (assuming a 35°F gas temperature) is 100 rpm using a mixture of N₂ and Freon-14 to obtain the total impulse.



3-16-1

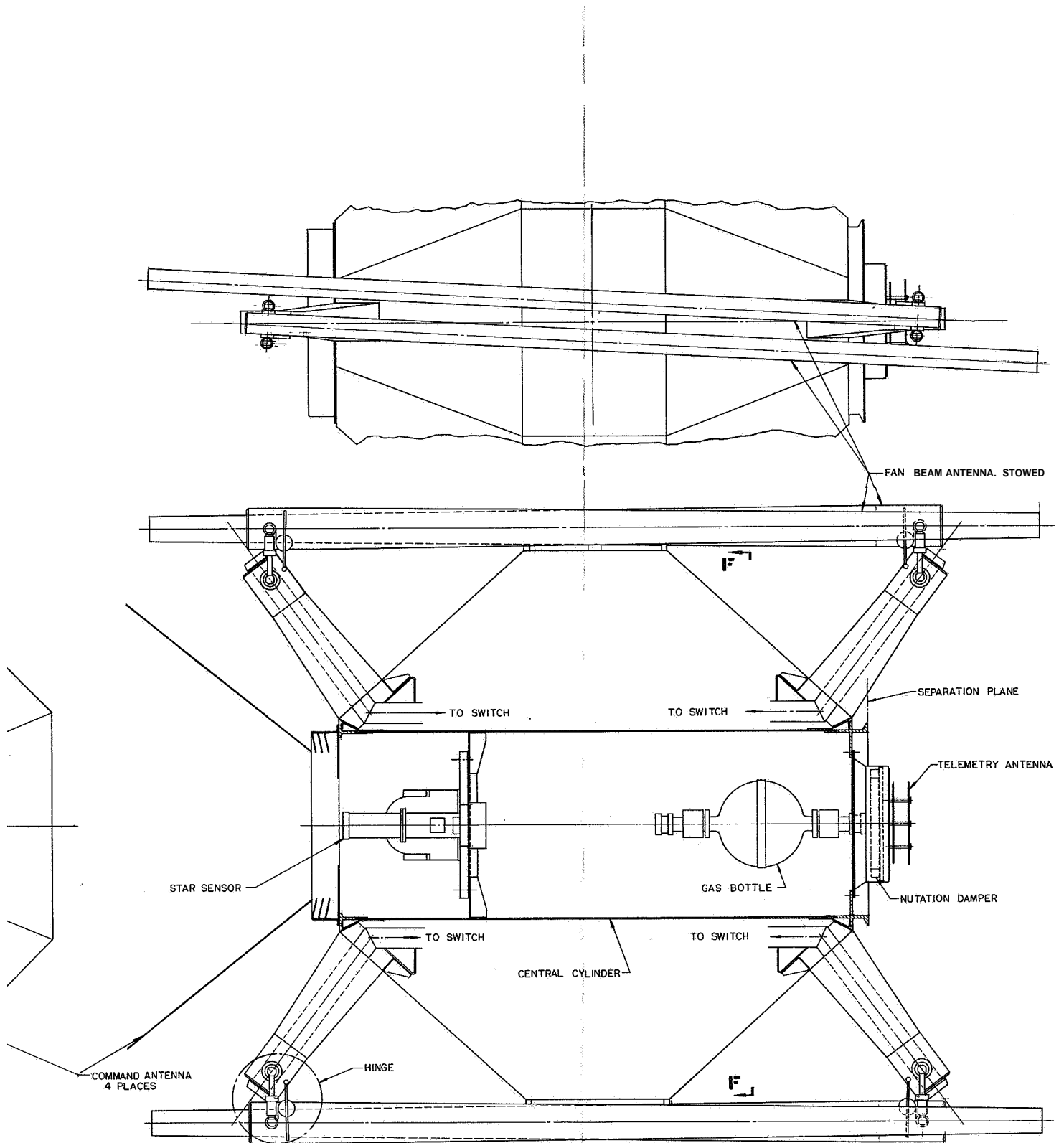
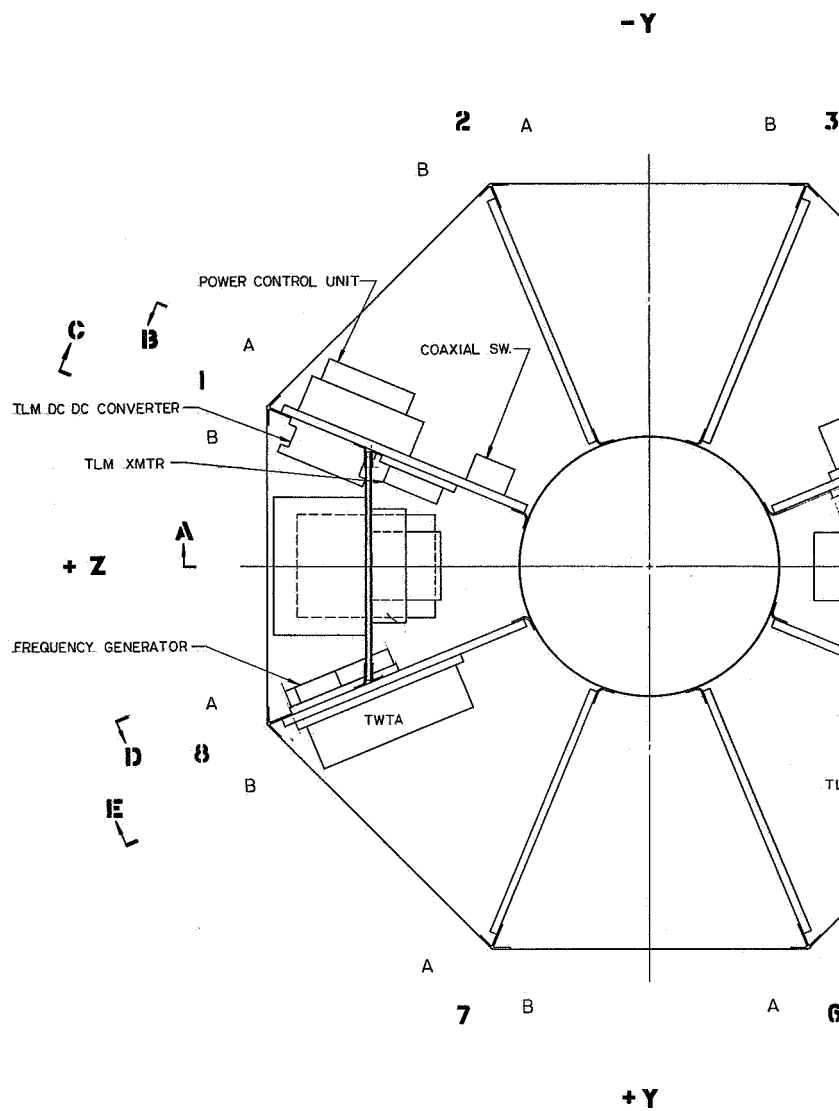


Figure 3-8 Satellite General Arrangement (Sheet 1 of 4)

3-16-2



SECTION **F-F**

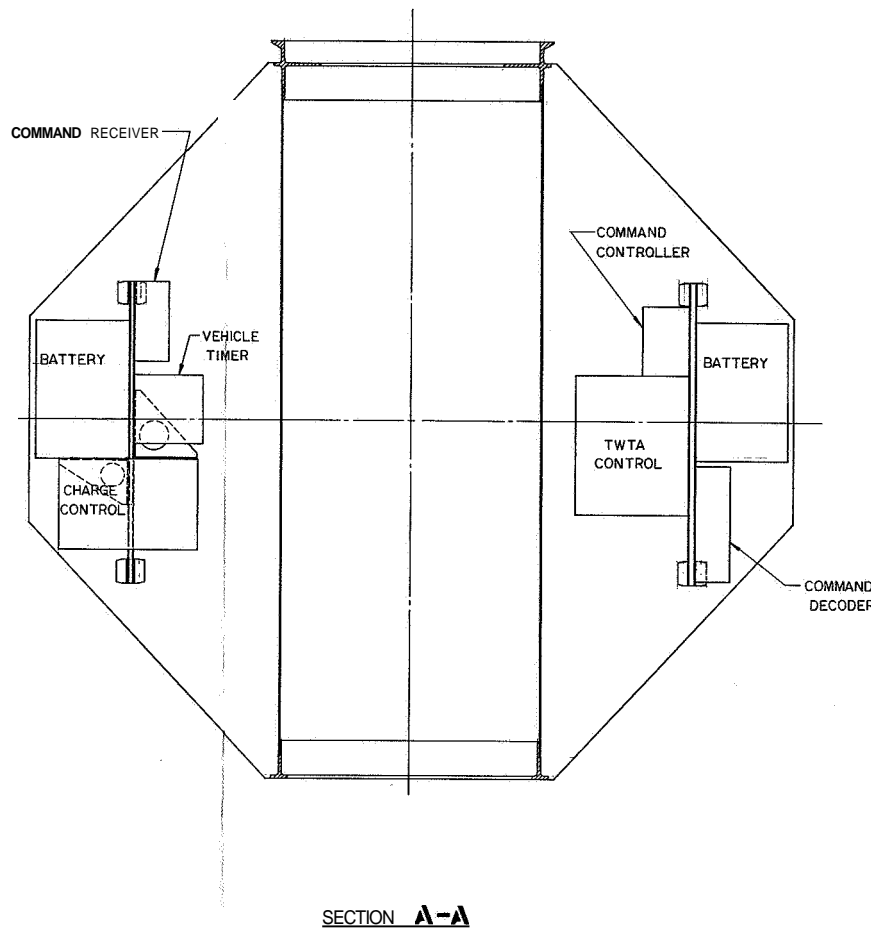
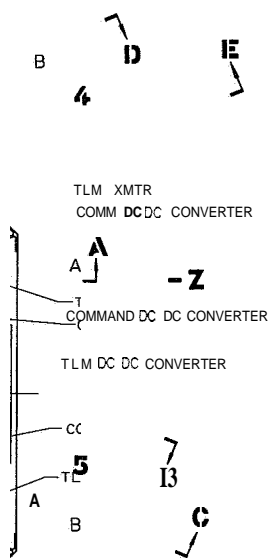


Figure 3-8 Satellite General Arrangement (Sheet 2 of 4)

3-17-2

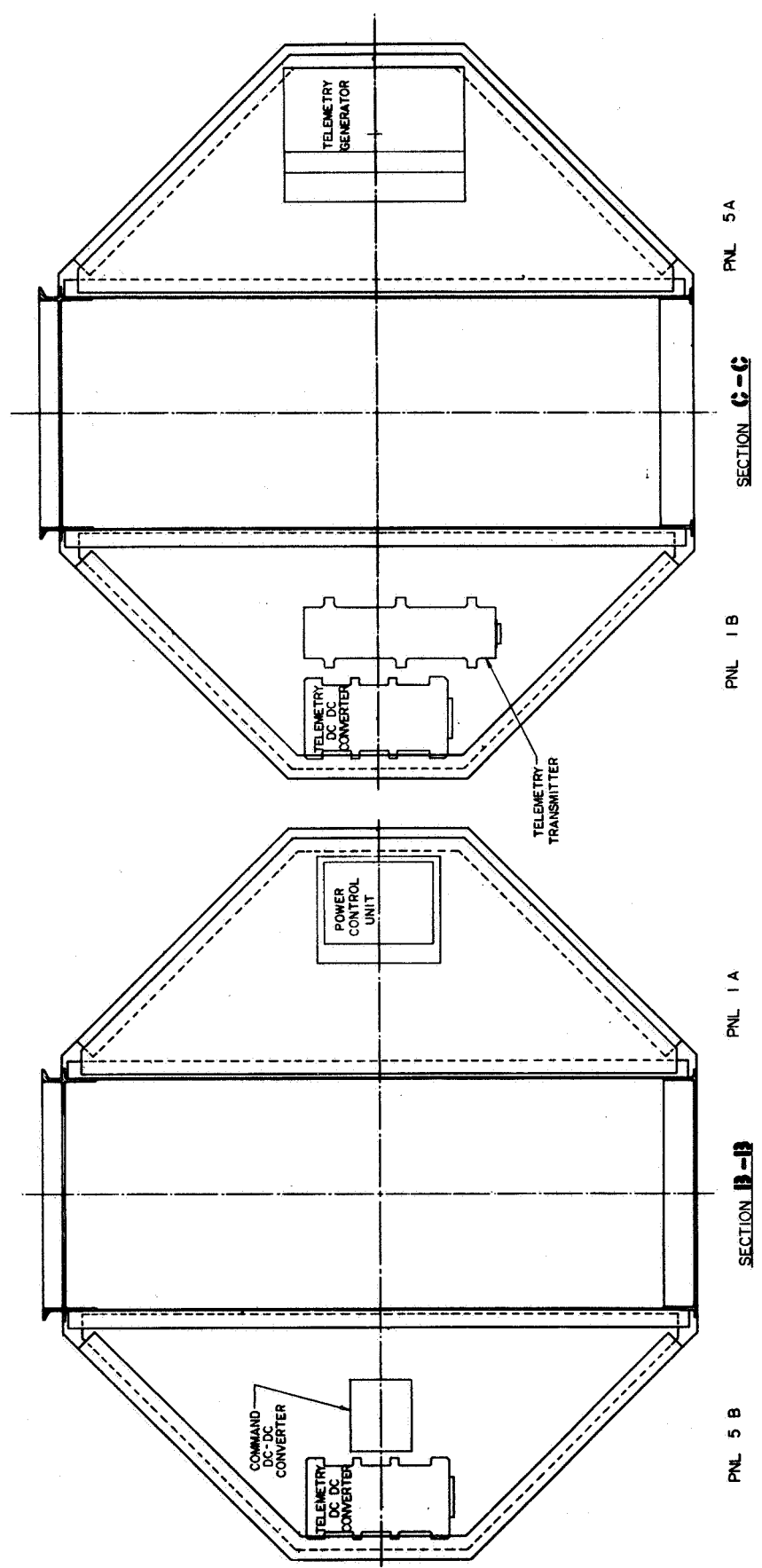


Figure 3-8 General Satellite Arrangement (Sheet 3 of 4)

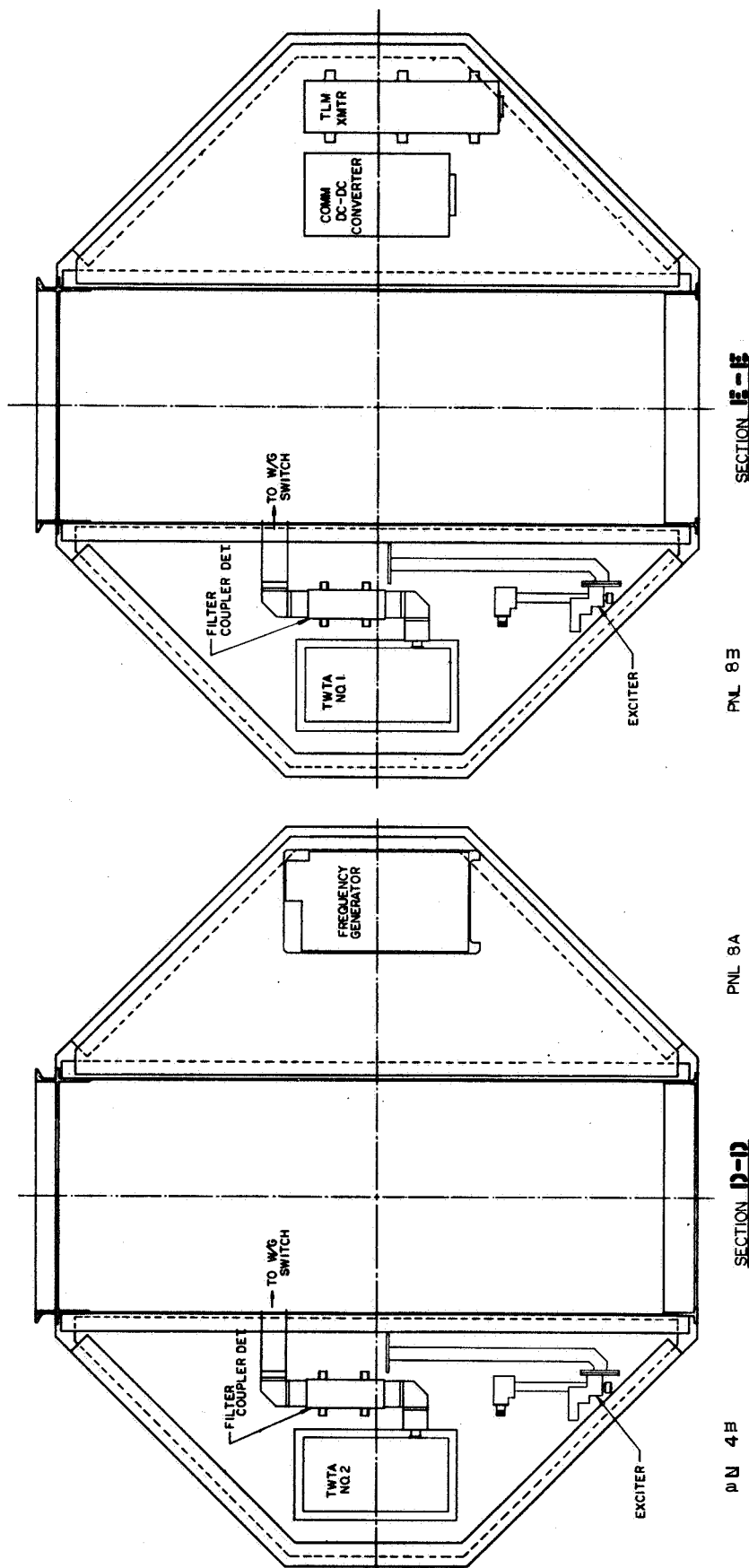


Figure 3-8 General Satellite Arrangement (Sheet 4 of 4)

3.1.3 Antenna Electrical Design

The proposed experiment will consider location accuracies resulting from various detection schemes made on three different radiation patterns developed by "fan beam" antennas. The term "fan beam" includes a broadside plane of zero or maximum field intensity on both sides of which are major or minor lobes respectively. The three different patterns are identified by modes. The modes of operation are controlled by an RF switching arrangement which is actuated by ground signals received by an omnidirectional 150 MHz antenna to be developed.

Mode A operation directs 8.0 GHz CW energy to two linear resonant arrays identical in all dimensions, Antennas Nos. 1 and 2 on Figure 1-1. These arrays lie in a plane on diametrically opposite sides of the satellite such that their extended longitudinal axes are parallel and make an angle of 45 degrees to the satellite spin axis. The radiated energy from the two arrays is oppositely directed, such that from the ground the pattern from only one array at a time is observed as the satellite spins. The shape of the radiation pattern is a fan beam with approximately a 100-degree beamwidth to the 3-dB points in the plane of the fan and a 3-dB beamwidth of 51st in the orthogonal plane.

Mode B operation directs the energy to the two remaining arrays, Antennas Nos. 3 and 4 on Figures 1-1, which are similarly oriented about the satellite in the same plane. The No. 3 array is given a uniform aperture amplitude distribution like the No. 1 and No. 2 arrays, but instead of a constant phase distribution, a 180-degree phase reversal is given to one half of the length of the array. On a resonant slotted waveguide array the element spacings are one half of the guide wavelength at the resonant frequency, Through a half wavelength of line, the phase changes by 180 degrees. An additional 180 degrees of phase shift is added by placing the longitudinal shunt slots on the opposite side of the waveguide longitudinal center line. Alternating successive elements provides a constant phase across the aperture at half wavelength spacings. If, at the midpoint of the array, which

must contain an even number of elements for the two halves of the array to radiate with equal amplitudes, the element alternating sequence on the short-circuited end is a mirror image of that on the input end, an array is produced which has a 180-degree phase reversal at its midpoint. Even symmetry is seen to exist about the midpoint. Odd symmetry exists for a constant phase aperture for an even number of elements. Figure 3-9 illustrates the alternating sequence for a constant phase aperture and for a 180-degree phase reversal, Operation of Antenna No. 4 is similar to that of Antenna No. 3 and differs only in the number of elements which are assigned the phase reversal, It can be shown that for this aperture phase distribution, there exists only one unique plane containing zero field strength. The pattern is likewise symmetrical about $\theta = 0$ in the $\phi = 0$ plane. With this pattern shape there can be no question or ambiguities concerning which null is used as the reference time for location purposes.

Various types of antenna patterns have been studied in detail during this extent of this study. Results of these pattern studies are presented in Volume III.

Figure 3-10 is a typical antenna pattern for a cross section as viewed by a navigator crossing the No. 1 and No. 2 beams at an angle of 45° . Amplitude detection would be used for purposes of determining the beam center in Mode A operation.

Figures 3-11 and 3-12 show the typical antenna pattern cross sections as viewed by a navigator crossing the No. 3 and No. 4 beams at an angle of 45° respectively. Null detection would be used for determining the beam centers in this Mode B operation, The absence of nulls in the vicinity of the central null make antenna pattern No. 4 more attractive for null detection than antenna pattern No. 3. These two different types of null patterns should provide excellent data for evaluating various null detection techniques.

All of the arrays will be fabricated in a waveguide equivalent **in** inside dimensions to WR112. The waveguide will be enclosed on three sides by a rigid honeycomb structure. The fourth wall will contain the radiating **slots**.

The latching wedge mating junction between the arrays and the feed lines **is** described in Section 3.1.2.

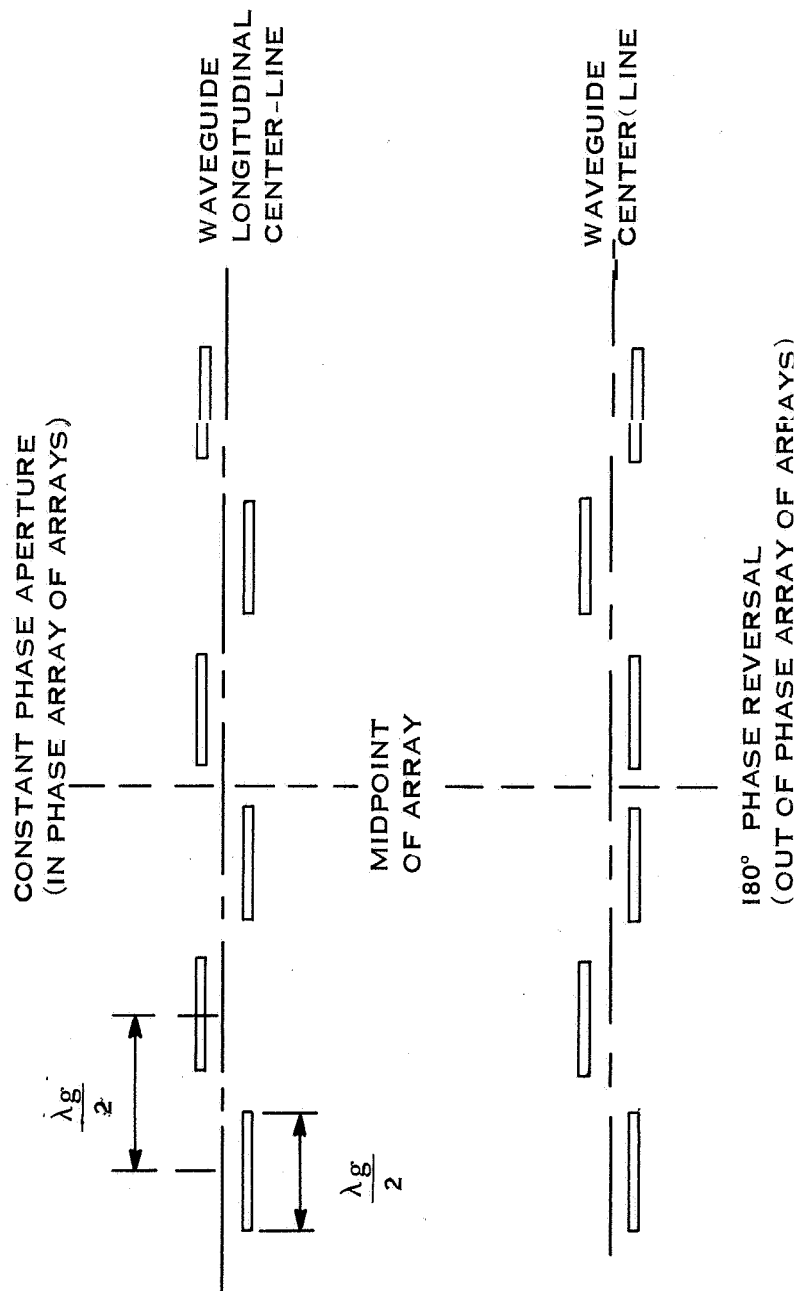


Figure 3-9 Schematic of Slot Arrangement for Constant Phase and Out-of-Phase Arrays

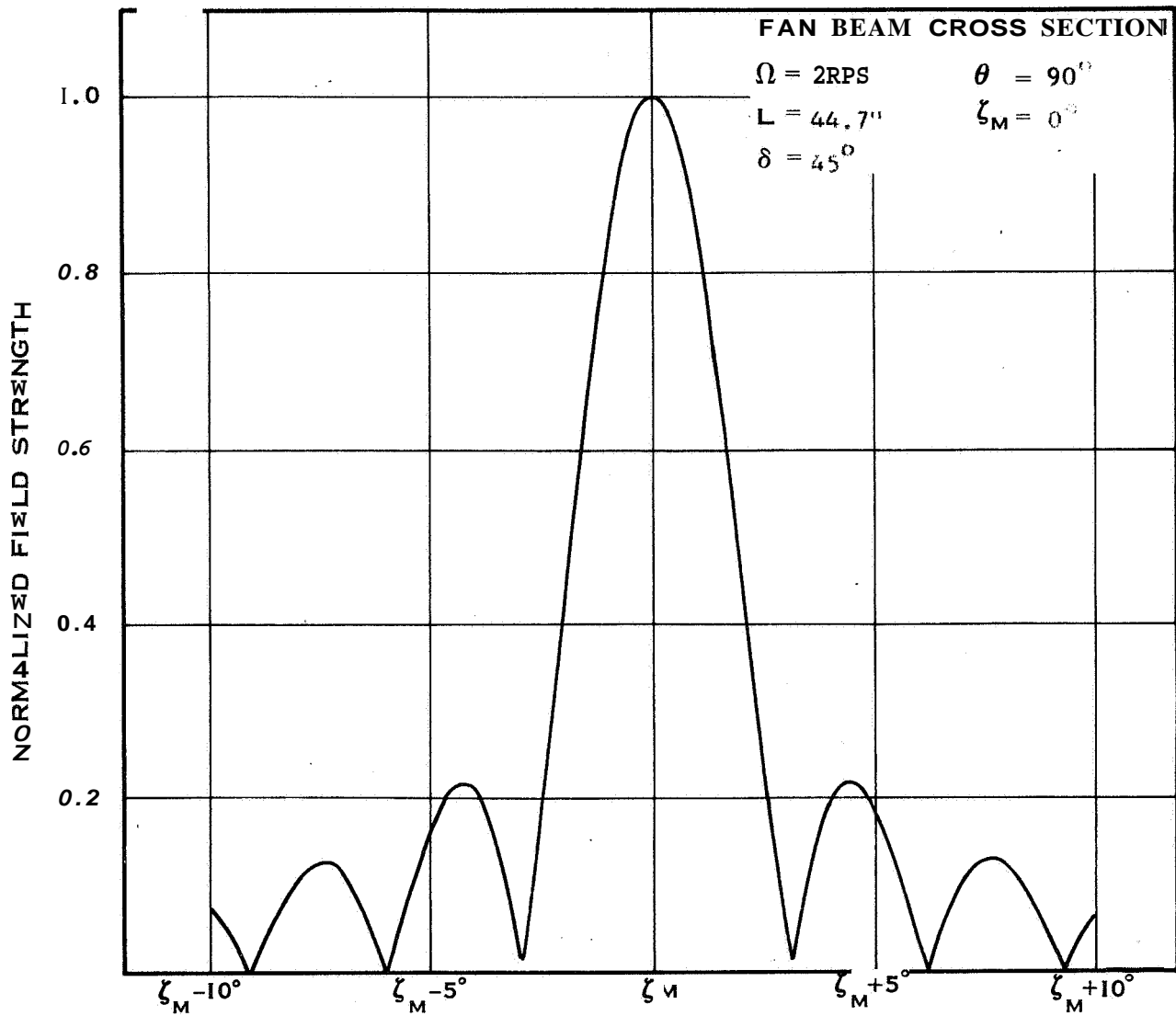


Figure 3-10 Cross Section of Antenna Pattern Nos. 1 and 2

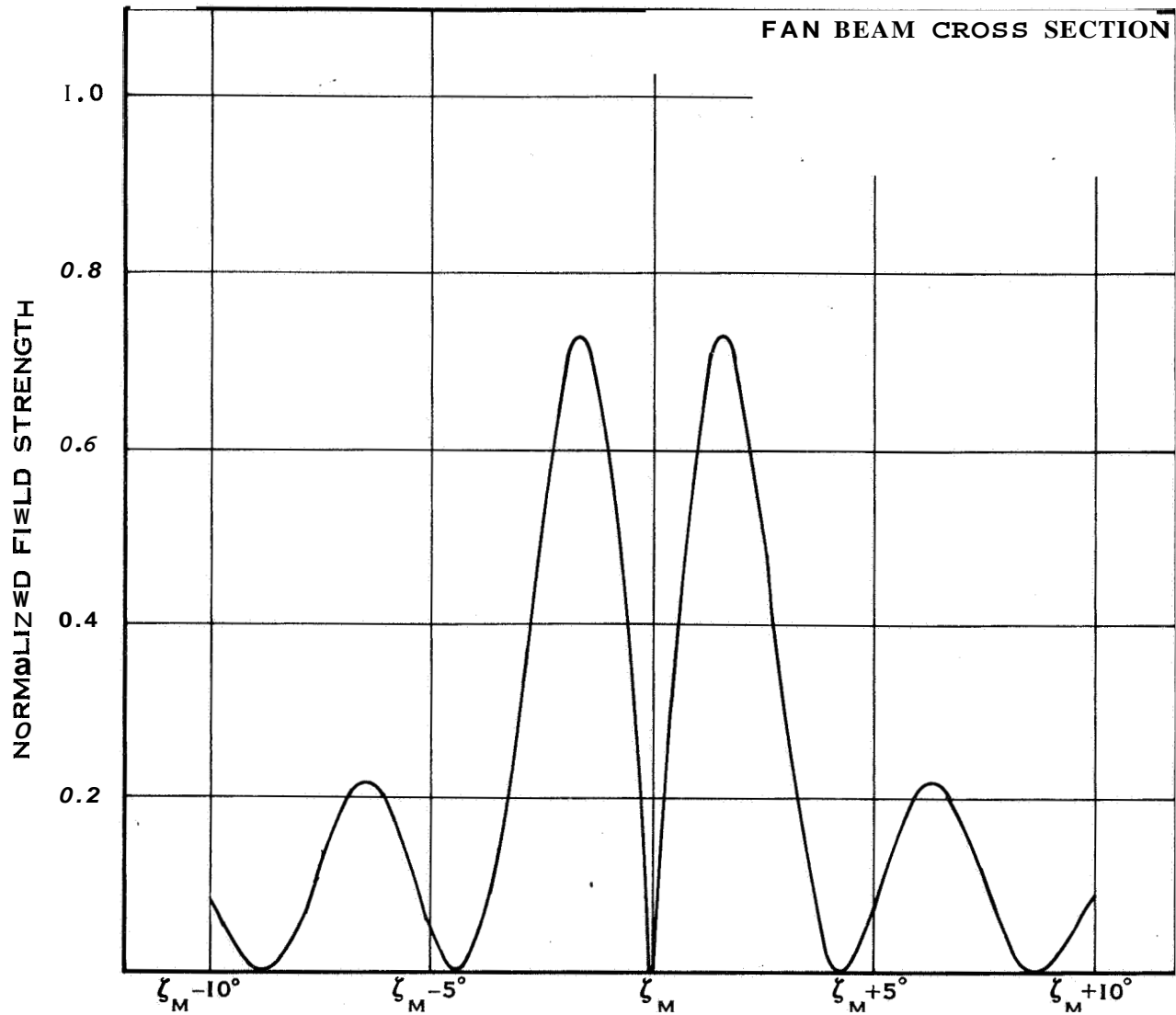


Figure 3-11 Cross Section of Antenna Pattern No.3

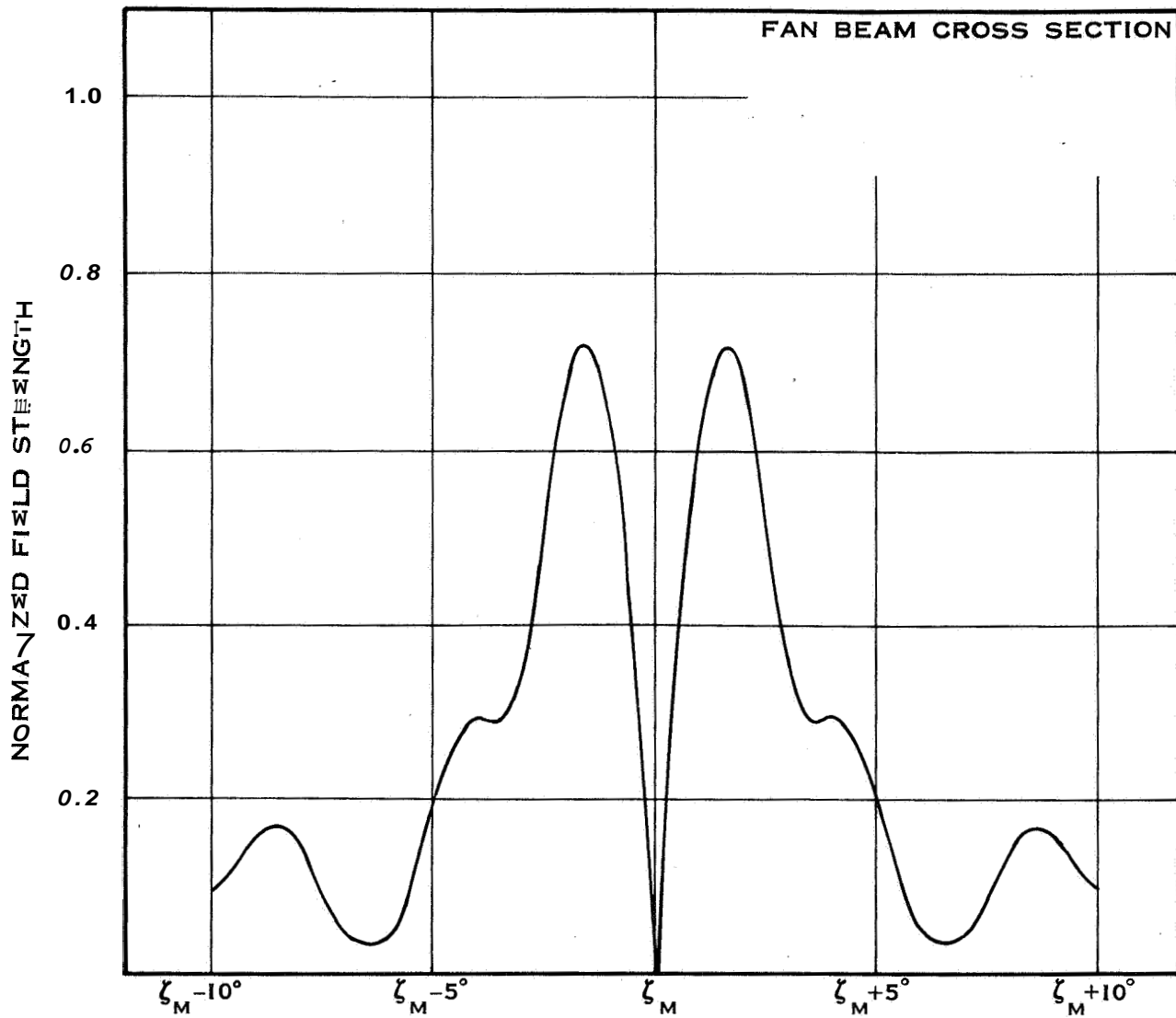


Figure 3-12 Cross Section of Antenna Pattern No.4

3.2 STAR DETECTOR DESIGN INTEGRATION

3.2.1 NavSat Star Detector System

A schematic of the star detector is shown in Figure 3-13 and an outline drawing in Figure 3-14. The device is mounted close to the spin axis, looking 48° south of the satellite equator. If the satellite spin axis is inclined approximately 5° to the ecliptic, the star field swept by the 5° field angle of the lens will vary with the season between 43° and 53° south of the ecliptic plane. This region is comparatively rich in stars brighter than +3 magnitude, as shown in Table 3-1.

The star detector look-angle will be oriented to avoid sunlight reflected from the extended antenna arms. The relation of the detector port to the sun is such that a spin axis inclined as much as 10° to the ecliptic can be tolerated. If the error angle is greater than this, sunlight can penetrate the port for a length of time which will depend on the season and the inclination of the spin axis. An automatic sun shutter will be provided to avoid damage to the star detector during the period of exposure to excessive light.

The star detector operates by imaging a star in the plane of a reticle; as the satellite rotates, image energy crossing and passing through the reticle pattern is detected by a photomultiplier tube. The reticle pattern is designed to encode the crossing position and angle of the star, relative to the optical axis of the detector, which is itself calibrated to the vehicle axis. A typical reticle pattern is shown in Figure 3-15. The exact configuration and dimensions used will be determined by the data handling plan adopted, and the image-forming characteristics of the optical system. As an example, a 2-arc-minute reticle opening at a vehicle rotation rate of 100 rpm would give a star pulse of 55.6 μ sec duration. Pulse rise time is dependent on the size of the star image blur circle.

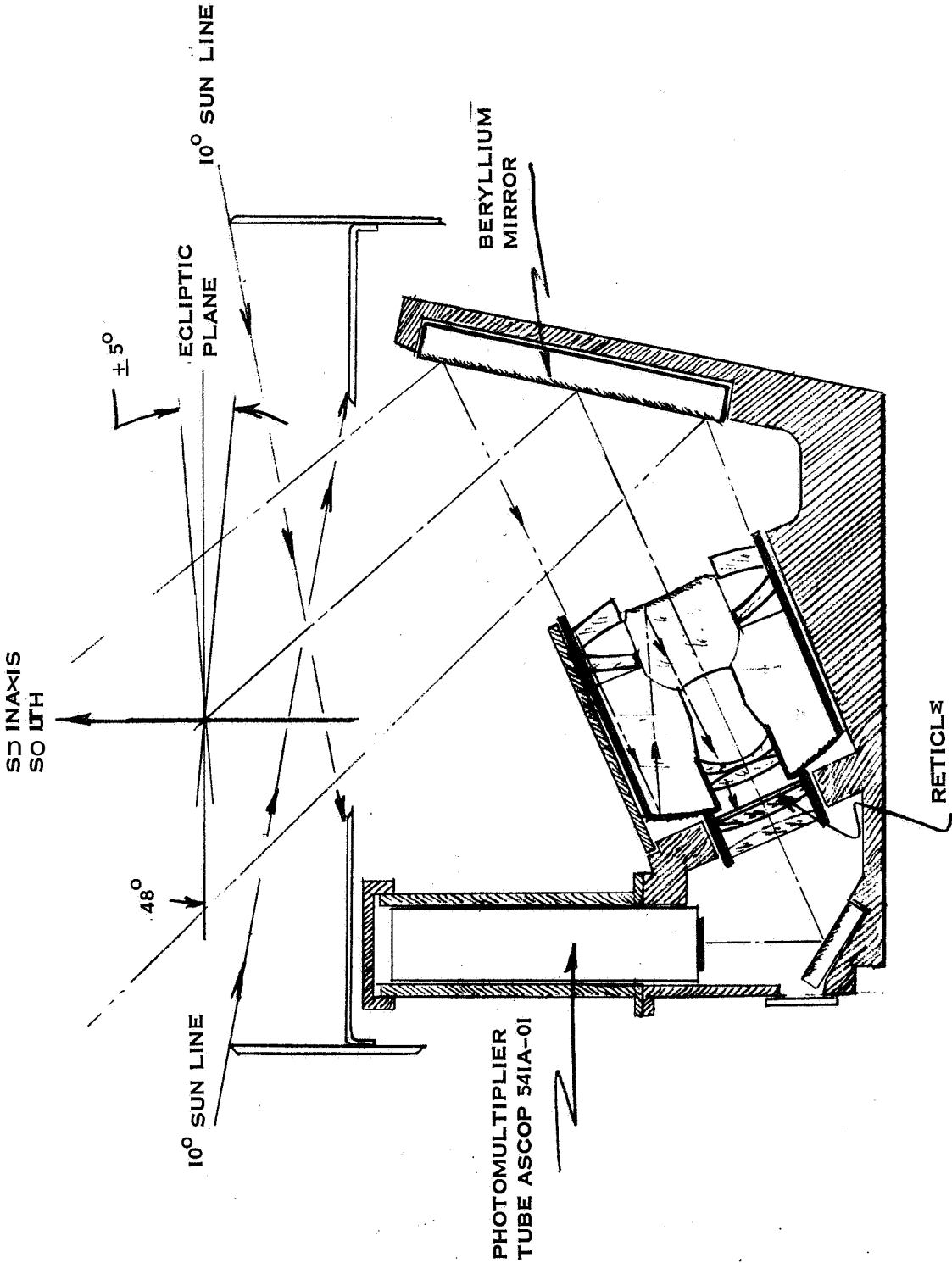
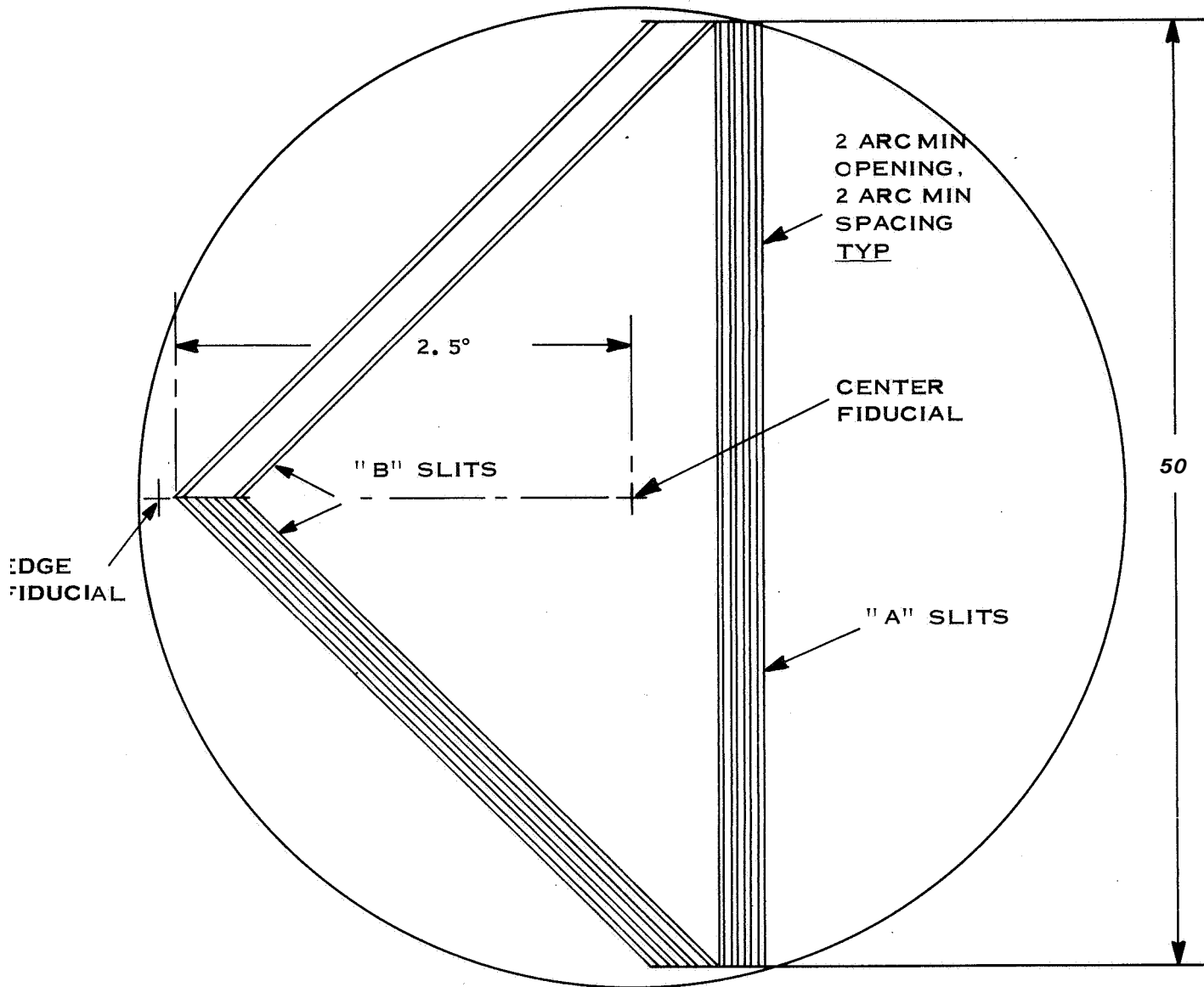


Figure 3-13 Star Detector Schematic



- NOTES:**
1. AXIS OF ROTATION IS PARALLEL TO "A" SLITS.
 2. "B" SLITS ARE ARRANGED TO COVER MAXIMUM FIELD ANGLE OF LENS, WITH ABOVE AND BELOW OPTICAL AXIS CODING.
 3. RETICLE IS OPAQUE EXCEPT FOR SLITS AND FIDUCIAL MARKS.

Figure 3-15 Typical Reticle Pattern

Table 3-1 Stars Brighter Than $M_V + 3$, 43° to 53° South of Ecliptic Plane

| Star | M_V | RA | | Declination (Epoch of 1900) |
|-----------------|-------|----|----|--------------------------------|
| | | h | m | |
| α Phe | 2.37 | 0 | 21 | $-42^\circ 51'$ |
| ϵ C Ma | 1.48 | 6 | 55 | $-28^\circ 50'$ |
| δ C Ma | 1.85 | 7 | 04 | $-26^\circ 14'$ |
| η C Ma | 2.42 | 7 | 20 | $-29^\circ 06'$ |
| β Cent | 0.63 | 13 | 57 | $-59^\circ 53'$ |
| α Cent | -0.27 | 14 | 33 | $-60^\circ 51'$ |
| α Tr A | 1.93 | 16 | 38 | $-68^\circ 51'$ |

The lens type selected for the NavSat Star Detector is capable of resolving 100 percent of the image energy in approximately a 30 arc second disc, over a spectral range of **0.38** to **0.68** microns; pulse rise time would be in the order of **13.9** μ sec. Geometrical image distortion, i.e., the aberrational displacement of an image point from its true angular position in object space, would not exceed **20** arc seconds over most of the **5°** field, or **25** arc seconds at the edge of the field. The accuracy of the reticle lines in straightness, spacing, and angle to one another can be held to ± 2 arc seconds or less. It should be noted that these are fixed, repeatable position errors, and total at most about ± 4 arc seconds. Thermal and dynamic error contributions could add something in the order of ± 6 arc seconds, for an inherent optical system total ± 10 arc seconds.

Tentatively, the detector selected is the **ASCOP 541A-01-14** photomultiplier, a rugged, space-proven tube with an S-11 response. The detector has **14** stages, with a dark current 2×10^{-9} amperes at a gain of 10^6 . The cathode sensitivity is 60 μ a/lumen.

The signal-to-noise ratios corresponding to a 2.4-inch clear aperture (**29 cm²**) for nominal gain, tube noise, and sky background for different magnitudes are :

| <u>Star M</u> | <u>S/N</u> |
|---------------|------------|
| 3 | 3.5 |
| 2 | 89 |
| 1 | 22.8 |
| 0 | 54.3 |

This is a generalization, which would be modified for specific stars. The electronics bandpass for the NavSat Star Detector is **6 kHz/s** to **18 kHz/s** and must provide a linear dynamic range of 1 volt for identifying star magnitude. System linearity will establish star intensity to 10 percent,

Studies conducted at Philco WDL on star detection systems of this class, trading off the number of stars observed per cycle against the data processing manipulations required, show that the identification of only three or four stars is necessary for establishing vehicle orientation. Thus, although +3M stars would be within the signal-sensing threshold of the detector, the system threshold would be set at 6/1 signal-to-noise ratio to reduce the complexity of the data pre-processing needed for detecting useful pulse trains,

3.2.2 Details of Design and Construction

3.2.2.1 Optical System

The telescope lens will be a solid catadioptric of fused quartz. Since image formation will be based primarily on mirror surfaces, color aberration can be kept low. Quartz is highly resistant to radiation browning effects and the attendant changes in refractive index, which reduce energy transmission and degrade image quality in the common optical glasses. Quartz also has excellent thermal characteristics.

Although the effective focal length will be about 9.6 inches, the catadioptric design permits folding the rear conjugate distance, from the front lens vertex to the focal plane, into less than 3.5 inches, providing a very compact package. This design also permits the use of a much shorter and lighter structure than would be normal for a lens of this focal length. The lens will be in its own cell, which will be installed in turn in the telescope mount.

The reticle in the focal plane will be produced by a photoresist or by engraving, depending on the final design. The opaque part of the reticle (Figure 3-15) will be an evaporated metal deposit, about 0.75 inch in diameter. The reticle will contain several fiducial marks for establishing an optical axis for the system, and for orientation and calibration measurements during assembly and checkout ■

Image energy passing through the clear spaces in the reticle will be transferred through a field lens system which images the lens aperture of the telescope onto the photocathode, through a small folding mirror.

The telescope will view the star field through a beryllium mirror of optical quality, the surface of which will be Kaniginized, aluminized, and over-coated with silicon monoxide. The mirror mount will be an integral part of the telescope lens mount casting, and will be supported at the center and sides by webs extending from the lens mount. The optical alignment of the telescope lens cell and its mirror will be rigidly maintained by the design of the structure and the placement of mirror pads to reduce thermal and mechanical movements and distortion. The casting design will prevent flexure of the system under rotational forces.

The photomultiplier tube housing and shield will be located at the rear of the telescope casting. Alignment of the photomultiplier is not critical, since the star energy is spread in a diffuse disc covering the one-inch-diameter photocathode to minimize the effects of uneven cathode sensitivity.

The telescope casting will be attached to pads in a Hexcell plate, which in turn will be mounted at three points to a flange in the satellite core cylinder. A short shroud extending beyond the end of the core cylinder will enclose the Star Detector. A cap plate with an elliptical port will be located 1.5 inches below the edge of the shroud. The rim thus forms a shield for the open port against sunlight up to 10° off the ecliptic. During part of the rotation, the sun can illuminate the inner side of the rim, and secondary reflected light can be seen by the mirror. Although this reflection is off-axis to the telescope, enough diffuse light could enter the system to reduce the signal-to-noise ratio. Three knife-edge baffles will be added to the rim to attenuate such reflections.

Interior and exterior surfaces likely to reflect glare light will be finished with 3-M Optical Black Paint, used for this purpose in previous space applications ■

Prior to launch, the telescope port will be sealed by an expendable cap, which will be released by a solenoid when orbital position and spin are attained and prior to antenna extension. If the design attitude is not

achieved, and excessive light of a predetermined level enters the port, a silicon detector cell near the top of the mirror mount will actuate a sun shutter through a bi-directional rotary solenoid. The shutter will remain closed until opened by a down-link command. Opening and closing will require about 1.5 watts of power for 100 μ sec. The sun shutter will be situated in front of the reticle, to prevent a focused sun image from damaging the reticle.

3.2.2.2 Assembly

The only critical part of optical assembly will be in positioning the reticle in the focal plane and orienting the vertical reticle openings with reference to the base of the telescope casting. This will be a relatively simple operation, since the reticle will be in a separate cell which will slide into a short tube at the rear of the lens, where it will be locked into the correct position.

Fiducial openings in the center of the reticle and the front mirror of the lens will define the optical axis, the line of which then can be established in relationship to the base of the casting. The beryllium mirror will be placed in its mount at the correct angle to the telescope axis. Focus and alignment will be done with a star target in a collimator, and by observing the image in the reticle plane through a microscope.

In turn, the base of the casting with its mounting plate will be calibrated to the designated spin axis of the vehicle during final assembly. This latter calibration need be accurate only to + 15 arc minutes, to be within the uncertainty of the operational spin axis. Aligning the star detector to the satellite axis may be done by simple leveling techniques; flats on the telescope casting referenced to the optical axis will facilitate this ,

3.2.2.3 Detector and Signal Processing Electronics

Various means for accomplishing the four main functional elements (video amplifier, high-voltage power supply, automatic gain control, and command turn-on) of the star detector electronics subassembly have been investigated. In this process, the basic scheme **as** proposed **was** also re-evaluated. Figures 3-16, 3-17 and 3-18 represent the current state of evolution of the electronics package. The block diagram, Figure 3-16, shows that the basic scheme has not changed. The schematic diagram of the video and AGC amplifiers, Figure 3-17, has changed in some details. The converter schematic, Figure 3-18, has changed in detail, but not in function.

Video amplification will be achieved by three **SE501** units. The Signetics **SE501** is a general-purpose, direct-coupled, wideband amplifier fabricated within a monolithic silicon substrate by planar and epitaxial techniques. The **SE501** offers low power consumption, excellent overload recovery, small size, good stability and low cost. The **SE501** also offers excellent noise performance, 4 db in the region of interest. The system noise figure will not be degraded by the video amplifier noise. Transformer coupling at the input achieves phase inversion, since the **NPN** structure of the **SE501** performs better with positive-going pulses. The transformer also offers an opportunity for optimizing the noise performance at the input without altering the DC conditions at the **PMT** mode. The video bandwidth is controlled by an **RC** highpass at the input to the third **SE501**, and an **RC** lowpass within the third **SE501**, just before the output emitter-follower.

Amplification within the **AGC** section will be achieved by two **μA702A** circuits. The Fairchild **μA702A** is a complete DC amplifier constructed on a single silicon chip, using planar epitaxial processes. It is intended for use **as** an operational amplifier **in** high-speed analog computers, as a precision instrumentation amplifier, or in other applications requiring a feedback amplifier useful **from** DC to 30 MHz. The first part of the **AGC** section is a precision peak detector whose charging time constant **is**

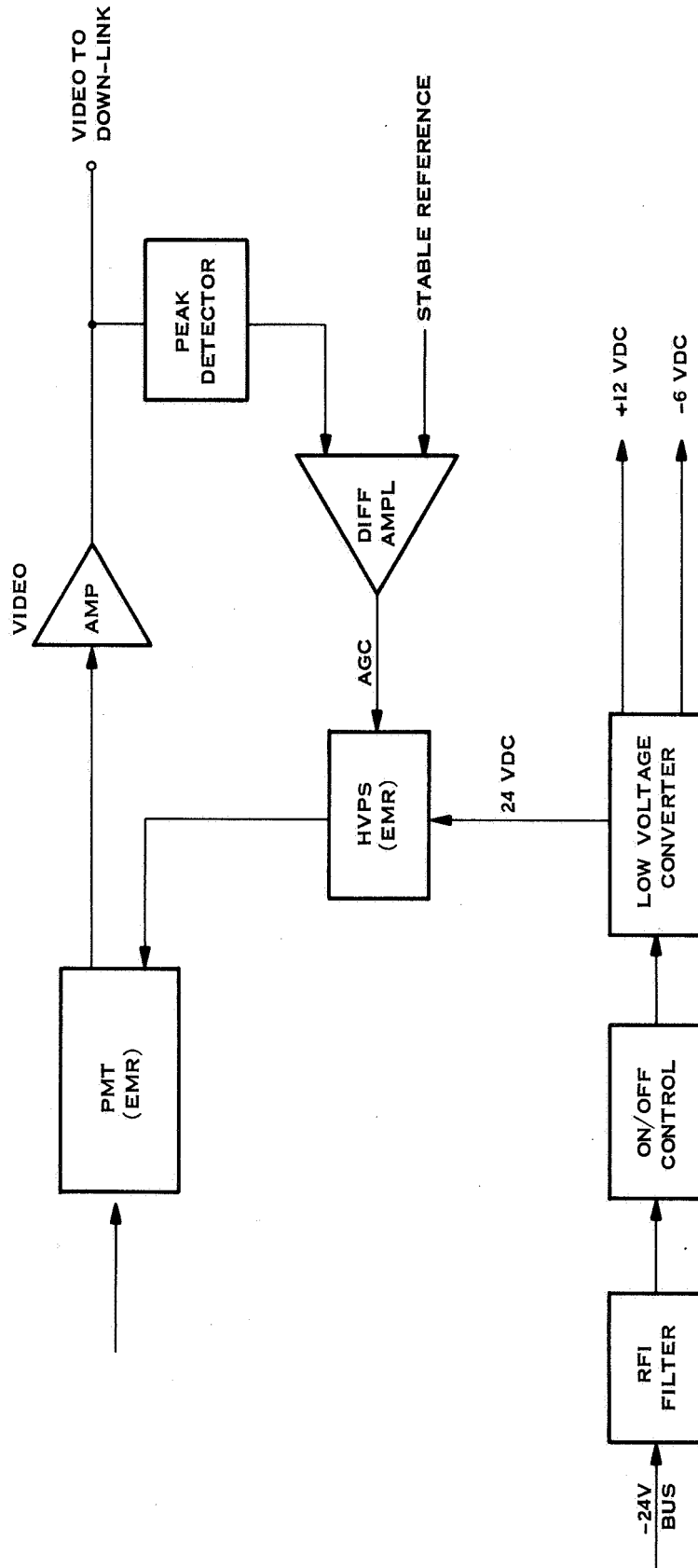


Figure 3-16 Star Detector Electronics Block Diagram

Figure 3-17 Star Detector Video Amplifier and Pulsed AGC Schematic

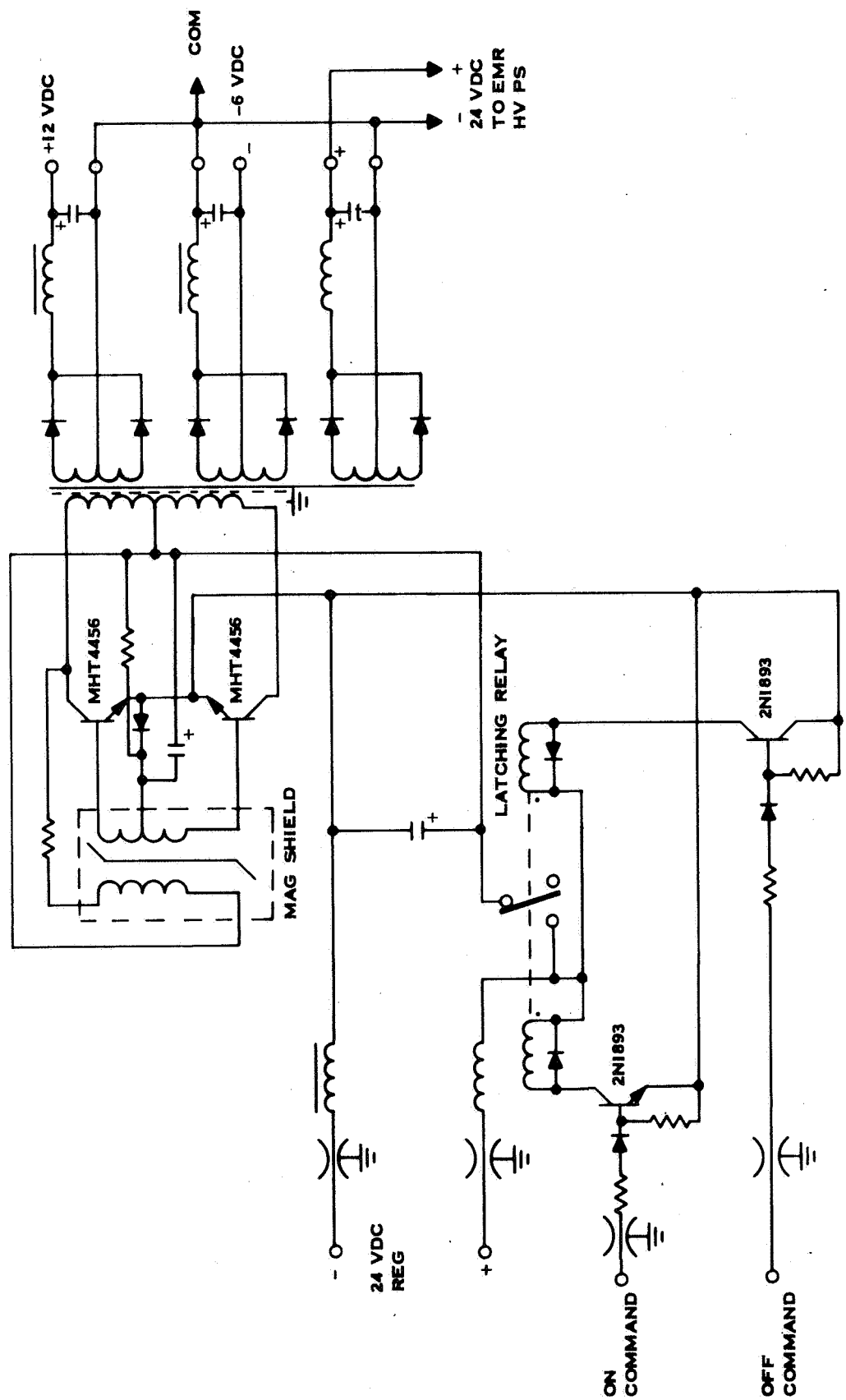


Figure 3-18 Star Detector Low-Voltage Converter Schematic

short compared to a star image pulse, and whose discharge time constant is very long compared to the spin period. To preserve this discharge time constant, a high-impedance differential stage is needed. This may be mechanized as shown with a matched pair of high-beta emitter-followers, or by employing an SH2000, which is a μ A702A with the emitter-followers built in. The reference voltage is generated by a precision zener diode. A T-pad attenuates the zener voltage the desired amount, while maintaining the desired 200K ohm impedance level. The AGC output voltage is zero when the peak-detected voltage equals the reference, and goes positive or negative for video peaks larger or smaller than standard. Modification of the EMR power supply to add AGC control turned out to be simple and straightforward, as expected. Drift and offset of the precision peak detector and differential comparison stages are negligible, and likely to remain so for the life of the experiment.

An EMR high-voltage power supply has been procured and tested, and the design, quality of parts, and workmanship appear to be satisfactory for this application. A high-temperature full-load stabilization period of around 350 hours is recommended by reliability. The data obtained from continuously monitoring this test will establish the drift characteristics of the unit. A good (that is, unlikely to fail) high-voltage power supply will exhibit a stable or very low drift rate with no discontinuities. The low-voltage converter, detailed in Figure 3-18, is to use a magnetic latching relay for command turn-on and off. This device supplies at no power the required command status memory. The relay proposed for this application, developed for another high-reliability satellite, is a General Electric Style 3SAM, modified to withstand a high-shock environment. The power oscillator will be of the two-transformer type for maximum efficiency. Primary power for the EMR high-voltage converter is supplied by the low-voltage converter. This allows the negative power lead to the EMR wire to be connected to signal ground, as required for automatic gain control. An electrostatic shield in the converter output transformer completes the isolation from the line.

Figure 3-19 is an outline drawing of the ERM high-voltage supply.

Figure 3-20 shows the proposed package for the remaining electronics.

3 2 24 Command and Other Electronics

Apart from the automatic sun-shutter activation by excessive light, turn-on and turn-off of the Star Detector is controlled from the ground station by means of the command subsystem. Only two commands are needed: "on" and "off." The command interface, as shown in Figure 3-18, is quite simple. If the expendable lens cap has to be held in place for a period after the shroud is removed, an additional command is required.

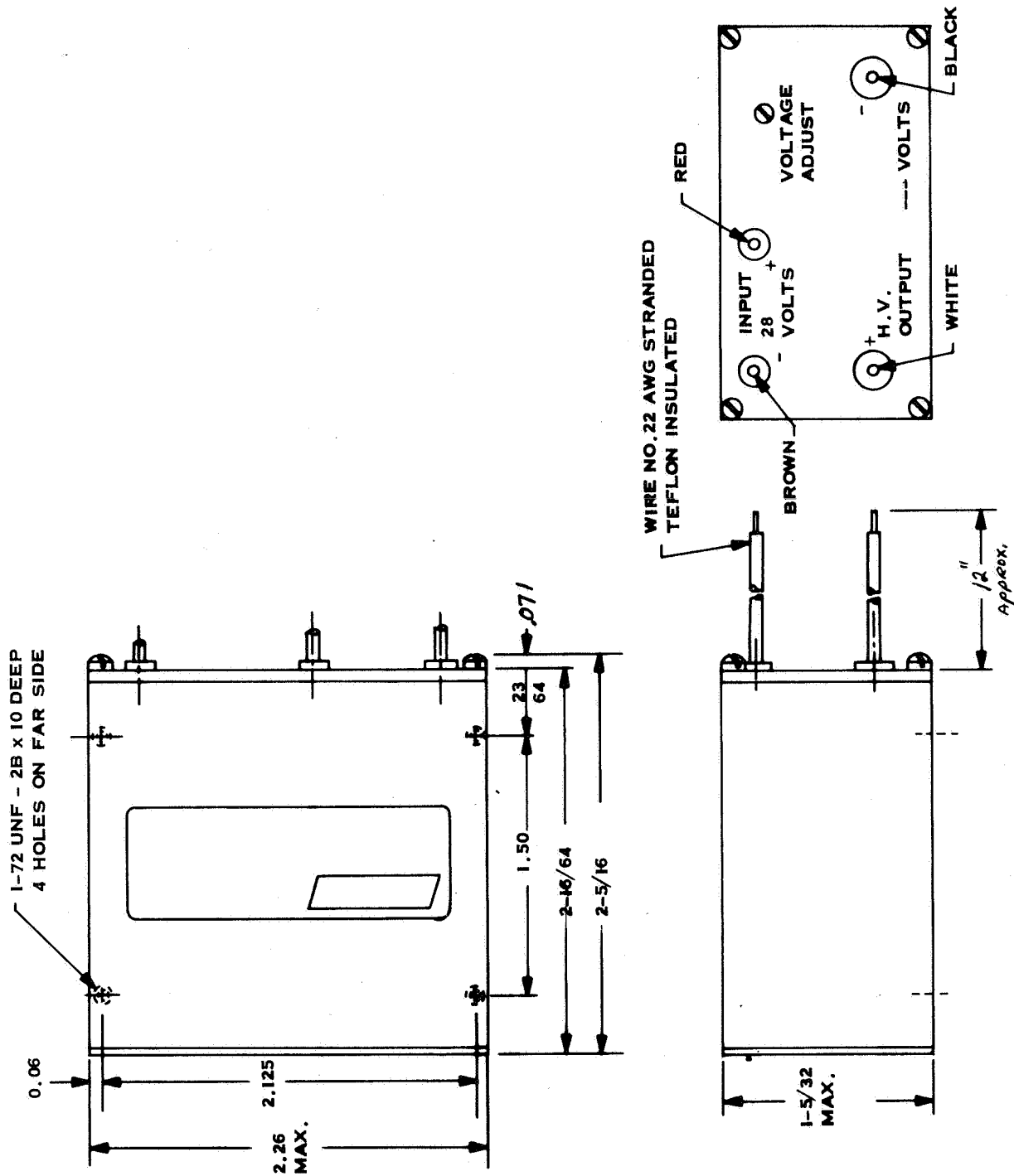


Figure 3-19 Outline Drawing of EMR Model 1 640C High-Voltage Supply

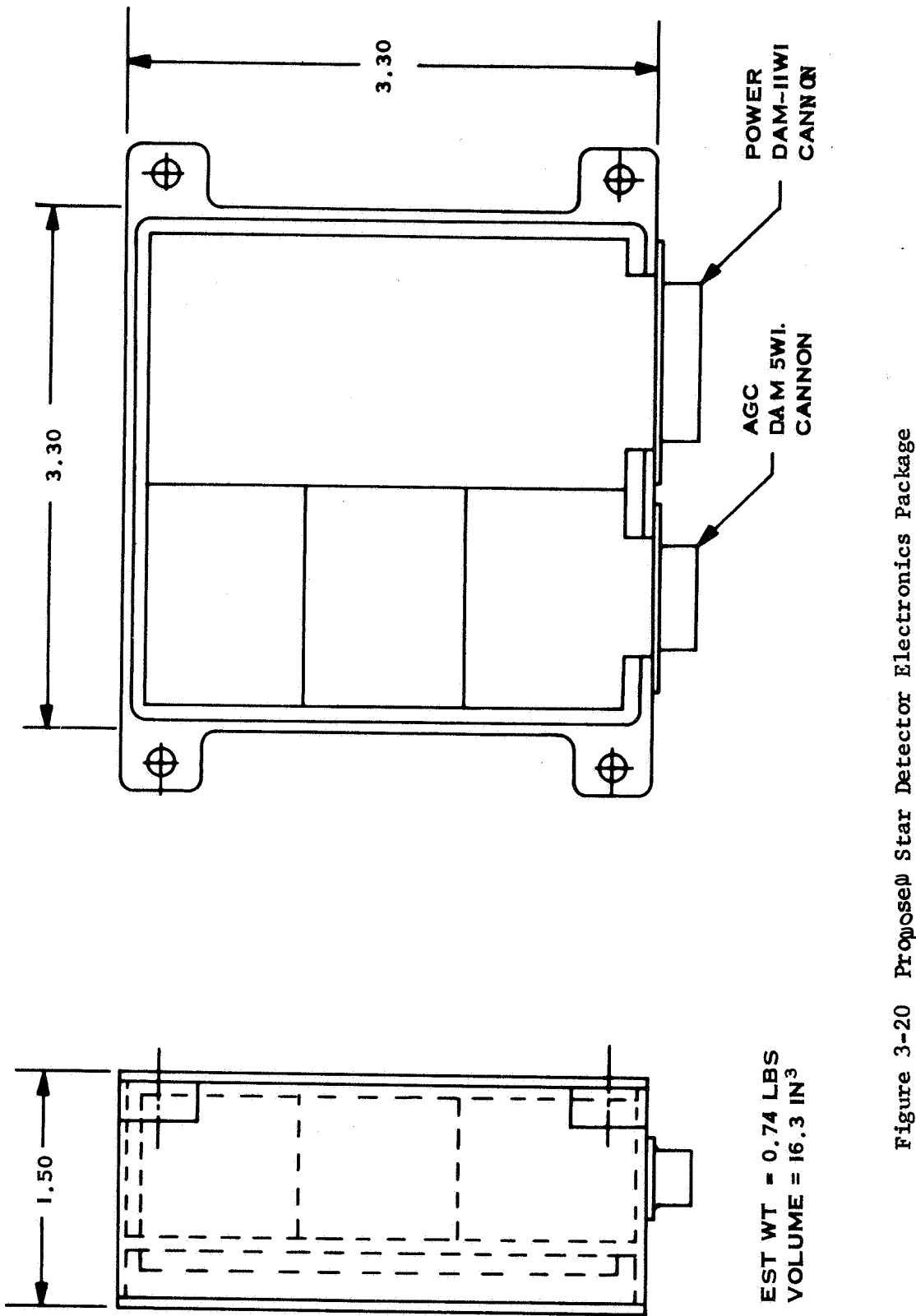


Figure 3-20 Proposed Star Detector Electronics Package

3.2.3 Calibration Testing

As noted above, calibration of the NavSat star detector to the vehicle axis is not highly critical. However, the internal accuracy of the unit itself is important, and must be known if precise star positions are to be measured. Slight variations in focal length, which are unavoidable in lens production, will have the effect of displacing star images on the reticle at different physical distances from the optical axis. The difference between the assumed and the effective focal length would appear as an error in the measurement of angles. Thus, the effective focal length of a given star detector must be calibrated before star image transit times across the angles reticle openings can be used with precision for measuring the angle between a star and the optical axis of the detector.

A specially designed star collimator and holding fixture will be used for calibrating and testing the star detector. A schematic of the test system is shown in Figure 3-21.

The star detector is mounted in the test fixture and is aligned to the star collimator, with the optical axes of both instruments coincident. This alignment will be done visually, with the photomultiplier tube withdrawn from the detector, by observing the target star image in the central fiducial mark on the reticle. The photomultiplier will then be replaced.

As shown in Figure 3-21, the test fixture holding the star detector is capable of being tilted at the intersection of the optical axis with the mirror, to place the star image at positions up to $\pm 2.5^\circ$ off the telescope axis in a plane passing through the vertical openings in the reticle. The lever arm tilting the star detector will be about 40 inches long. If the movement of the arm relative to the base is known to .0002 inch, the angle through which the star detector is moved will be known to 1 arc second. However, since the target star is seen by the detector through a mirror, the optical angle becomes doubled, and tilt will be determined to 2 arc seconds. The test fixture is an adaption of the sine bar principle, where repeatable measurements to this accuracy or better are readily attainable with toolroom gauging techniques.

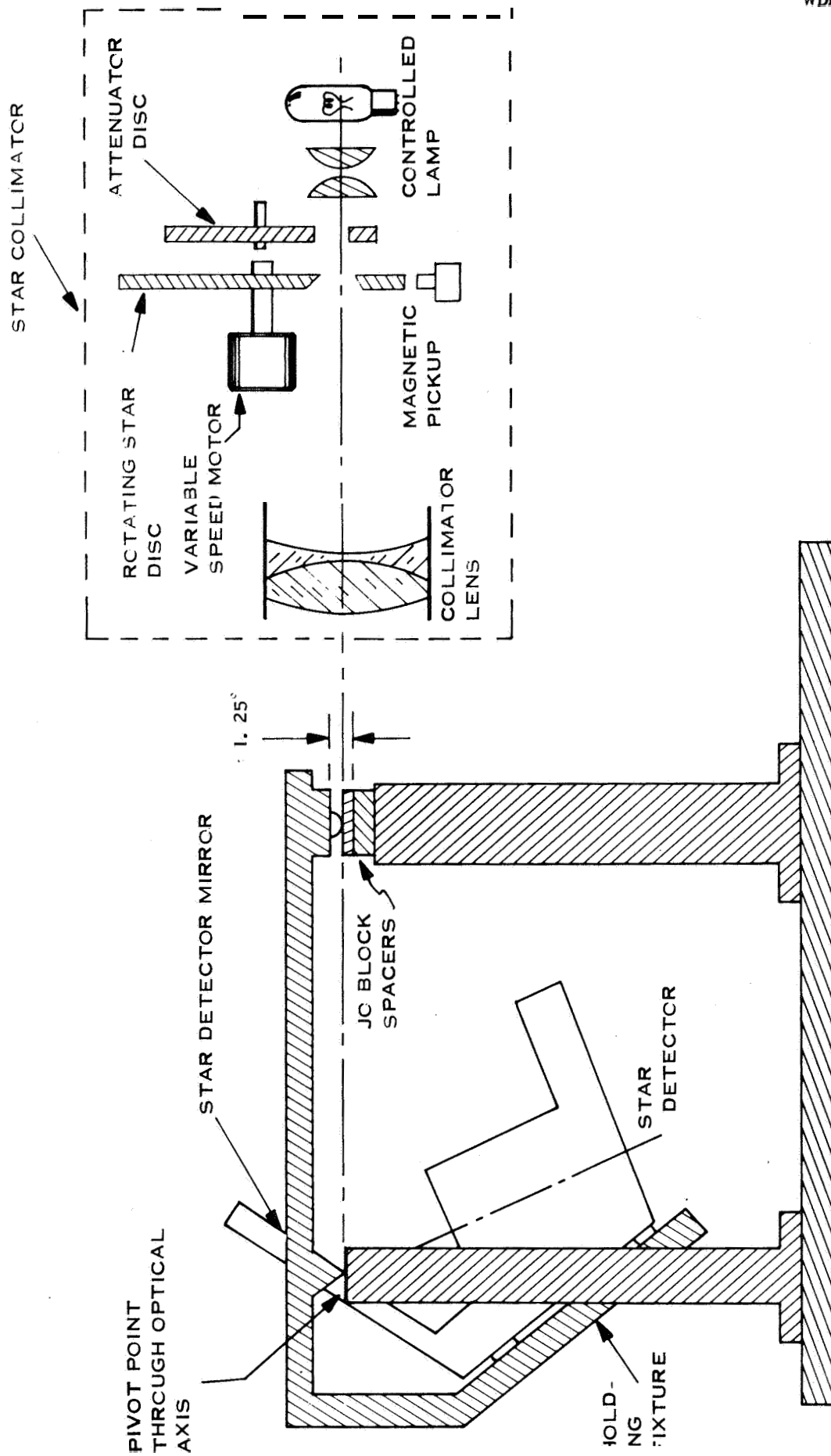


Figure 3-21 Star Detector Calibration and Checkout Equipment

The artificial star in the collimator will be mounted on a rotating disc, the star being stopped on the collimator axis for the measurement described above. If the disc is now rotated, the star will cross the focal plane in the collimator and its image will sweep across the reticle openings, generating pulse trains through the detection system.

The electronic output from the Star Detector may be reduced to angles representing the actual positions of the star image as it crosses the reticle openings, relative to the Star Detector optical axis. Comparison of these data obtained at various field angles, with the true angles derived from the **known** speeds of disc rotation and field angles of the star, will establish the effective focal length of the telescope and serve to calibrate any discrepancies in the optical system due to optical distortion and reticle inaccuracies.

As the rotating star follows a radial rather than a horizontal path, a simple correction factor will be applied. The collimator lens will be selected for a flat field, low distortion and other optical characteristics suitable for this application.

Disc rotation will be detected by a magnetic pickup, and can be monitored on an oscilloscope and timed to 0.10 percent with a Dymec counter.

3.2.4 Installation Checkout

The star detector will be mounted on the satellite with the protective cap in position, to prevent the entry of light and dust. A miniature tungsten light, mounted on the inside of the expendable cap, will be used to confirm operation of the photomultiplier tube, and at a higher intensity, operation of the automatic sun shutter and the remote opening control,

WEIGHT: The maximum weight of the NavSat Star Detector **is** estimated to be:

| <u>Item</u> | <u>Weight (lbs.)</u> |
|--|--------------------------|
| Photomultiplier Tube | 0.30 |
| PMT Shield | 0.42 |
| Power Supply | 0.37 |
| Electronic Package | 0.74 |
| Expendable Cap | 0.20 |
| Sun Shutter | 0.30 |
| Beryllium Mirror | 0.40 |
| Hexcell Baseplate & Pads | 0.30 |
| Fasteners & Hardware | 0.30 |
| Housing for Lens, Mirror PMT; Cap Plate & Baffles | 3.70 |
| Lens & Integral Mount | 1.65 |
| | <u>8.68</u> |

DIMENSIONS: Maximum dimensions **of** the unit will be approximately:

| | |
|--------|-----------|
| Length | 10.25 in. |
| Width | 4.25 in. |
| Height | 7.0 in. |

(**Less** mounting plate and covers)

The electronics package will be:

| | |
|--------|---------|
| Length | 3.3 in. |
| Width | 3.3 in. |
| Height | 1.5 in. |

The total volume of the unit and its electronics will be in the order of 108 in³ ■

POWER: The simple **AGC** scheme, as proposed, will draw no power when commanded "off", after the "off" command passes by. When "on," the experiment will draw **12** watts from the **-24** v bus.

Should a solid-state manual gain control scheme be adopted, it would add about 100 mw to the total, while **an** all-relay scheme would add no significant steady-state power drain. This is not presently planned.

The solenoid operating the sun shutter will require 1.5 watts for 100 msec on automatic closure, and the **same** when opening on command ■

3.3 NUTATION DAMPER INTEGRATION

In order to achieve the spin-axis stability required for the navigation experiment it is necessary to have some form of nutation damping. The levels of allowable spin-axis motions desired are on the order of 0.1 mr or less. To attain this level of accuracy a passive circular constraint mercury nutation damper has been selected. This device has been analyzed and tested (1); while relatively simple in design, it provides the required damping torques.

The version of the circular constraint damper to be used is one in which the damper rod restraint is replaced by a circular brace, and a heavy fluid such as mercury is used as the damper mass (see Figure 3-22). With the damper mass free to flow in the race, the fluid spreads out uniformly at the end of the damping period, and the symmetry axis of the spinning vehicle exhibits no spin-wobble. Alternately stated, the fluid acts as an asymmetric damper mass during nutation and as a circularly symmetric mass during spin of the vehicle.

The simplified equation of motions for the damper are given as follows:

(Ref. 1)

$$\dot{\gamma} = \frac{m p h}{I_T} \left(\frac{I_P}{I_T} \Omega_s \right) \sin \alpha \quad (1)$$

$$\ddot{\alpha} + \frac{C_f}{m} \dot{\alpha} + \frac{h}{\rho} \left(\frac{I_P}{I_T} \Omega_s \right)^2 \gamma \sin \alpha = -\frac{C_f}{m} \left(\frac{I_P - I_T}{I_T} \right) \Omega_s \quad (2)$$

where

I_P and I_T are the polar and transverse mass moments of inertia

Ω_s = spin rate

h , p and m are as shown on next page

-
- (1) W. F. Cartwright, E. C. Massingill, R. D. Trueblood,
"Circular Constraint Nutation Damper," AIAA Journal
Vol. I, No. 6, June 1962.

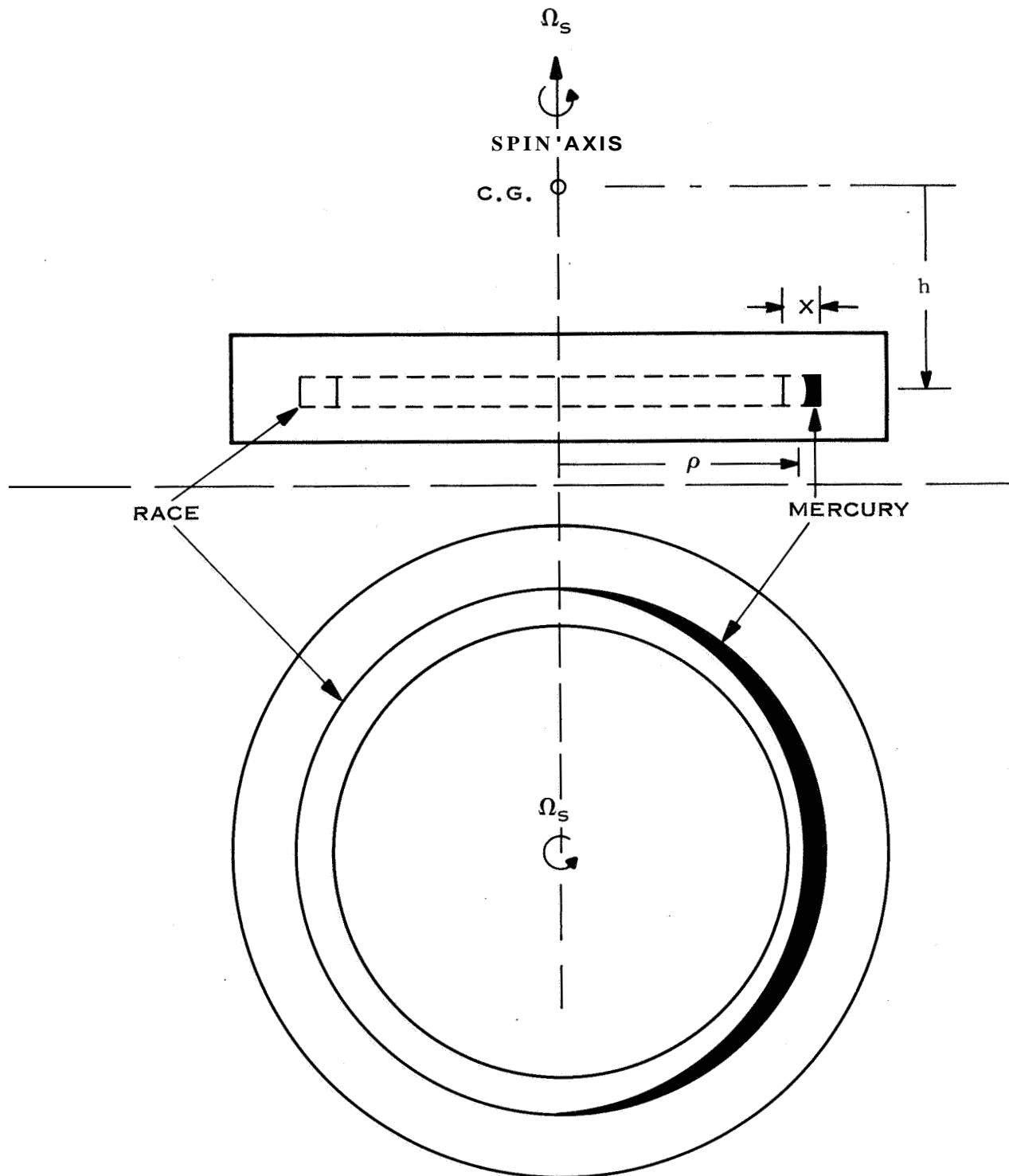
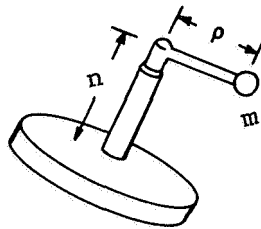


Figure 3-22 Schematic of a Nutation Damper



The frictional force on the damper is approximated by the product of a constant C_f and the relative velocity.

γ = angle between the spin axis and angular momentum vector H .

α = angle between the damper rod and transverse angular velocity vector.

The nonlinear equations (1) and (2) may be made integrable if $\dot{\alpha} \approx 0$ (damper mass rotates very nearly at the nutation rate) in which case the following expressions result:

$$\gamma^* = C_f \left(\frac{\rho}{hm} \right) \frac{1}{\Omega s} [r (1-r)] \quad (3)$$

$$t^* = \frac{\gamma_o^2 - \gamma^{*2}}{C_f \rho^2} \left[\frac{r}{1-r} \right] \frac{I_p}{2} \quad (4)$$

where:

t^* is the transition time from nutation-synchronous to spin-synchronous damping. (Time constant for nonlinear region of damping).

γ^* is the nutation half cone angle at the time of transition (t^*)

Figure 3-23 shows the curves of damping time history for the nonlinear range of damping covered by equations (3) and (4) for several damper masses.

Following are some damper design conditions and assumptions together with a table of parameter damper design values.

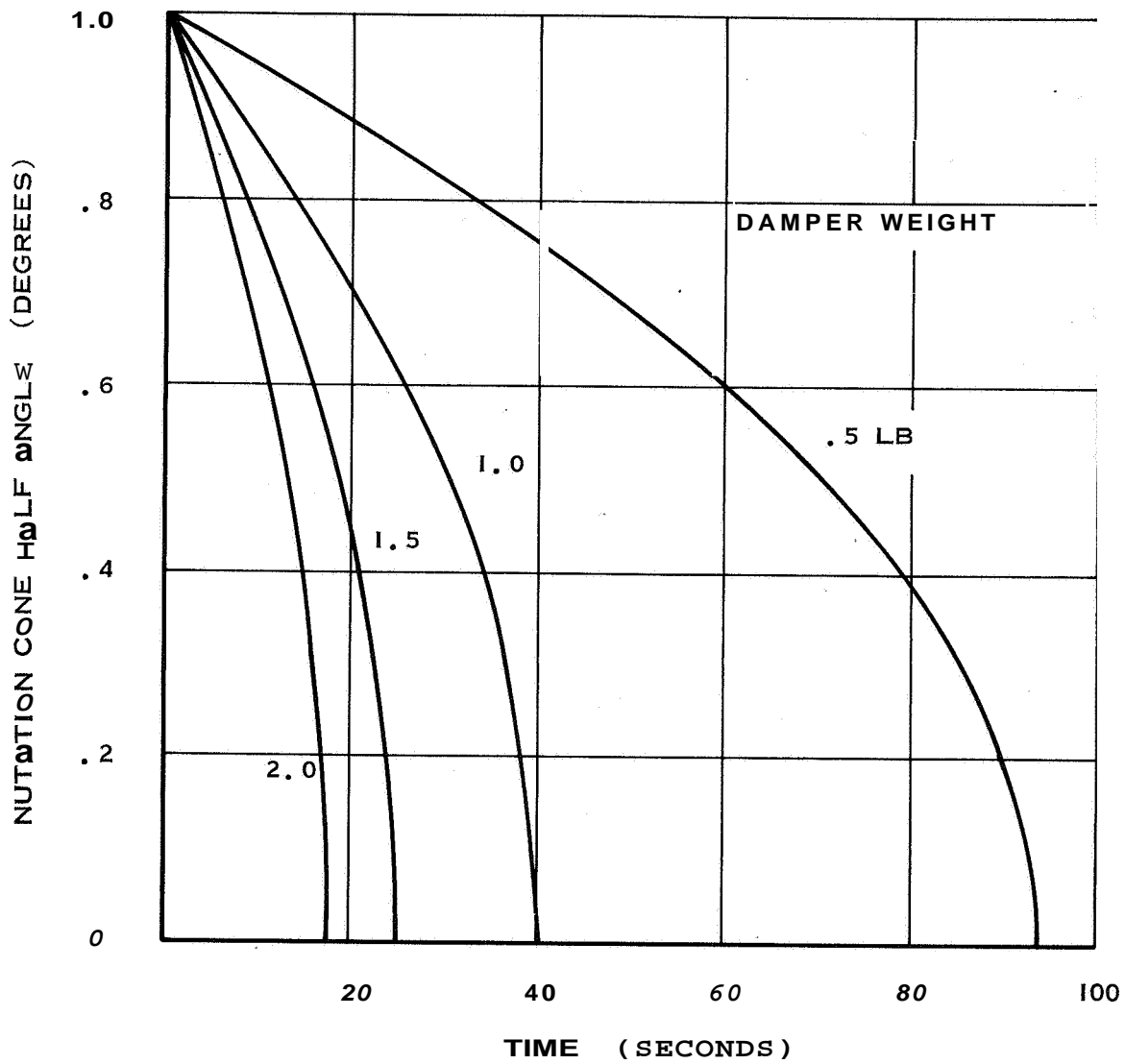


Figure 3-23 Damping Time History $\nu^* = 20$ Seconds of Arc

- a. **Design Conditions** (as furnished by B. D. Trueblood, General Motors Defense Research Laboratories, Santa Barbara, California)

$$I_P = 3.0 \text{ slug-ft}^2$$

$$\Omega_s = 2 \text{ rps}$$

$$\gamma^* = 20 \text{ seconds of arc}$$

$$\lambda = 1.10$$

- b. **Damper Assumptions**

Circular constraint, 1 channel

Mercury, 50 percent fill

Square cross-section race

$$.1 \leq mg \leq 2 \text{ lbs.}$$

$$h = 20.4 \text{ inches}$$

- c. **Table of Parametric Values**

| P (inches) | X (inches) | mg* (lbs.) | C _f (slugs/sec) | t* (sec.) |
|---------------|---------------|---------------|-------------------------------|--------------|
| 1.45 | .210 | .1 | .00061 | 763.5 |
| 2.36 | .375 | .5 | .00220 | 93.6 |
| 2.76 | .488 | 1.0 | .00350 | 40.1 |
| 3.00 | .565 | 1.5 | .00460 | 24.6 |
| 3.20 | .638 | 2.0 | .00560 | 17.3 |

* Does not include weight of race and housing.

Satellite Integration, The nutation damper selected for use in the proposed configuration is estimated to weigh 1.5 pounds including mercury and housing. The damper has been mounted as far away from the center of gravity as possible on the spin axis. Figure 3-8 shows the proposed location of the nutation damper immediately below the 400 MHz telemetry antenna. The damper-antenna assembly is also easily removable for purposes of tanking the spin-up gas storage system before launch.

3.4 ELECTRICAL SYSTEM DESIGN

3.4.1 Introduction

Configuration studies for the design of the electrical system of the experimental Navigation Satellite have one main objective: identification of the best system design which will provide the required performance with the expenditure of the least amount of time and money. Accordingly, a design **has** been selected which **makes maximum** use of the communications satellite developed by Philco WDL for the Department of Defense under Air Force **contract**. Not only is the basic satellite **structure** utilized, but the individual subsystems and components are retained wherever possible. The soundness of this approach **is** substantiated when the economic factors of reliability, cost, and availability are evaluated.

A recommended design has been developed in sufficient detail to enable a confident evaluation of its feasibility. Almost without exception, components have been selected which have been used (~~or~~ qualified for use) on other satellite programs.

3.4.2 Design Requirements and Constraints

3.4.2.1 Design Requirements

The electrical system configuration was developed to meet certain requirements imposed by the objectives of the Fan Beam Navigation System Experiment. These requirements include the following:

- a. Reliable operation for at least one year in an elliptical orbit.
- b. Generation of sufficient RF power to obtain the desired navigation accuracy with a variety of users.
- c. Capability of accepting commands in order that various experiments can be performed over different portions of the orbit,
- d. Transmission of telemetry data to allow monitoring of critical vehicle parameters in order that system performance can be accurately evaluated ■

- e. ~~Compatibility~~ with ground stations of the **NASA STADAN** network in selection of carrier frequencies and modulation methods.
- f. Continuous transmission ~~of~~ data signals which allow the satellite to be tracked to any point in its orbit.
- g. **No** reference channel **is** required other than that ~~provided~~ by direct transmission of star detector data.

In addition to these requirements, the obvious constraints ~~of~~ low weight and small size apply to all subsystems. Structural and thermal considerations also impose constraints ~~of~~ rigidity and passive temperature control. Reliable operation within the capability of the existing solar array demand that highly efficient DC/DC converters be used to regulate the power to each of the components, and hermetically-sealed nickel-cadmium batteries be used to provide ample power for reliable performance of the experiments throughout the full lifetime of the mission.

Table 3-2, Equipment List, gives the size, weight and power consumption for the satellite components.

Table 3-2 Equipment List

| | Equipment | Size (inches) | Weight (lbs.) | Power (watts) |
|-----|---|--|---------------|--------------------|
| 1. | Structure | 37.0" dia x 32.0 H. | 21.32 | ---- |
| 2. | Solar Array | 8 3/4 x 13 5/8 (Rect. 8) 5 1/4 x 13 1/2 x 15.4 (Trap. 16) | 22.87 | ---- |
| 3. | Battery (2 ea.) | ----- | 8.00 | ---- |
| 4. | Harness and Connectors | ----- | 8.00 | ---- |
| 5. | Waveguide Antennas (4 ea.) | 60.0" x 2.5 x 1.25" | 4.00 ea. | ---- |
| 6. | Antenna Switch # 1 | 3.0 x 2.0 x 3.0 | 1.50 | 13.5 watts/50 msec |
| 7. | Antenna Switch # 2 | 3.32 x 3.32 x 6.25 | 1.50 | 13.5 watts/50 msec |
| 8. | Waveguide | ----- | 6.00 | ---- |
| 9. | Command Antenna | ----- | 1.00 | ---- |
| 10. | TWTA (ea.) (x2) | 7.87 x 4.4 x 2.53 | 3.35 ea | 25.00 ea. |
| 11. | Frequency Generator | 9.50 x 5.0 x 1.2 | 2.05 | ---- |
| 12. | Exciter | 10.0 x 4.0 x 1.3 | 1.85 | ---- |
| 13. | Communications DC/DC Conv. | 7 x 4 x 1.6 | 1.91 | 8.80 |
| 14. | TLM Transmitter (ea.) (x2) | 9.4 x 3.5 x 1.2 | 1.04 | ---- |
| 15. | TLM Coax Switch | 2.16 x 1.19 x 2.19 | 0.32 | 52 watts/25 sec |
| 16. | TLM Generator | 8.9 x 6.5 x 2.5 | 3.61 | ---- |
| 17. | TLM DC/DC Converter (x2) | 7.0 x 4.1 x 1.6 | 1.73 | 4.75 |
| 18. | Command Receiver | 3.5 x 5.0 x 1.2 | 1.00 | ---- |
| 19. | Command Decoder | 3.5 x 5.0 x 1.5 | 1.50 | ---- |
| 20. | Command Controller | 3.0 x 4.0 x 2.0 | 2.00 | ---- |
| 21. | Command DC/DC Converter | 3.0 x 3.0 x 2.0 | 1.50 | 4.25 |
| 22. | Charge Control | 5 x 6.0 x 4.0 | 3.50 | 3.00 |
| 23. | TWTA Control | 5.0 x 6.0 x 3.0 | 3.00 | 2.00 |
| 24. | Power Control Unit | 5.25 x 6.28 x 3.03 | 3.14 | 3.05 |
| 25. | Vehicle Timer | 3.0 x 3.0 x 3.0 | 1.50 | 1.50 |
| 26. | Star Detector | 18 x 10 x 12 | 8.0 | 1.30 |
| 27. | TLM Antenna | 6.0" dia. x 1.2" H. | 0.68 | ---- |
| 28. | RF Power Amplifier (for Star Detector) | 4 x 7.0 x 2.0 | 1.25 | 10.00 |

The primary operational mode consists of radiating **RF** power at a frequency of approximately 8 **GHz** from a pair of fan beam slotted-waveguide antennas mounted on a satellite spinning at 100 rpm, (These antennas are described in Section 3.1). Simultaneous with generation of the fan beams, star-detector data is also transmitter over a separate radio link to the user. Different fan beam antennas can be selected by commands received by the on-board command subsystem. The Telemetry Subsystem transmits to the user critical vehicle and subsystem parameters, such as temperatures, voltages, currents, and pressures, in order that the condition of the satellite can be determined. Commands can be accepted which will allow certain components to be turned on or off, and allow the batteries to be properly charged for maximum capacity and long life. Achievement of the basic goal of the fan beam experiment is made more certain by incorporating provisions for switching either traveling-wave-tube amplifier to either set of fan beam antennas. Thus, in the event of a failure of one TWTA (a highly unlikely occurrence, based on life-test and reliability data), the other TWTA could still be used for either experiment,

The satellite could be launched into an elliptical orbit from Cape Kennedy by use of an Atlas-Agena or Titan III-C launch vehicle. The inclination of the orbit is such that it will be in view of STADAN tracking stations in the Southern Hemisphere for the greater portion of its time in orbit,

Following the ascent phase of the mission and during insertion into orbit, the shroud is ejected from around the satellite. Solar energy illuminates the solar array and the Telemetry Subsystem goes into operation. At the time of separation of the Navigation Satellite from the launch vehicle trans-stage, an electrical signal is sent to the event timer. Ten seconds later, the event timer causes squibs to be fired which allow the fan beam antennas to be deployed. Following this deployment, the timer causes a second set of squibs to be fired which actuate valves on the spin bottles and the satellite is spun up to its in-orbit rate of approximately 100 rpm.

Computer-generated orbital elements, based on launch and ascent trajectory parameters, allow an appropriate ground tracking station of the **STADAN** net to acquire the 400-MHz telemetry transmitter carrier. Once lock-on of the carrier is achieved, telemetry data is read out and the status of the vehicle and all its subsystems is determined. Depending on the time-in-view of the satellite at the particular ground station being used, a series of **commands** can now be transmitted to exercise the **command** subsystem and ensure that all command functions are operational.

Once a stable orbit has been achieved and the orbital elements are known to a high degree of precision, the actual fan beam experiments can be performed. The fan-beam transmission subsystem is energized and the desired **pair** of antennas (Nos. 1 and 2, or Nos. 3 and 4) selected by means of appropriate commands transmitted from the user ground station. To conserve power and to provide for transmission of telemetry and star sensor data free from excessive errors, only one subsystem is energized at a time. A low-loss coaxial switch is used to switch the telemetry antenna from one transmitter to the other. Magnetic latching is used **so** that there is no holding power required in either position. Power is applied only to the DC/DC converters of the subsystem whose transmitter is connected to the antenna by means of interlock circuitry in the command controller. Both telemetry transmitters operate on the same frequency in the 400-MHz telemetry band; the ground antenna tracking and data receivers will require little if any retuning when either telemetry or star sensor data is being transmitted. Since continuous star sensor data is normally desired throughout a fan beam experiment, telemetry data is read out for five or ten minutes at the beginning and at the end of each experiment period. Provisions can be incorporated in the final design for powering either subsystem from the nickel-cadmium batteries, thus allowing the satellite to be continuously tracked while passing through eclipse and either star sensor or telemetry data to be received. By connecting the telemetry subsystem to the battery bus, a complete temperature history **of** the satellite can be obtained as it passes through eclipse, and valuable thermal data collected.

3.4.3 Basic Electrical System Description

The basic electrical system is shown in the block diagram, Figure 3-24. The individual blocks marked with an asterisk (*) are units developed for the USAF Communications Satellite Program and are used as is, or with minor modifications. For clarity of explanation, the electrical system is divided into several subsystems, consisting of the Power Subsystem, the Fan Beam Transmission Subsystem, the Command Subsystem, the Telemetry Subsystem, and the Star-Detector Subsystem. A brief description of each of these subsystems is given here; the individual boxes are more fully described in the following sections.

3.4.3.1 Power Subsystem

The Power Subsystem consists of the basic satellite solar cell array, a nickel-cadmium battery, and associated power control and battery charge control circuitry. The solar array is used to charge the battery and also provides power to the Command and Telemetry Subsystems and the low-level portion of the Fan Beam Transmission System. An alternative method considered during the early stages of the design is to use the solar array exclusively for charging the batteries, and power the entire satellite from the batteries. The present design was chosen in the interests of flexibility in switching units on and off with freedom from transients getting into the more critical circuits. Provisions are also incorporated for operation of the Telemetry or Star Detector Subsystems from the solar array should the battery fail.

The basic solar array consists of 8 rectangular panels and 16 trapezoidal panels. Each rectangular panel contains four 76-cell, series-connected strings, wired in parallel. Each trapezoidal panel contains four 84-cell series connected strings, wired in parallel. The total array consists of 7,808 NP silicon solar cells, which are rated at 10 percent conversion efficiency at 28°C and at air-mass zero. Cover glass slides are bonded to the solar cell surfaces with a transparent adhesive. These slides

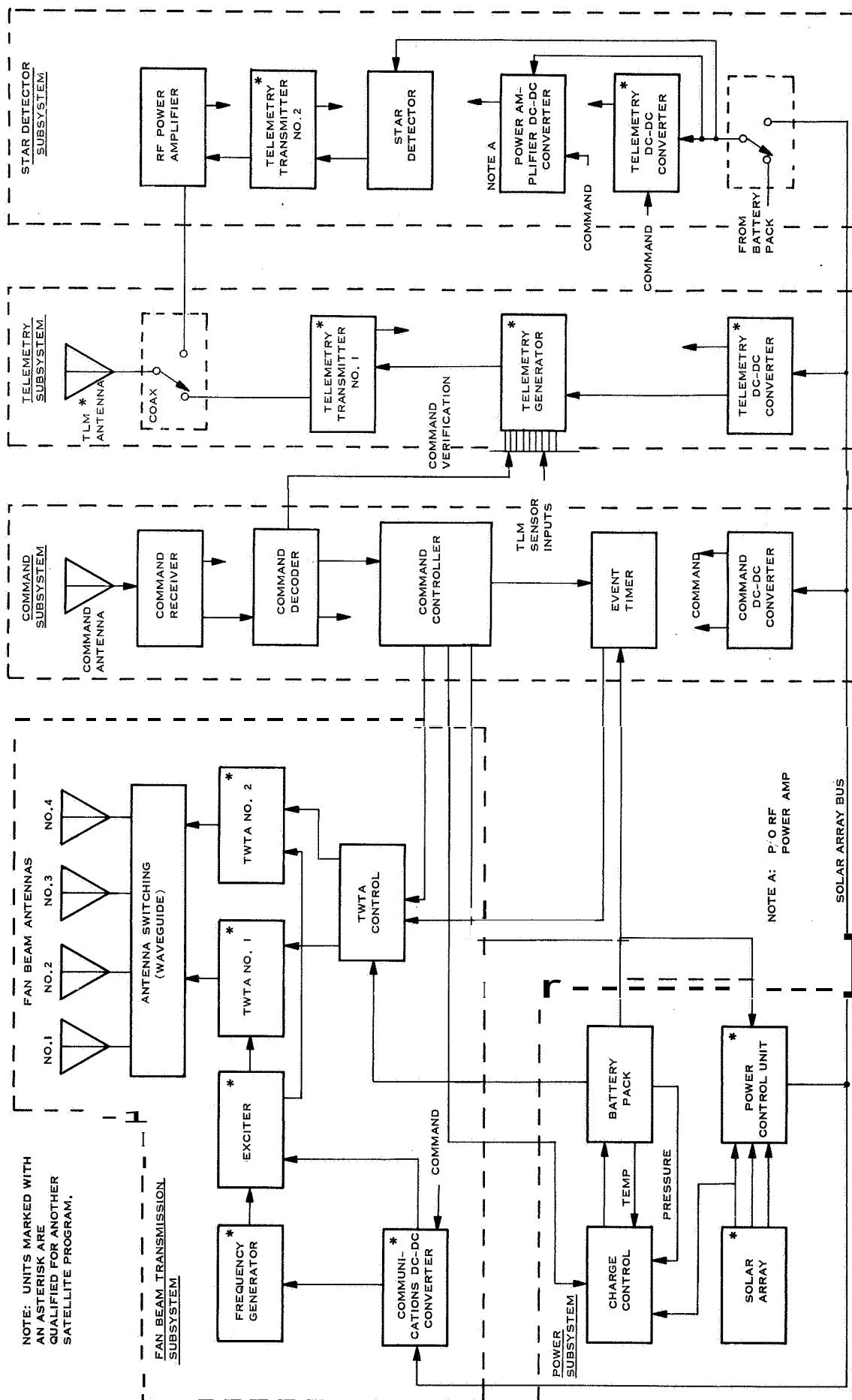


Figure 3-24 Basic Electrical System Block Diagram

provide space environmental particle radiation protection, increase the cell's spectral radiation resistance, and offer protection against micro-meteoroids. The power output of this array *is* approximately **42** watts initially, and decreases to 36 watts at the end of one year in orbit due to effects of the space environment.

The battery consists *of* 23 hermetically sealed nickel-cadmium cells packaged into two units because of weight and balance problems. This battery is similar in design and configuration to those used on the **ATS**, **0A0** and **0G0** satellites and should provide good performance throughout the orbital life *of* the satellite. Based on the available power from the solar array and the power required from the battery, 6 ampere-hour cells *were* selected to provide an optimum balance between size-weight-capacity and charge-discharge cycling requirements.

The cells are housed in lightweight, yet strong, boxes *of* aluminum which restrain the cells to prevent excessive expansion due to a build-up of internal pressure during charging. A powdered-metal-filled epoxy cement in the lower portion of each battery box serves to bond the cells to the heat-sink base for good thermal conductivity. This is an important factor in the design of the battery, as both efficiency and long life are directly dependent on adequate control of battery temperature,

The power control unit was designed as an optimum match for the characteristics of the solar array. This unit serves to limit the main bus voltage to 30.0 ± 0.2 volts **DC** under various combinations of solar illumination and power loads. In addition, sequential load switching is accomplished when the satellite is going into or **coming out** of **an** eclipse, preventing cycling on and off of the loads. Voltage and current monitors are **also** provided, to allow measurement of critical array voltages and currents by means of the Telemetry Subsystem. Minor modifications may be required to the power control unit when **used** in the Navigation Satellite.

The battery charge controller is used to ensure that the battery is maintained in the best possible condition throughout its orbital life-time. Nickel-cadmium batteries are quite critical in regard to both cell pressure and temperature in relation to state and duration of charge, if long life at full capacity is to be achieved. Provisions are incorporated in the battery charge controller to monitor individual cell voltage and pressure, and over-all battery temperature. These parameters are then used in controlling the charging current going into the battery so that no critical values are exceeded. The charging current can also be adjusted by means of ground-initiated commands processed by the Command Subsystem in the event of an unforeseen failure of some element of the Power Subsystem. A battery cycling routine can also be initiated via the Command Subsystem in the event of loss of capacity due to the "memory" effect; this effect is present when batteries are charged and discharged at a fraction of their rated capacity.

3.4.3.2 Fan Beam Transmission Subsystem

The Fan Beam Subsystem consists of a frequency generator, an exciter, a communications DC/DC converter, two TWTA's, waveguide, waveguide switches, and a TWTA control unit. Photographs of several of these units are shown in Figures 3-25 through 3-28.

The frequency generator and exciter, which are supplied regulated DC power from the DC/DC converter, consist of a highly stable crystal oscillator followed by frequency multipliers and a power amplifier, which drives a series of varactor diode frequency multipliers. Both units are solid-state, using devices which have been proven in previous satellite equipments. Isolators and filters are used as appropriate to allow drive power free from spurious signals to be delivered to the inputs of the two TWT power amplifiers. Input power to each TWT is at a level of 10 milliwatts at a frequency in the vicinity of 8 GHz.

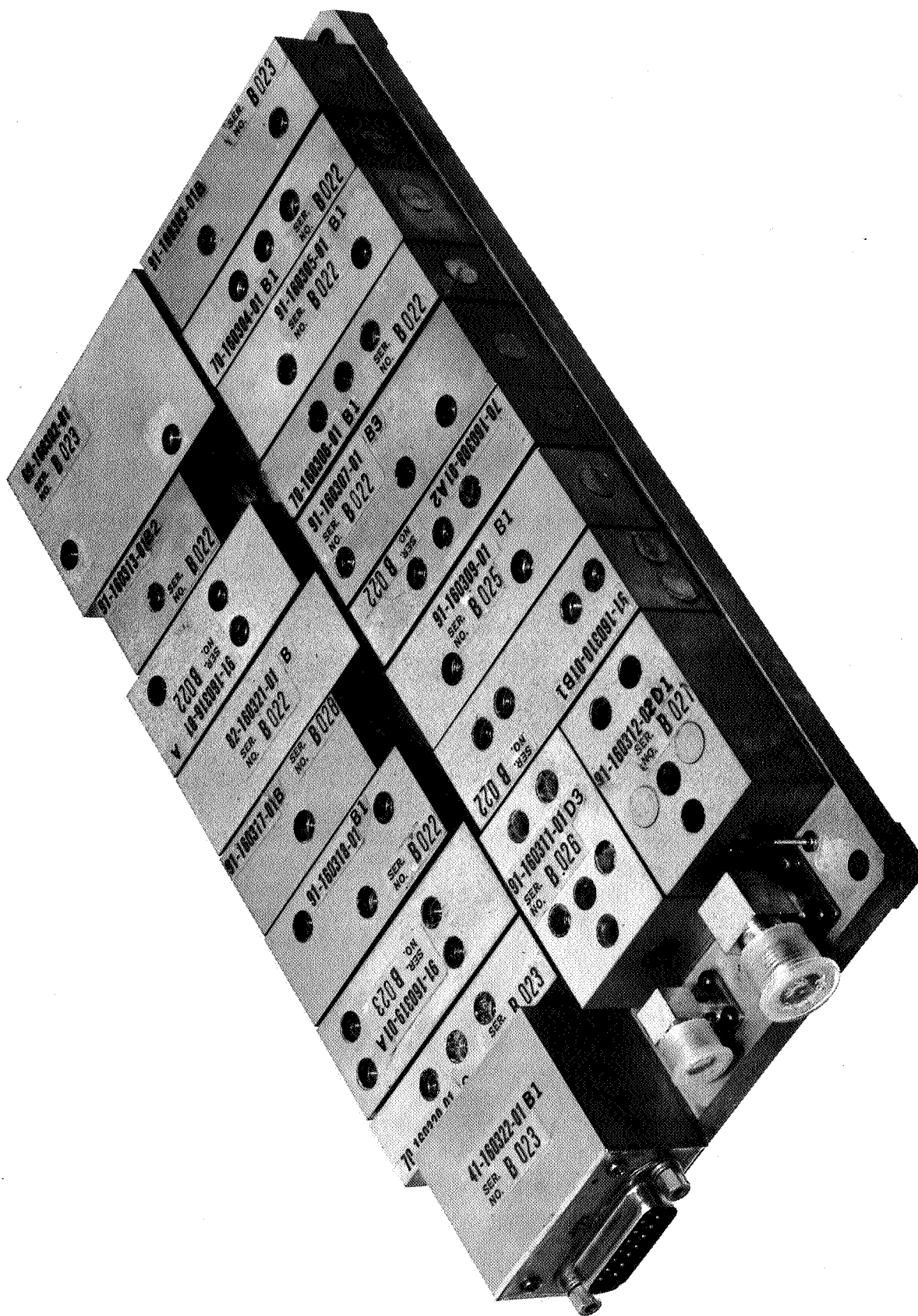


Figure 3-25 Frequency Generator



Figure 3-26 Traveling Wave Tube Amplifier

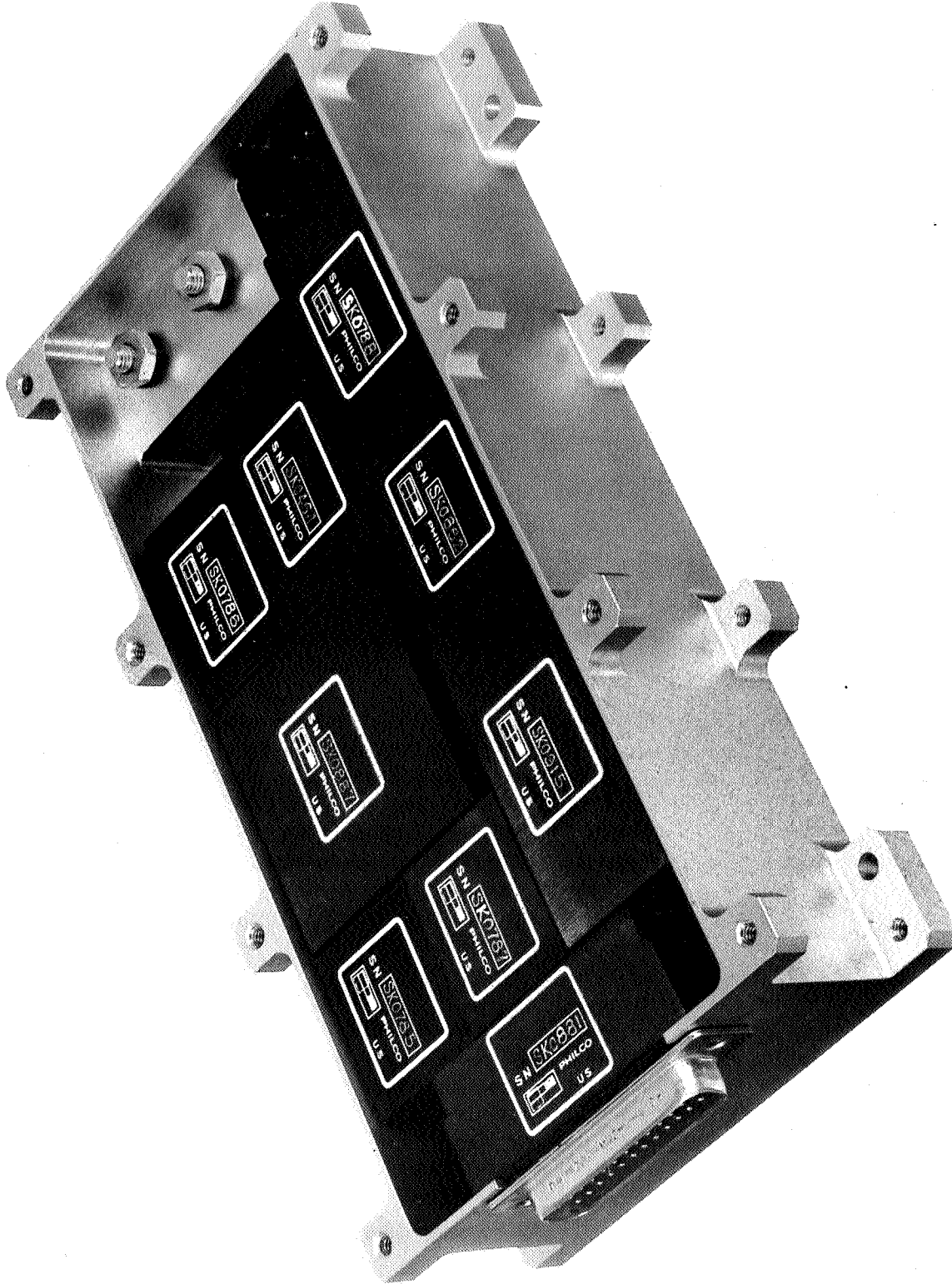


Figure 3-27  DC Converter

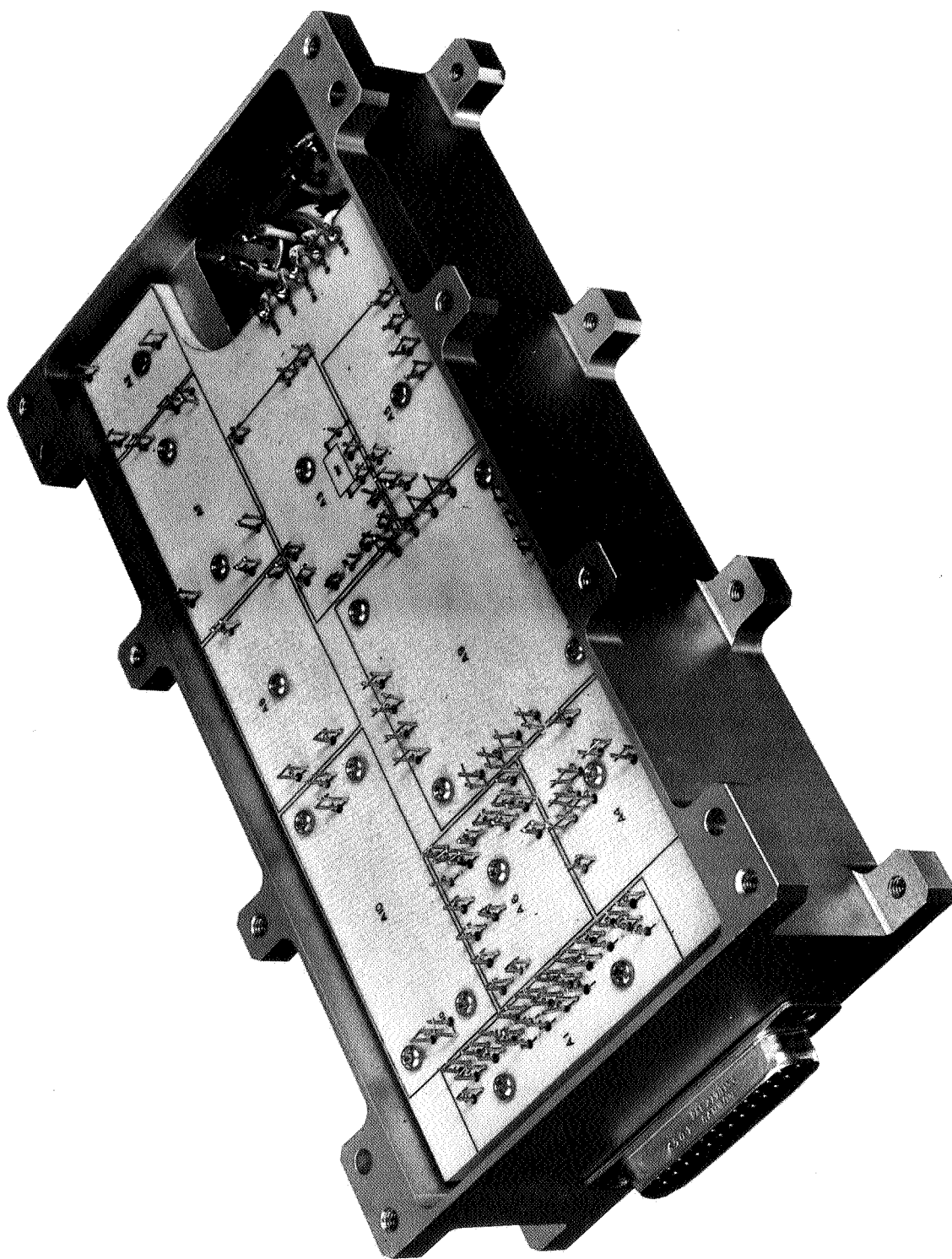


Figure 3-28 DC/DC Converter (Rear View)

The TWT amplifiers proposed for this experiment are almost identical to those used in the USAF Communications Satellite Program, and are under development at the present time. A power output of 6 watts is attained, with a power gain at saturation of at least 41 db. The amplifier contains its own power supply, and the overall DC-to-RF efficiency is 24 percent. Telemetry monitoring circuits are incorporated in the TWTA to provide for measurement of important amplifier operating parameters. The amplifier is completely solid state except for the TWT itself, and is designed to provide long-life, trouble-free operation throughout all phases of the satellite program.

The waveguide switches to be used for this application are units of the type designed for the USAF Communications Satellite Program and have a minimum lifetime of 10,000 switching cycles. The insertion loss is 0.2 db and the isolation between parts is on the order of 50 db. Magnetic latching is used so that no holding power is required.

The TWTA's are turned on and off by means of the TWTA control unit. Binary control signals, initiated by ground command or the vehicle timer, are generated by solid-state circuitry in the control unit. These control signals function to turn the DC/DC converter power supply in the TWTA either on or off. Either TWTA can be energized or de-energized independent of the other. Fail-safe circuitry is used so that the TWTA's are turned off in the event of a malfunction of the control unit.

3.4.3.3 Command Subsystem

The command subsystem utilizes flight-proven components developed for the NASA Scientific Satellite Programs, and is compatible with the STADAN Command System. The units are solid state, highly reliable, and provide for either 21 or 70 commands, depending upon which decoder is finally selected. The receiver receives amplitude-modulated, tone-digital commands transmitted in the 148-150 MHz range, and delivers a PCM audio tone to the decoder. The decoder filters this tone and translates the eight-bit

command words into signals on the output command lines. The command controller uses these signals to control operation of relays **or** solid-state switches, which perform the command functions. Latching-type relays are used in those cases where complete isolation **is** required and no power consumption is desired between commands. A list of typical commands is given in Table 3-3, Command List.

3.4.3.4 Telemetry Subsystem

The telemetry subsystem consists of a telemetry transmitter, a telemetry generator, and a telemetry DC/DC converter. These units were developed for the USAF Communications Satellite Program, are completely solid state, and represent an advanced state-of-the-art development. The pertinent characteristics are shown in Table 3-4.

The transmitter consists of eight welded modules identical (except for slight changes in frequency or power level) to those used in the frequency generator. The ninth module, a harmonic suppression filter, was a new development and causes very little degradation in reliability, since only passive elements are used. The transmitter is phase-modulated by a 1024-Hz carrier and has a power output of 250 milliwatts at a frequency in the 400-401.5 MHz telemetry band.

The telemetry generator accepts both analog and digital inputs and forms them into a data frame comprised of 64 words. Each word is eight bits in length, two bits being used for synchronization and the remaining six for data. Five complete words of each frame are used for frame synchronization, satellite identification, and telemetry calibration. The output of the generator is a serial pulse-code-modulated (PCM) pulse train which differential bi-phase modulates a 1024-Hz subcarrier at a rate of 256 bits per second. One complete data frame requires two seconds for transmission.

The maximum use of monolithic silicon integrated circuitry, in conjunction with the Philco WDL established and proven technique of welded module welded motherboard packaging, has resulted in a design which is advanced and reliable ■

Table 3-3 Command List

| Command Number | Command Function |
|----------------|---|
| 1 | Telemetry Subsystem ON-OFF |
| 2 | Increase Battery Charge Rate |
| 3 | Decrease Battery Charge Rate |
| 4,5 | Star Detector Electronics ON-OFF Star Detector Transmitter ON-OFF |
| 6,7 | Communications Subsystem ON-OFF |
| 8 | Fan Beam Antenna Mode 1 |
| 9 | Fan Beam Antenna Mode 2 |
| 10,11 | TWTA No. 1 ON-OFF |
| 12,13 | TWTA No. 2 ON-OFF |
| 14 | Reset Vehicle Timer |
| 15 | Eject Star Detector Lens Cap |
| 16 | TWTA No. 1/TWTA No. 2 Transfer |
| 17, 18 | Operate Star Detector Sun Shutter ON-OFF (1.5 watts/100 msec) |
| 19 | Star Detector to Solar Array |

Table 3-4 Telemetry Subsystem Characteristics

| Parameter | Requirement |
|-------------------------------|---|
| Data Channels | 74 |
| Analog Channels | 56 |
| Binary Channels | 18 |
| Analog Data Accuracy | 1.5% |
| Data Quantization | 6 bits |
| Bit Coding | PCM differential (NRZ) |
| Bit Rate | 256 bps $\pm 0.05\%$ |
| Word Length | 8 bits |
| Word Synchronization | First 2 bits (11) |
| Frame Rate (Data Sample Rate) | 0.5 frames/sec |
| Frame Synchronization | Zero plus 7 bit Barker (01110010) |
| Frame Length | 512 bits |
| Subcarrier Frequency | 1024 cps $\pm 0.05\%$ |
| Subcarrier Modulation | PSK/PM Biphase |
| Carrier Modulation | PM |
| Carrier Phase Deviation | ± 1 radian peak |
| Carrier Deviation Stability | $\pm 15\%$ |
| Transmitter RF Output Power | 250 Mw minimum |
| Carrier Frequency: | |
| Range | 400 - 401 Mc (selected crystal) |
| Long-Term Stability | $\pm 5 \times 10^{-6}$ for 1.5 years |
| Short-Term Stability | $\pm 1 \times 10^{-8}$ for 1 sec |
| Accuracy | $\pm 1 \times 10^{-5}$ at $+25^{\circ}\text{C}$ |
| Antenna Polarization | Right-hand circular |
| Primary Power | 4.5 watts maximum |
| Duty Cycle | 100% |
| Weight (w/o sensors) | 8.2 pounds |

A block diagram of the Telemetry Generator is **shown** in Figure 3-29.

The telemetry DC/DC converter is very **similar** to the communications DC/DC converter. A block diagram is given in Figure 3-30. The DC/DC converter is used to isolate the telemetry subsystem from electrical transients and noise in the primary power source, to eliminate ground loops, and to provide the specific voltage levels and regulation required for optimum performance and efficiency of the subsystem elements. Current limiting is used in order that a malfunction of the transmitter or generator will not render inoperative the other satellite systems receiving power from the **same** power bus. This converter also provides a very closely regulated +6.2 vdc source for the temperature sensors,

Photographs of telemetry subsystem components are shown in Figures 3-31 through 3-36,

3.4.3.5 Star Detector Subsystem

The Star Detector Subsystem consists of a star detector, a telemetry transmitter, a RF power amplifier, and DC/DC converters to power these units. The star detector, with its associated power supply, is described in Section 3.2. The telemetry transmitter and its associated DC/DC converter are the **same** units as those used in the Telemetry Subsystem. The phase modulator in the transmitter has been slightly modified to accept the video signal from the star detector and develop a low-distortion phase-modulated carrier. This video signal is bandpass filtered to pass from 6 to 15 KHz.

The RF power amplifier is **a** two-stage device using epitaxial silicon planar NPN transistors developed for use at 400 MHz. A single device is rated at **8** watts output at 400 MHz with a collector voltage of 28 volts DC. Two stages are used to develop 4 watts power output with reasonable efficiency, high reliability, and sufficient gain to allow use of the 250-milliwatt telemetry transmitter as a driver.

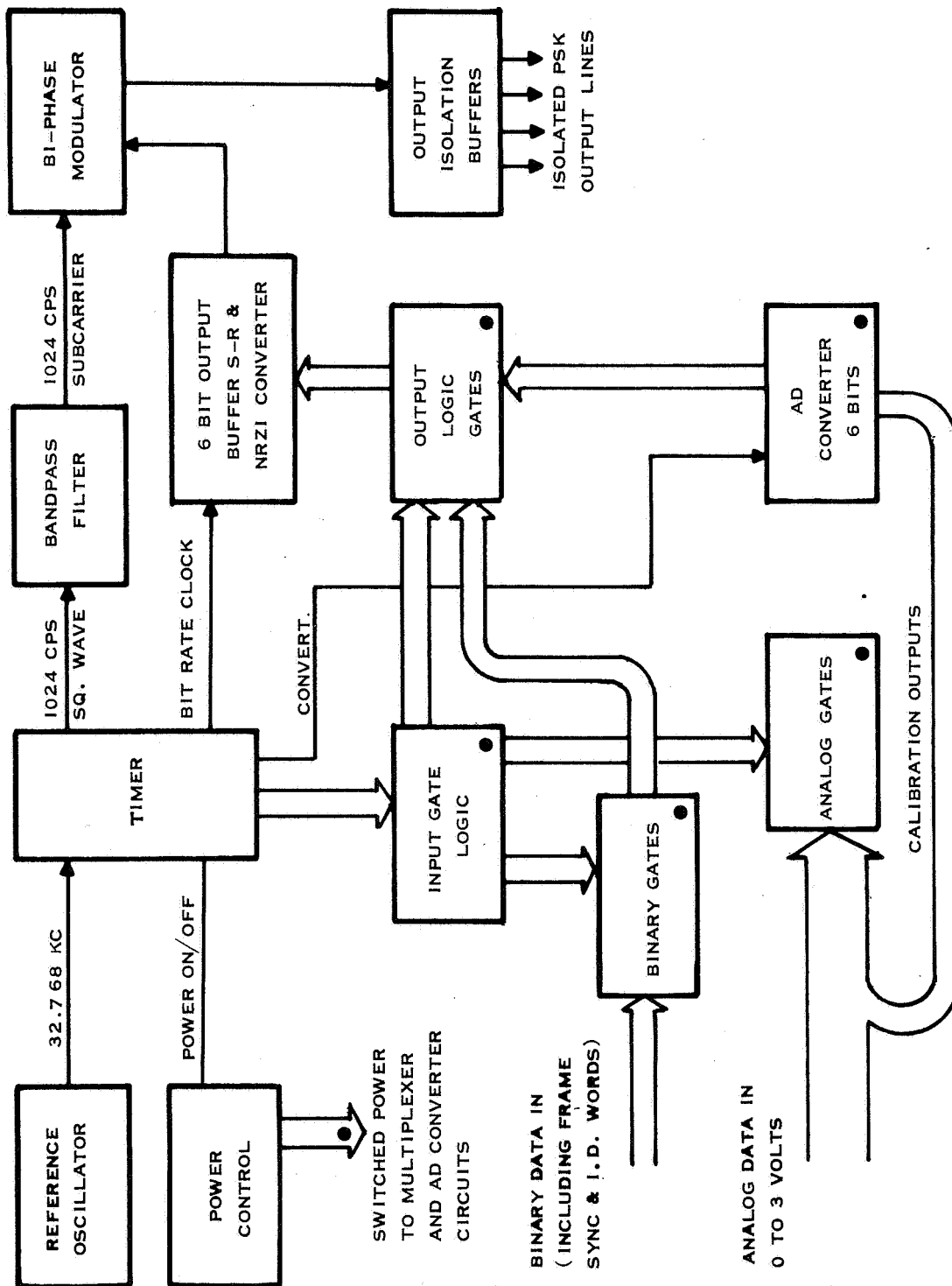


Figure 3-29 Telemetry Generator Block Diagram

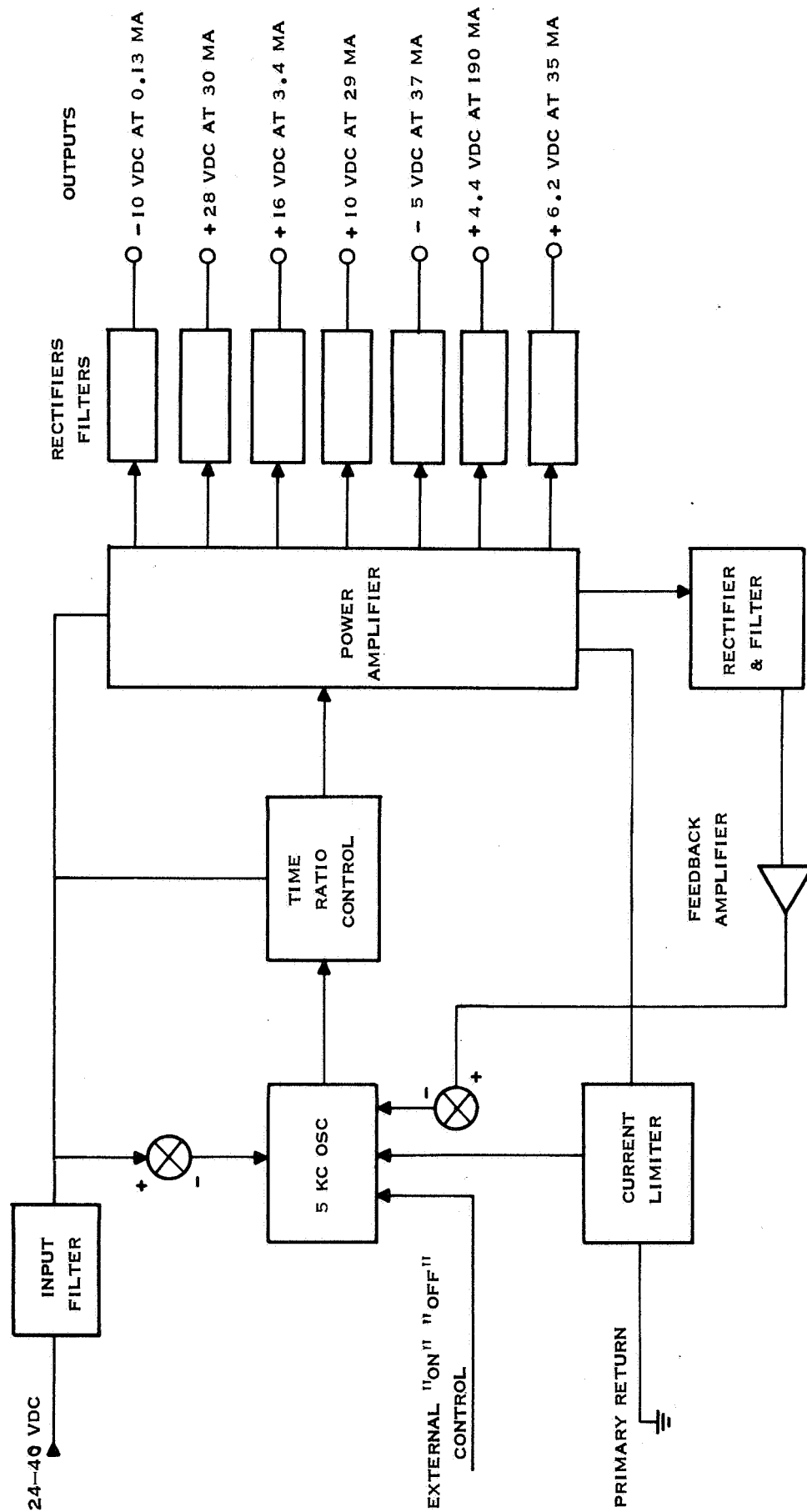


Figure B-30 Telemetry DC/DC Converter

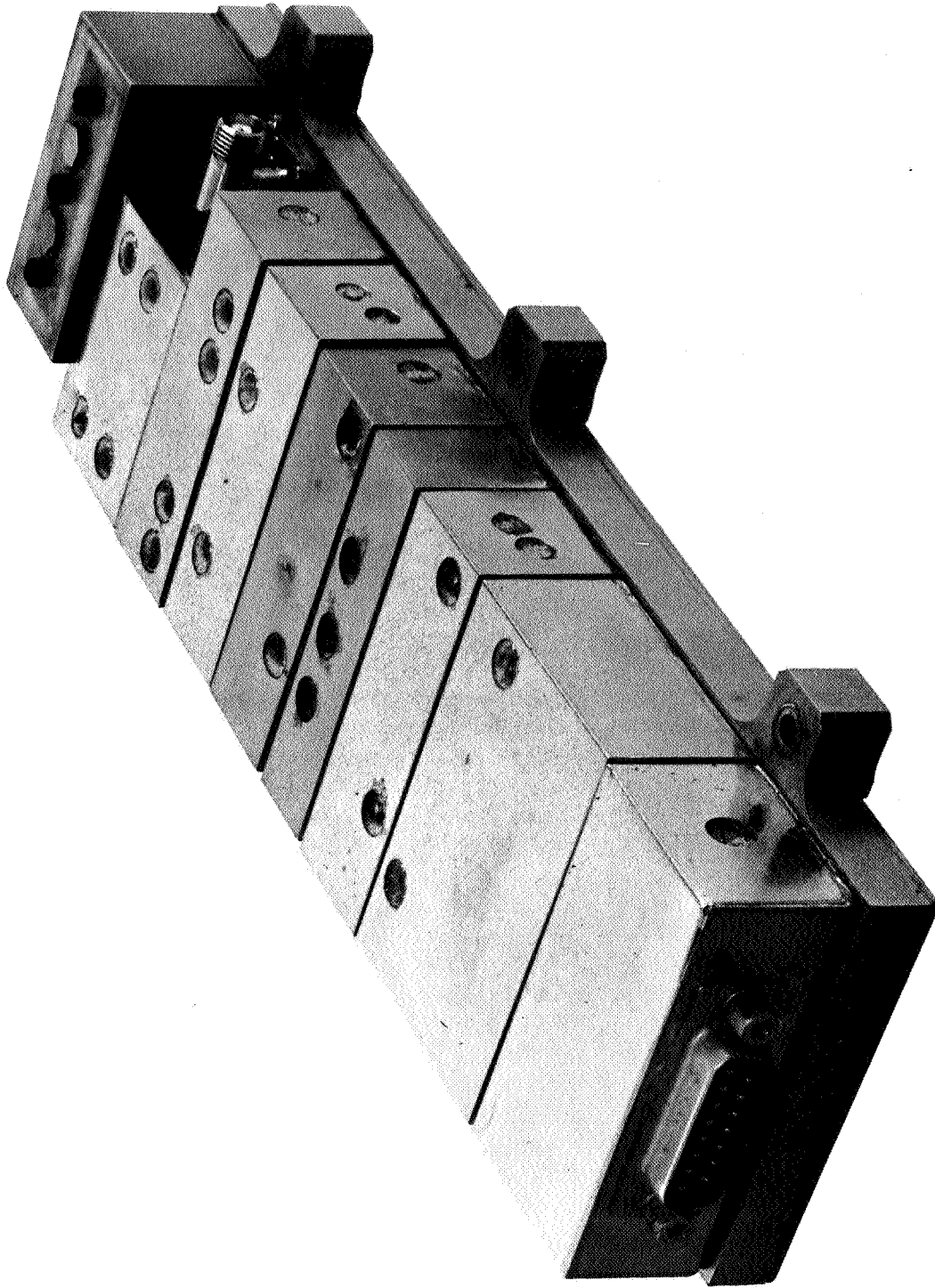


Figure 3-31 Telemetry Transmitter

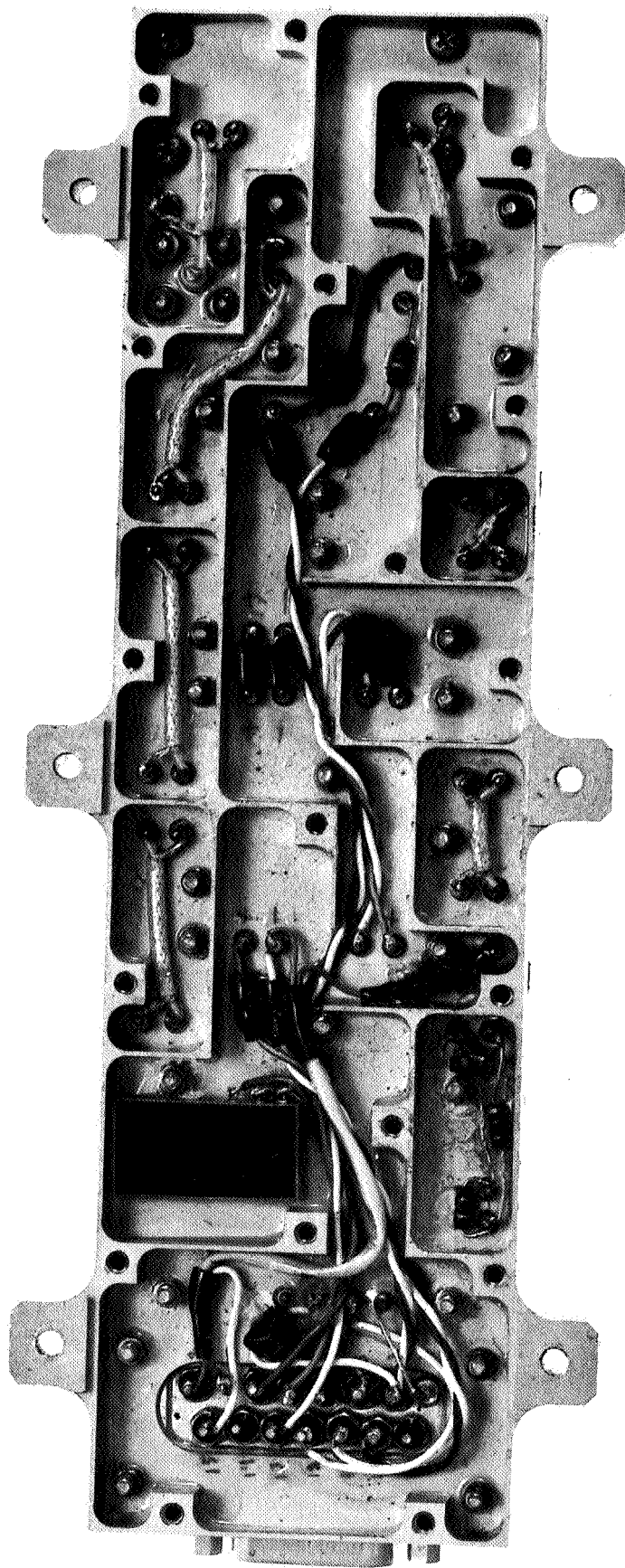


Figure 3-32 Telemetry Transmitter (Rear View)

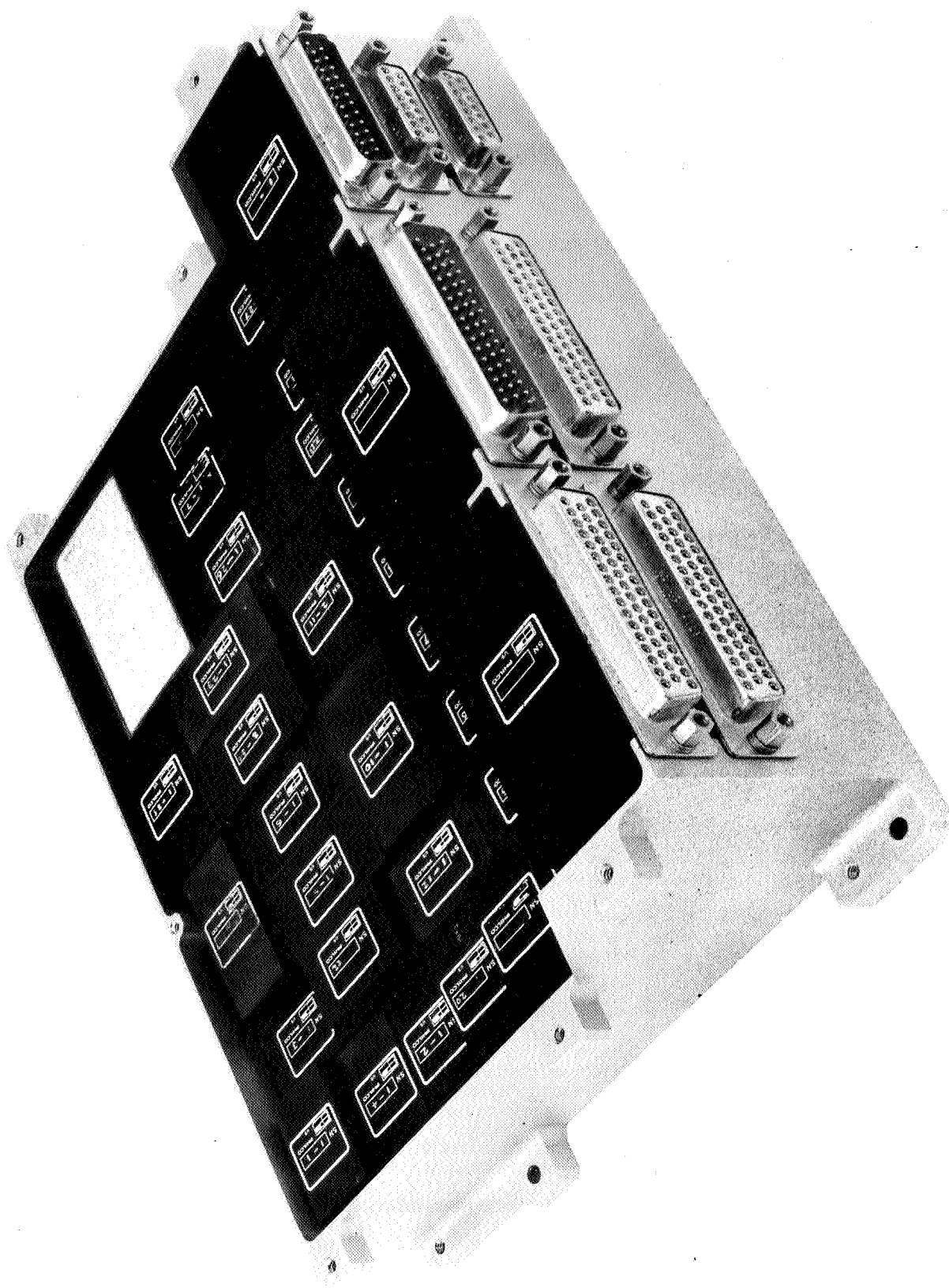


Figure 3-33 Telemetry Generator

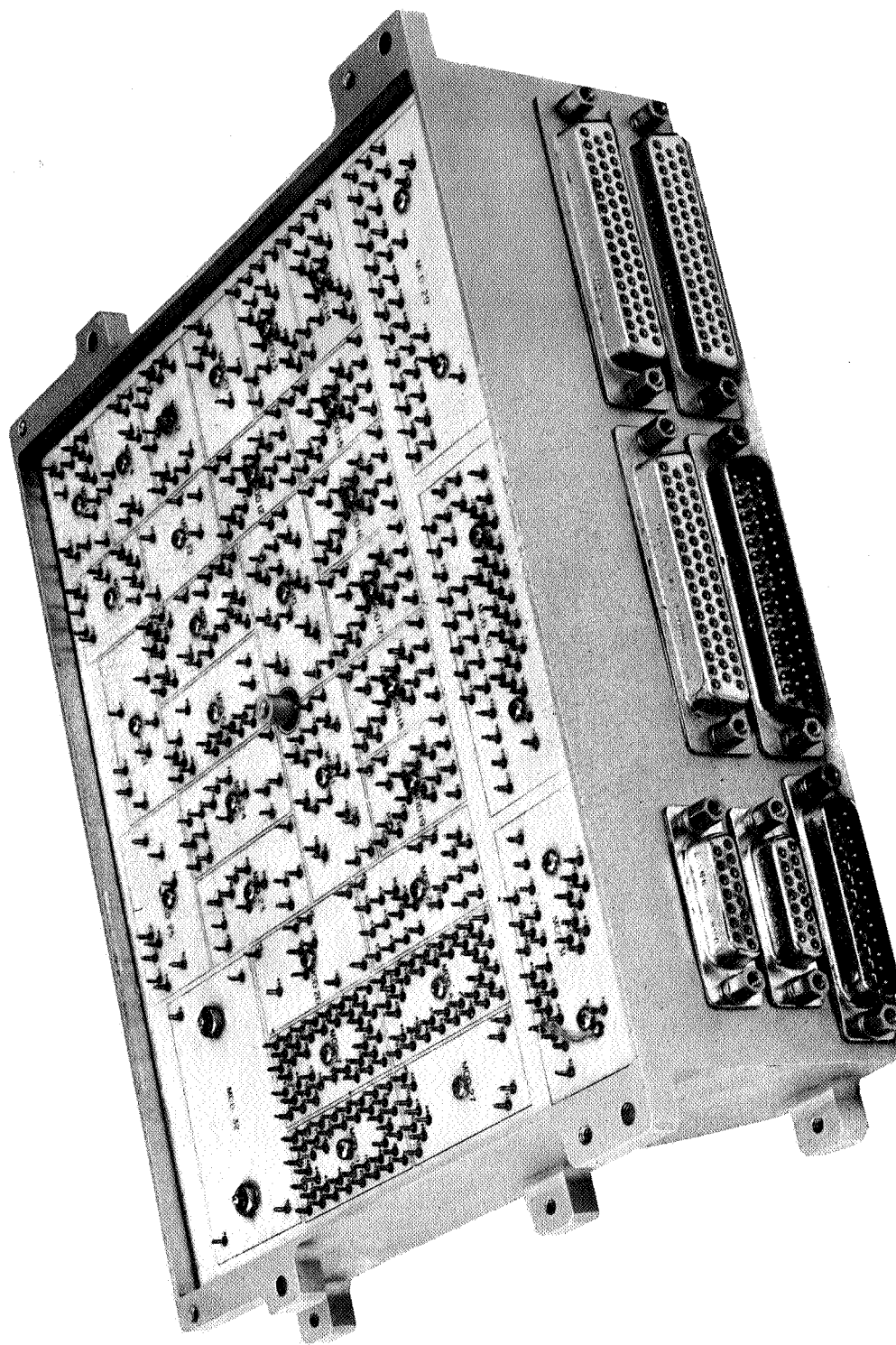


Figure 3-34 Teletype Cry Generator (Rear View)

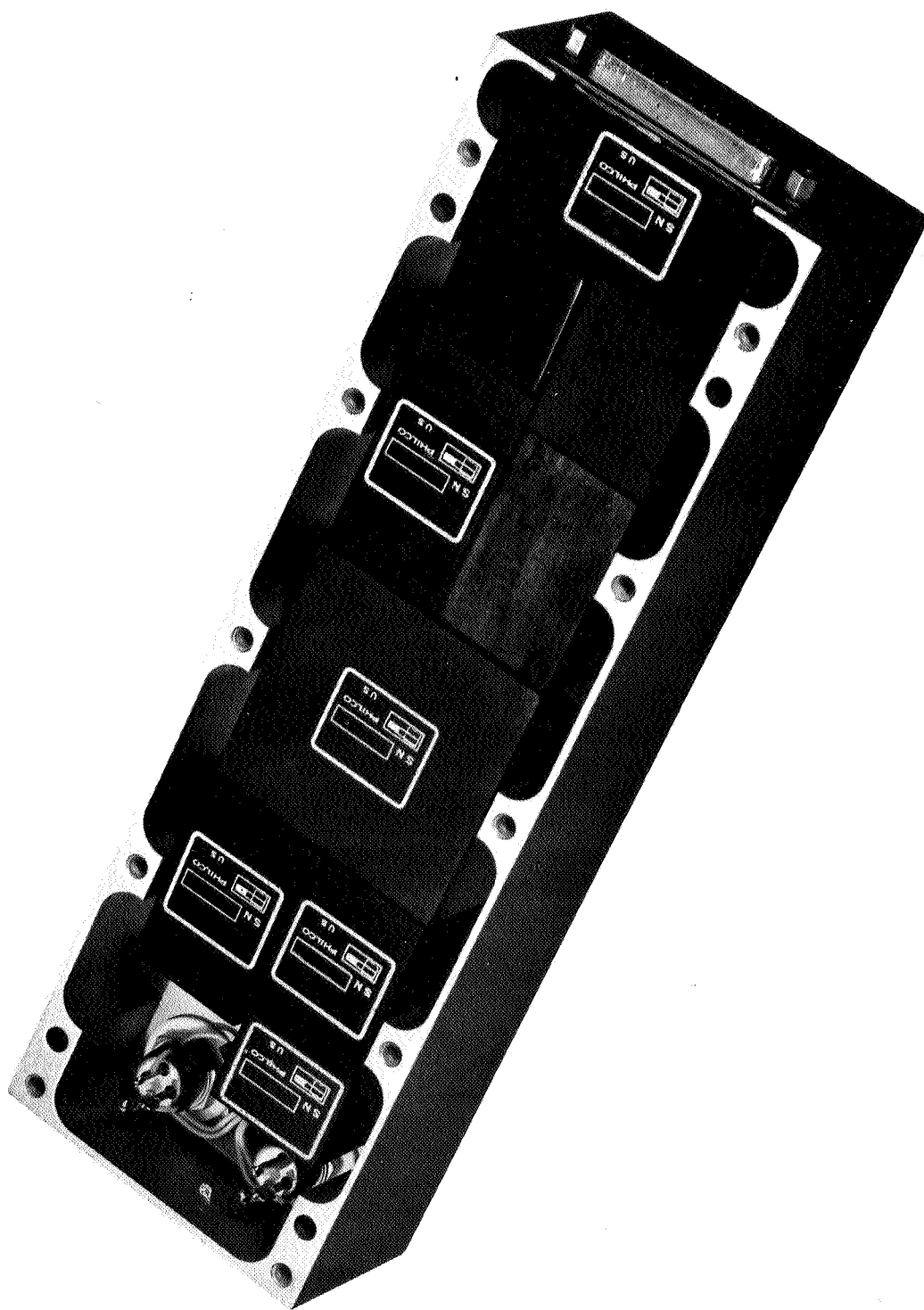


Figure 3-35 DC/X C printer (Top View)

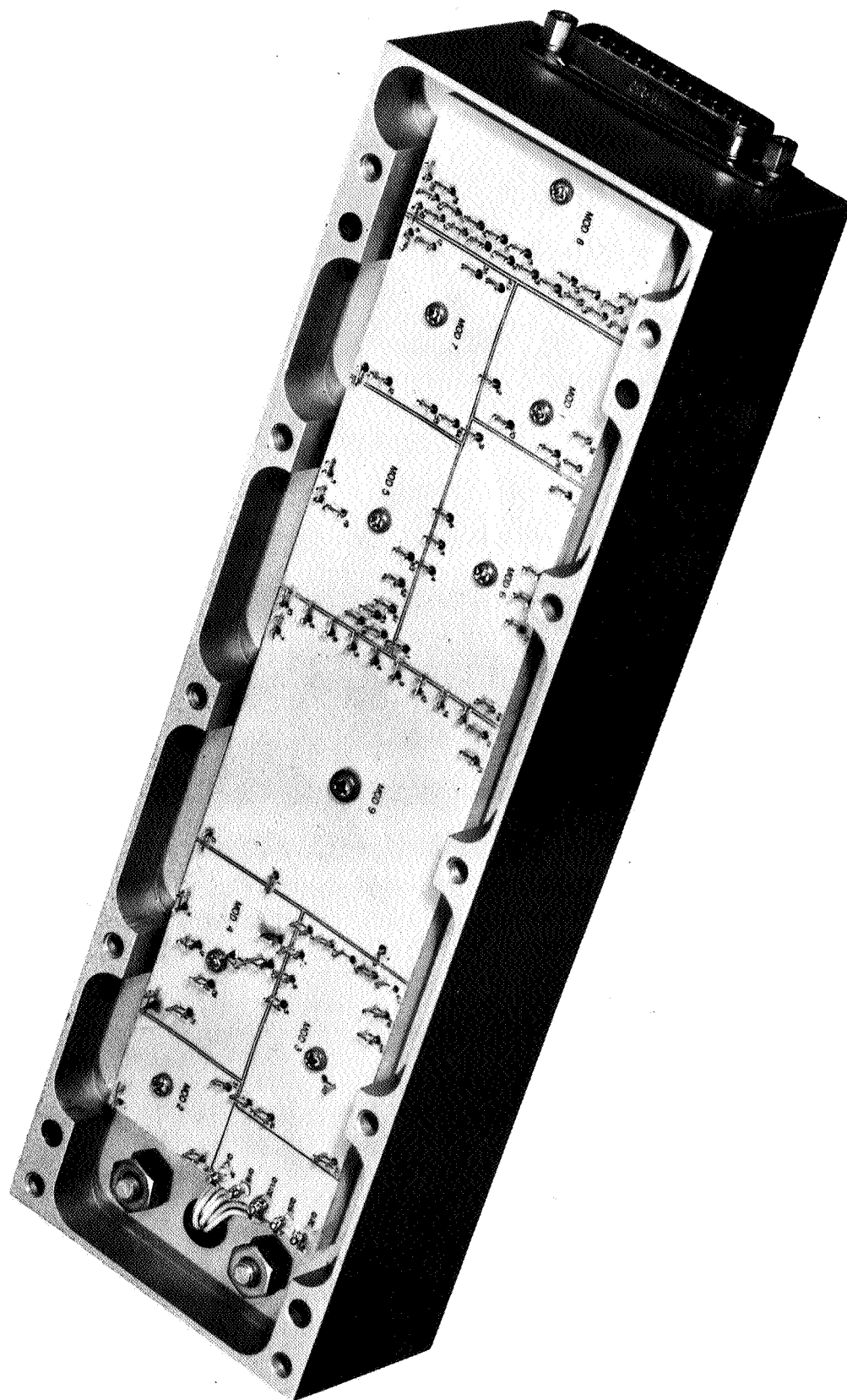


Figure 3-36 DC/DC Converter (Bottom View)

The power amplifier DC/DC converter serves to isolate the power amplifier from noise and transients which may be present on the power bus. It may be packaged with the power amplifier, since highly precise regulation requiring many components is not necessary. Noise filtering and transient suppression circuitry is included, along with voltage stabilization components.

3.4.3.6 Event Timer

The event timer selected for the experimental satellite is of the type proven in many space flight programs. It initiates, on command, a preselected timing sequence consisting of 12 intervals; each interval can be individually adjusted for a duration of from a fraction of a second to several hours. The unit contains 24 sets of double-throw contacts to provide the desired outputs. When a start command is received, one 12-event sequence will be completed. At any time during a sequence, the timer may be commanded to stop or restart at the beginning of the sequence. The device is composed of three major parts; a low frequency magnetic oscillator which functions as the internal time clock, a resettable binary counter which counts the clock output, and a shift register with associated parer output circuits. Magnetic core transistor logic is used to provide high reliability and long life.

The timing sequence is initiated by ground commands or by switch closures during satellite separation, antenna deployment, spin-up, or similar events. For example, it is used to remove power from the TWT amplifiers at the end of a prescribed time interval, such as one hour. This prevents the batteries from being discharged to too low a level in the event that a ground command to turn off the TWT amplifiers is not received by the satellite.

3.4.4 Electrical System Performance

3.4.4. I Introduction

A brief discussion of the performance of the electrical system is given in this section of the report. Several user configurations are assumed and typical performance parameters assigned. Link calculations are shown for the Fan Beam, Command, Telenetry, and Star Detector Subsystems. The effects of the satellite environment, including aging, cycling, and radiation, temperature are also presented.

3.4.4.2 Fan Beam Transmission Subsystem

The Fan Beam Transmission Subsystem consists of a frequency generator, an exciter, two TWT amplifiers with self-contained power supplies, a TWTA control unit, a communications DC/DC converter, two waveguide switches, and four fan beam antenna elements. A CW signal with a stability of $\pm 1 \times 10^{-8}$ (1 second) is generated by the frequency generator and supplied to the exciter. The exciter multiplies this signal up in frequency and by the use of isolators and filters delivers the proper level of RF drive to the two TWTA's. Each TWTA is rated at power output of 6 watts at frequencies in the vicinity of 8 GHz. Each TWTA is connected by means of X-band waveguide to the input ports of a waveguide transfer switch. The output ports of the transfer switch are connected to the input ports of a DP2T waveguide switch. The output ports of the DP2T switch are connected by means of waveguide to the four fan beam antennas. A schematic type diagram of the switching circuitry is shown in Figure 3-37.

Characteristics of the fan beams are described in Section 3.1.3. When the TWTA's are connected to antennas Nos. 1 and 2, the maximum power point of the beams is detected by the user. When the TWTA's are connected to antennas Nos. 3 and 4, a null detection method is used to determine user position. For the purposes of this section of the report, antennas Nos. 1 and 2 are energized.

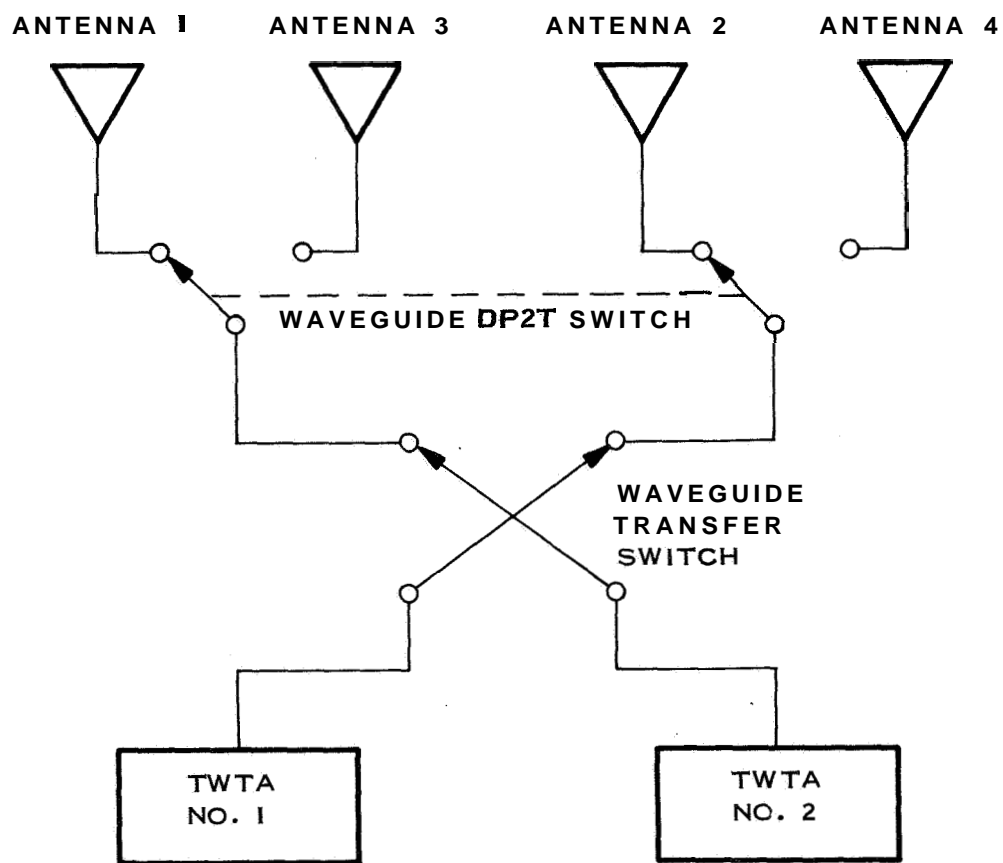


Figure 3-37 Waveguide Switching Schematic

Link calculations have been made in order that the performance of the fan beam subsystem can be evaluated. Two different ranges, 5,000 and 20,000 nautical miles, are considered. Three different size ground antennas are used in the calculations, together with corresponding variations in receiving system noise temperature. An AM receiver with an envelope detector and threshold circuits is assumed,

The gain of a fan beam antenna is given by:

$$G_A \approx \frac{31,000}{\theta_1 \times \theta_2}$$

where θ_1 and θ_2 represent the half-power beamwidths in the two orthogonal planes.

$$G_A \approx \frac{31,000}{102^\circ \times 2.5^\circ} = 122, \text{ or } 20.9 \text{ db}$$

Other values are given in Tables 3-5, 3-6, and 3-7.

The position accuracy of the fan beam navigation system is discussed in Section 13, and curves of accuracy vs smoothing time for various receiver parameters.

3.4.4.3 Telemetry Subsystem

The signal transmitted by the Telemetry Subsystem consists of a 400-MHz carrier which is phase-modulated ± 1 radian by a 1024-cycle subcarrier. The subcarrier is differential bi-phase modulated by a PCM serial bit stream at a rate of 256 bits per second. The 400-MHz carrier is fed to the satellite omni-antenna via coaxial cable and a SPDT coax switch.

It is assumed that the 40-foot parabolic antennas and associated receiving systems at the STADAN ground stations will be used for reception of telemetry and star detector data. The 400-MHz carrier from either subsystem will be used in tracking of the satellite by the 40-foot antennas.

Table 3-5 Fan Beam **Link** Calculations

WDL-TR2962 (V)

| | |
|---|----------------|
| Satellite Transmitter Power (6 watts) | +7.8 dbw |
| Waveguide/Switch Losses | -1.0 db |
| Satellite Antenna Gain | +20.9 db |
| Space Loss (20,000 n. mi., 8 GHz) | -202.0 db |
| Ground Antenna Gain (40-ft) | + 56.0 db |
| Ground Line Loss | -1.0 db |
| Polarization Loss | 3.0 db |
| Atmospheric Absorption | -0.4 db |
| Pointing Loss | -2.0 db |
| Received Carrier Power | -124.7 dbw |
| Receiver Noise Density, (503°K) (NF = 4 db or 438 K) (Antenna Temperature = 65°K) | -201.6 dbw/cps |
| Receiver IF Bandwidth (40 Hz) | + 46.0 db |
| Receiver Noise Density in IF | -155.6 dbw |
| Carrier-to-Noise Ratio | +30.9 db |

Table 3-6 Fan Beam **Link** Calculations

| | |
|---------------------------------------|----------------|
| Satellite Transmitter Power (6 watts) | +7.8 dbw |
| Waveguide/Switch Losses | -1.0 db |
| Satellite Antenna Gain | +20.9 db |
| Space Loss (5,000 n. mi., 8 GHz) | -189.8 db |
| Ground Antenna Gain (3" Horn) | +8.0 db |
| Ground Line Loss | -1.0 db |
| Polarization Loss | -3.0 db |
| Atmospheric Absorption | -0.4 db |
| Received Carrier Power | -158.5 dbw |
| Receiver Noise Power Density (1000°K) | -198.6 dbw/cps |
| Receiver IF Bandwidth (250 Hz)* | + 24.0 db |
| Receiver Noise Power Density in IF | -174.6 dbw |
| Carrier-To-Noise Ratio | + 16.1 db |

NOTE:

$$\text{IF } \omega_s = 100 \text{ RPM;}$$

$$\text{Min. Bw}_{\text{IF}} \equiv \frac{1}{T} = \frac{\omega_s}{\theta_B} =, \frac{360^\circ}{0.6 \text{ secs} \times 2.5^\circ} = 240 \text{ Hz}$$

Table 3-7 Fan Beam Link Calculations

| | |
|---|----------------|
| Satellite Transmitter Power (6 watts) | +7.8 dbw |
| Waveguide/Switch Losses | -1.0 db |
| Satellite Antenna Gain | +20.9 db |
| Space Loss (20,000 n. mi., 8 GHz) | -202.0 db |
| Ground Antenna Gain (2-ft) | +31.0 db |
| Ground Line Loss | -1.0 db |
| Polarization Loss | -3.0 db |
| Atmospheric Absorption | -0.4 db |
| Pointing Loss | -1.6 db |
| Received Carrier Power | -149.3 dbw |
| Receiver Noise Density (1000°K) | -198.6 dbw/cps |
| (NF = 4 db, T = 438°K) | |
| (Antenna Temperature = 562°K) | |
| Receiver IF Bandwidth (2 KHz) | +33.0 db |
| Receiver Noise Density in IF | -165.6 dbw |
| Carrier-To-Noise Ratio | + 16.3 db |

Table 3-8, Telemetry Subsystem Link Calculations, summarizes the performance of the subsystem at 20,000 n. miles range. As is shown in the table, a bit error rate, P_e , of 10^{-3} is obtained with an additional 4.2 db margin allowed for degradation in equipment performance.

3.4.4.4 Star Detector Subsystem

The Star Detector Subsystem also transmits a 400-MHz phase-modulated carrier which is received by the 40-foot antennas of the STADAN network. The same type of telemetry transmitter is used in this subsystem as is used in the Telemetry Subsystem. The phase modulator has been slightly modified to accomodate the wider bandwidth of the star detector video signal, To provide a suitable signal-to-noise ratio at the ground receiver, a 4-watt RF power amplifier has been added.

Table 3-9, Star Detector Subsystem Link Calculations, shows the performance of the link at 20,000 n. miles, Based on the satellite attitude and the corresponding signal-to-noise ratios available, several different methods of processing the video signal can be used at the ground station to obtain the desired accuracy.

3.4.4.5 Command Subsystem

The Command Subsystem receives tone-digital commands which are used to control selected spacecraft functions. These commands are transmitted over an amplitude-modulated RF link operating in the 120-150 megacycle range.

The command systems are available in the STADAN network, depending upon which station is controlling the satellite. A ground transmitter power of 5 kilowatts (37 dbw) and an antenna gain of 22 db are available at some sites, while at others the transmitter power is 250 watts (+23 dbw) and the antenna gain is +14 db. These parameters are included in Case 1 and Case 2 respectively of Table 3-10 Command Subsystem Link Calculations.

Table 3-8 Telemetry Subsystem Link Calculations

| | |
|--|----------------|
| Satellite Transmitter Power (250 mw) | -6.0 dbw |
| Cable/Switch Losses | -1.0 db |
| Satellite Antenna Gain | -2.0 db |
| Space Loss (20,000 n.mi.) | -175.9 db |
| Ground Antenna Gain (40 ft. dish) | +30.0 db |
| Line & Filter Losses | -1.0 db |
| Received Carrier Power | -155.9 dbw |
| Modulation Loss ($\beta=1$ radian) | |
| Carrier Power ($J_0(\beta) = 0.7652$) | -2.3 db |
| Sideband Power ($J_1(\beta) = 0.4401$) | -4.1 db |
| Total Received Power | |
| Carrier | -158.2 dbw |
| Sideband | -160.0 dbw |
| Receiver Noise Power Density (503°K) | -201.6 dbw/cps |
| (NF = 4 db, T = 438°K) | |
| (Antenna Temp. = 65°K) | |
| Carrier Tracking Loop Bandwidth (100 Hz) | +20.0 db |
| Sideband Demodulator Bandwidth (600 Hz) | +27.8 db |
| Carrier Noise Power Density | -181.6 dbw |
| Sideband Noise Power Density | -173.8 dbw |
| Carrier Signal/Noise Ratio | +22.8 db |
| Sideband Signal/Noise Ratio | +13.2 db |

$$E/N_o = 9 \text{ db for } P_e = 10^{-3} \text{ (includes 1 db for equipment degradation)}$$

$$\text{Margin for } P_e = 10^{-3} \quad +4.2 \text{ db}$$

Table 3-9 Star Detector Subsystem Link Calculations

| | |
|---|-----------------------|
| Satellite Transmitter Power (4 watts) | +6.0 dbw |
| Cable/Switch Losses | -1.0 db |
| Satellite Antenna Gain | -2.0 db |
| Space Loss (20,000 n. mi.) | -175.9 db |
| Ground Antenna Gain | +30.0 db |
| Line & Filter Losses | -1.0 db |
| Received Carrier Power | -143.9 dbw |
| Receiver Noise Temperature (NF=4 db) | 438°K |
| Antenna Temperature | 65°K |
| Total Receiver Noise Temperature | 503°K |
| Receiver Noise Density | -201.6 dbw/cps |
| Receiver IF Bandwidth (40 KHz) | +46.0 db |
| Receiver Noise Density in IF | -155.6 dbw |
| Carrier/Noise Ratio | +11.7 db |
| Modulation Loss ($\beta=1.3$ radians) | |
| Carrier ($J_0(\beta) = 0.6201$) | -4.1 db |
| Sideband ($J_1(\beta) = 0.5220$) | -2.6 db |
| Total Received Power | |
| Carrier | -148.0 dbw |
| Sideband | -146.5 dbw |
| Carrier Tracking Loop Bandwidth Improvement | |
| (40 KHz to 100 Hz) | +26.0 db |
| Sideband Filter Bandwidth Improvement) | |
| (40 KHz to 18 KHz) | + 35 db |
| Output Signal-to-Noise Ratio | |
| Carrier | +33.6 db |
| Sideband | +12.6 db |

Table 3-10 Command Subsystem **Link** Calculations

| | <u>Case 1</u> | <u>Case 2</u> |
|--|-----------------------|-----------------------|
| Ground Transmitter Power | +37.0 dbw | +23.0 dbw |
| Ground Antenna Gain | +22.0 db | +14.0 db |
| Ground Line Loss | -1.0 db | -1.0 db |
| Space Loss (20,000 n. mi.) | -167.3 db | -167.3 db |
| Spacecraft Antenna Gain | -3.0 db | -3.0 db |
| Spacecraft Line Loss | -1.0 db | -1.0 db |
| Received Carrier Power | -113.3 dbw | -135.3 dbw |
| Receiver Noise Power Density | -193.0 dbw/cps | -196.5 dbw/cps |
| (NF = 10 db/2610°K or 5 db/627°K) | | |
| (Antenna Temperature = 1000 K) | | |
| Receiver IF Bandwidth (40 KHz or 20 KHz) | +46 db | +43.0 db |
| Receiver Noise Density in IF | -147.0 dbw | -153.5 dbw |
| Receiver Carrier/Noise Ratio | +33.7 db | +18.2 db |
| Modulation Loss | -6.0 db | -6.0 db |
| Tone Filter Bandwidth Ratio (In Decoder) | +18.2 db | +15.2 db |
| Tone Signal-to-Noise Ratio | +45.9 db | +27.4 db |

The PCM/AM/AM mode is used, in which an eight-bit-per-word serial bit stream modulates a subcarrier tone, which in turn modulates the RF carrier. Bit rates between 10 and 100 bps and subcarriers in the 1 to 12 KHz range are used. For the calculations shown in Table 3-10, a bit rate of 50 bps and a subcarrier at a frequency of 10 KHz are assumed. A bit error rate of 1 part in 10^5 is achieved at 20,000 n. miles.

3.4.5 Power Management

Full utilization of the available battery and solar array capacity to achieve long and reliable lifetime in orbit requires careful design of the Power Subsystem. The detailed characteristics of each element of the subsystem must be accurately determined and complete compatibility must be achieved between these elements and the loads to which power is supplied. Degradation in performance due to the orbital environment must be taken into account in the design of the Power Subsystem in order to ensure that sufficient power is available throughout the entire life of the mission.

3.4.5.1 Solar Array Performance

The N/P silicon solar cells used in this solar array have a conversion efficiency of 10 percent at $+28^{\circ}\text{C}$ and at air-mass zero. Corning fused silica cover-glass slides, with a thickness of 20 mils, are bonded to the cells with a transparent adhesive. A multilayer, "blue" filter is vacuum-deposited on the inside surface of the cover-glass slide, and an anti-reflective coating is applied to the outer surface. This filter provides protection against ultraviolet radiation transmission losses in the adhesive, and decreases the cell's operating temperature, with a resultant increase in array power. Typical degradation factors of this type of solar array are listed in Tables 3-11 and 3-12.

Solar array V-I curves for the initial orbit and after one year are shown in Figure 3-38, and represent typical values for this array and this shape of satellite.

Table 3-11 Solar Array Degradation Factors

| Factor | Power Loss |
|---|------------|
| Filter installation losses (includes transmission losses through cover slides and adhesive) | 6% |
| Variation in solar intensity | 3.5% |
| Micrometeorite cover slide degradation | 2% |
| Variations in individual cell temperature and temperature coefficient | 5% |
| Solar cell installation loss | 1% |
| Diode and wiring loss | 3% |

Table 3-12 Environmental Degradation Factors

| Factor | Power Loss |
|---|------------|
| Ultraviolet radiation degradation to adhesive (1 year) | 2% |
| Random open circuit (1 year) | 3% |
| Particle radiation of medium solar flare (20 mil cover glass) | 5% |

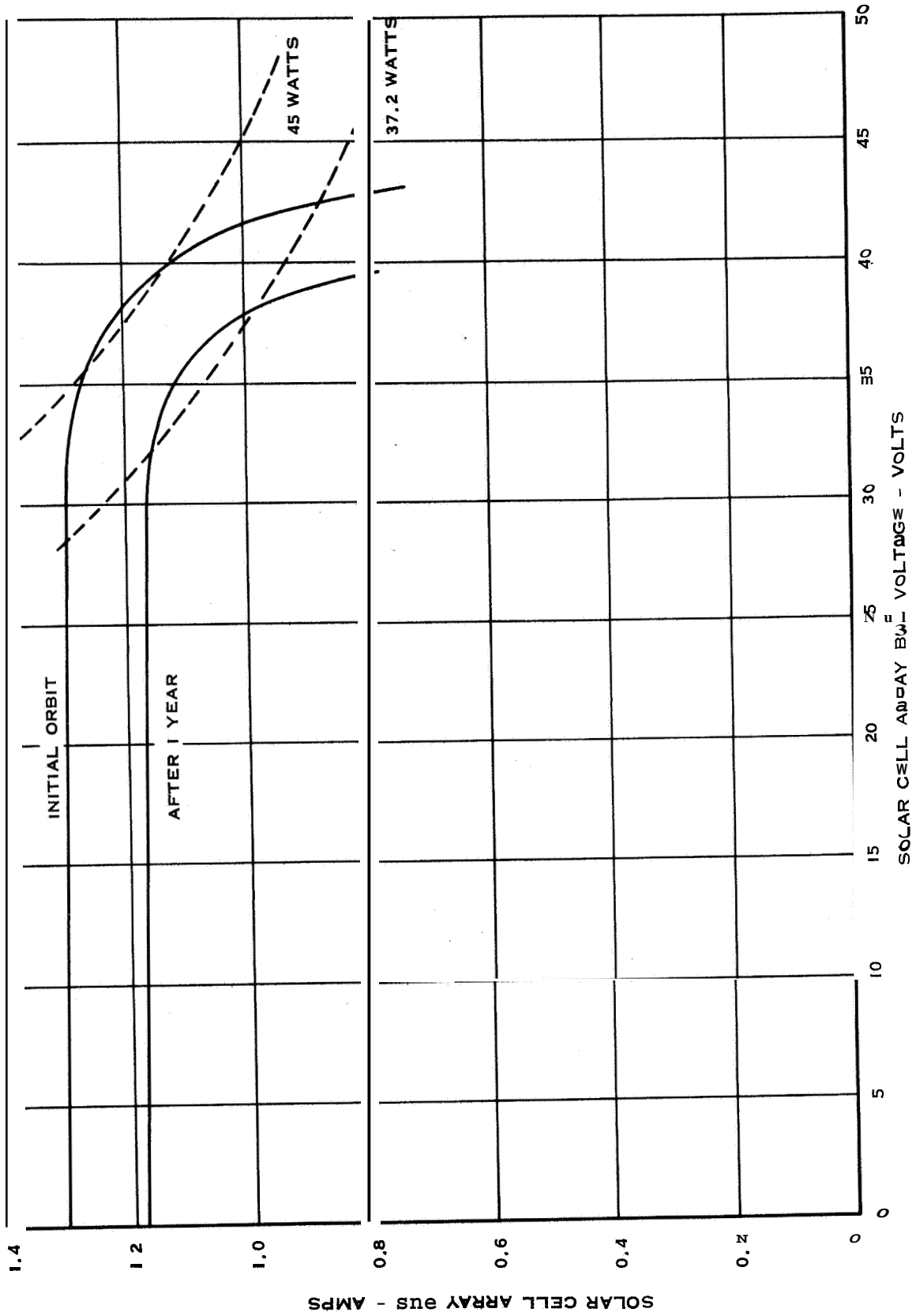


Figure 3-38 Solar Array Power Curve

3.4.5.2 Battery Performance

The hermetically sealed nickel-cadmium battery selected for this experiment has been utilized in other satellite programs and represents a current state-of-the-art capability.

The parameters governing design of the battery and charge control include the following items:

- a, Ampere-hour capacity of the battery
- b. Energy requirements of the load
- c. Satellite thermal characteristics
- d. Solar array capacity available for charging of the battery
- e. Number and duration of charge-discharge cycles during the mission
- f. Size and weight allocation for the battery and charge control
- g. Degree of confidence in achieving mission goals and objectives.

The selection of a suitable battery is governed by the peak load demand (and duration thereof) imposed on the battery. Other related factors include time available for recharging, maximum charging rate, and maximum depth of discharge. The latter factor, in conjunction with the number of charge-discharge cycles required, is of primary importance in determining the life of the battery.

Equations have been derived in which these related factors are used in determining the required ampere-hour capacity of a battery:

$$C = \frac{P_a T_d}{VX}$$

where

P_a = average output battery power, watts

T_d = battery discharge time, hours

V = nominal battery voltage, volts

X = depth of discharge, percentage of C

The output energy in a discharge cycle is $P_a T_d$, in watt-hours. The input energy from the solar array required during the time interval between discharge times to replenish the charge is $P_{ic} T_c$.

$$P_{ic} T_c = B \times \frac{E_c}{E_d} \times P_a T_d, \text{ in watt-hours}$$

P_{ic} = input power from solar array used for charging battery, watts

T_c = battery charging time, hours

B = overcharge required to compensate for battery inefficiency

E_c = battery voltage at end of charge

E_d = battery voltage at end of discharge.

Table 3-13, Power Subsystem Operating Modes, shows the status of the vehicle subsystems and components for five typical modes of operation. Table 3-14, Power Subsystem Power Requirements, lists the various components which are operating during each time interval, and the power consumption of each. Table 3-15 Battery Charging Availability, summarizes the battery bus and solar array bus power loads. The solar array power during the initial orbit and after one year of life is given, and the array power available for charging the batteries is also included. Inefficiency of the power control unit and the battery charge control are taken into consideration by listing a value of power consumption for each unit in the tables.

Table 3-13 Power Subsystem Operating Modes

| Time Interval | Mode | Function |
|---------------|--------------------|--|
| 1 | Telemetry Mode | Telemetry and command subsystems, solar array, power control unit, battery charge control, event timer, and TWTA control unit operating. Vehicle and component temperatures, antenna deployment, battery condition, and other parameters telemetered to read-out station. Command subsystem exercised. |
| 2 | Warm-Up Mode | Same as above, plus star detector electronics, communications DC/DC converter, frequency generator, and exciter now operating. Telemetry data from these components now included in data transmitted to read-out station. |
| 3 | Star Detector Mode | TLM #2 DC/DC converter, TLM transmitter #2, and RF power amplifier operating and telemetry subsystem turned off. Star detector data now transmitted to user station. |
| 4 | Fan Beam Mode | Same as above, plus fan beam TWTA #1 and #2 now operating. Fan beam transmissions and star detector data received by user stations. |
| 5 | Eclipse Mode | No solar array power available. Telemetry and command subsystems inoperative. Star detector data transmitted to user stations. Battery only source of power. |

WDL-TR2962(V)

Table 3-14 Power Subsystem Power Requirements

| Time Interval | Battery Bus | | Solar Array Bus | |
|---------------|--------------------|----------------|---------------------|----------------|
| | Equipment | Power | Equipment | Power |
| 1 | Event Timer | 0.60 w | Command DC/DC Conv. | 4.25 w |
| | Charge Control | 3.00 w | TLM #1 DC/DC Conv. | 4.75 w |
| | TWTA Control | <u>2.00 w</u> | Power Control Unit. | <u>3.00 w</u> |
| | | 5.60 w | | 12.00 w |
| 2 | Event Timer | 0.60 w | Command DC/DC Conv. | 4.25 w |
| | Charge Control | 3.00 w | TLM #1 DC/DC Conv. | 4.75 w |
| | TWTA Control | 2.00 w | Power Control Unit | 3.00 w |
| | Star Detector | <u>1.30 w</u> | Comm. DC/DC conv. | <u>8.75 w</u> |
| | | 6.90 w | | 20.75 w |
| 3 | Event Timer | 0.60 w | Command DC/DC Conv. | 4.25 w |
| | Charge Control | 3.00 w | Power Control Unit | 3.00 w |
| | TWTA Control | 2.00 w | Comm. DC/DC conv. | 8.75 w |
| | Star Detector | 1.30 w | | <u>16.00 w</u> |
| | TLM #2 DC/DC Conv. | 4.75 w | | |
| | RF Power Amplifier | <u>10.00 w</u> | | |
| | | 21.65 w | | |
| 4 | Event Timer | 0.60 w | Command DC/DC Conv. | 4.25 w |
| | Charge Control | 3.00 w | Power Control Unit | 3.00 w |
| | TWTA Control | 2.00 w | Comm. DC/DC conv. | <u>8.75 w</u> |
| | Star Detector | 1.30 w | | 16.00 w |
| | TLM #2 DC/DC Conv. | 4.75 w | | |
| | RF Power Amplifier | 10.00 w | | |
| | TWTA #1 & #2 | <u>50.00 w</u> | | |
| | | 71.65 w | | |
| 5 | Event Timer | 0.60 w | | |
| | Charge Control | 3.00 w | | |
| | TWTA Control | <u>2.00 w</u> | | |
| | Star Detector | 1.30 w | Eclipse | 0.0 w |
| | TLM #2 DC/DC Conv. | 4.75 w | | |
| | RF Power Amplifier | <u>10.00 w</u> | | |
| | | 21.65 w | | |

Table 3-15 Battery Charging Availability

| Time Interval | Available Solar Array Power | Solar Array Bus Load | Battery Bus Load | Battery Charging Power Available | t |
|---------------|-----------------------------|----------------------|------------------|----------------------------------|------------|
| 1 | 42.0 w | 12.0 w | 5.60 w | 24.40 w | t = 0 |
| 2 | 42.0 w | 20.75 w | 6.90 w | 14.35 w | |
| 3 | 42.0 w | 16.00 w | 21.65 w | 4.35 w | |
| 4 | 42.0 w | 16.00 w | 71.65 w | -45.65 w | |
| 5 | - | - | 21.65 w | - | |
| 1 | 36.0 w | 12.00 w | 5.60 w | 18.40 w | t = 1 year |
| 2 | 36.0 w | 20.75 w | 6.90 w | 8.35 w | |
| 3 | 36.0 w | 16.00 w | 21.65 w | -1.65 w | |
| 4 | 36.0 w | 16.00 w | 71.65 w | -51.65 w | |
| 5 | - | - | 21.65 w | - | |

Several example calculations are given to show how the experiments can be scheduled within the constraints of long battery life, solar array capacity, and the periods of visibility during an orbit. For intervals 1, 2, and 3, the solar array is able to simultaneously charge the batteries and supply the battery bus load. For intervals 4 and 5, the battery supplies a portion of or all of the load.

Case 1. For interval 4, assume the fully charged battery supplies approximately 46 watts of power for one hour.

$$\begin{aligned} C &= 6.0 \text{ A-H} & P_a &= 46.0 \text{ w} \\ V &= 30.0 & T_d &= 1.0 \text{ hr.} \end{aligned}$$

$$X = \frac{P_a T_d}{CV} = \frac{46.0 \times 1.0}{6.0 \times 30.0} = 20.6\%$$

This depth of discharge results in a life expectancy of more than 5000 cycles at battery temperatures between 20° and 130°F.

Assume time interval 1 occurs immediately following 4. Then approximately 24 watts of solar array power is available for charging the battery.

$$\begin{aligned} B &= 1.2 & E_c &= 1.47 \text{ v} & E_d &= 1.2 \text{ v} \\ P_a &= 46.0 \text{ w} & T_d &= 1.0 \text{ hr} \end{aligned}$$

Solving for T_c ,

$$T_c = \frac{B E_c P_a T_d}{P_{ic} E_d}$$

$$T_c = \frac{1.2 \times 1.47 \times 46.0 \times 1.0}{24.0 \times 1.2} = 2.82 \text{ hours}$$

Case 2. Assume the satellite goes into a one-hour eclipse (interval 5) with the batteries fully charged. Further, assume that interval 3 occurs next.

$$T_c = \frac{1.2 \times 1.47 \times 22 \times 1.0}{4.3s \times 1.2} = 7.43 \text{ hours}$$

From these two examples, it is evident that several experiments can be performed during each orbit with no detrimental effects to battery life.

3.4.5.3 Charge Control

One of the most critical elements in the Power Subsystem is the charge control unit. It must continuously monitor the condition of the battery and adjust the division of solar array power between the battery and the battery bus load. In conjunction with the power control unit and the command subsystem, the charge control unit ensures that the battery is charged to full capacity before load conditions listed for intervals 4 and 5 are imposed on the battery. The charging rate as a function of state of charge of the battery is also controlled to prevent loss of battery capacity due to the "memory effect." In addition, the charge control functions to isolate the solar array and power control unit from the effects of switching transients caused by the units powered from the battery bus.

SECTION 4

MISSION PLAN

4.1 EXPERIMENT PLAN

Since the Fan Beam Navigation Satellite as proposed is only meant to be an experiment it is desirable to gain as much useful information as possible on all phases of the navigation problem. The Fan Beam Navigation concept employs a spinning satellite generating thin fan beams of RF energy as shown in Figure 1-1. The three basic areas of investigation needing experimental verification are outlined below.

1. Satellite

- Spin axis damping by nutation damper
- Spin axis determination from onboard star detector
- Planarity of fan beam generation
- Reference pulse generation

2. Receiver

- Accuracy of RE fan beam detection

3. Calibration

- Ability to determine the spin axis orientation in time from onboard star detector data
- Accuracy of position determination by using the calibrated navigation satellite system.

To gain information on all the above areas of investigation in a parametric sense and minimize launch mission constraints, the orbit selected for the navigation experiment was the typical transfer orbit for a synchronous mission. The synchronous transfer orbit used as an experiment orbit will allow data to be acquired over a wide range of altitudes from 100 n.mi. to synchronous. A typical orbit profile is shown in Figure 4-3. This range of altitude will provide more than ample verification of this parametric system behavior. In addition, the orbit selected allows for

determination of low-level spin-axis drift due to thermal shocks induced by earth occultation of the sun and variations in satellite torques due to earth magnetic moments varying with altitude. Figure 4-1 shows the predicted change in angular momentum vector of the satellite due to the interaction of earth's magnetic field and the satellite dipole moment.

The experiment plan for a one-year test program is summarized in Table 4-1.

4.2 MISSION ANALYSIS

The navigation satellite performance evaluation and related experiments are to be conducted over a number of previously defined altitude regions between the transfer orbit radius limits of 100 n.mi. and 19,330 n.mi. (i.e., synchronous altitude). An obvious choice of mission profile to accomplish these objectives would be a synchronous altitude transfer orbit. Such a choice of orbit would permit the navigation satellite to ride "piggy-back" on a previously defined mission to be conducted in a synchronous altitude circular orbit. The navigation satellite would be released from the transfer vehicle at a previously defined altitude prior to injection of the primary payload into the synchronous orbit. The economical benefits derived from the utilization of the transfer phase of such a mission are obvious.

4.2.1 Orbit Selection

The transfer orbit considered most nearly optimal, for performance evaluation of the navigation satellite, would possess the following characteristics:

- a. Inclination. The vehicle would be launched due East from AMR. Such a maneuver would permit the injection of maximum payload onto the transfer orbit. This fact could be of extreme importance should the mission chosen possess payload weight limitations and a non-optimal launch azimuth (i.e., launch azimuth greater than 90°). Assuming a due East launch and injection maneuver, the transfer orbit would possess an inclination with respect to the Equator plane of approximately 28.5° . The inclination with respect to the ecliptic plane would vary with date of launch as

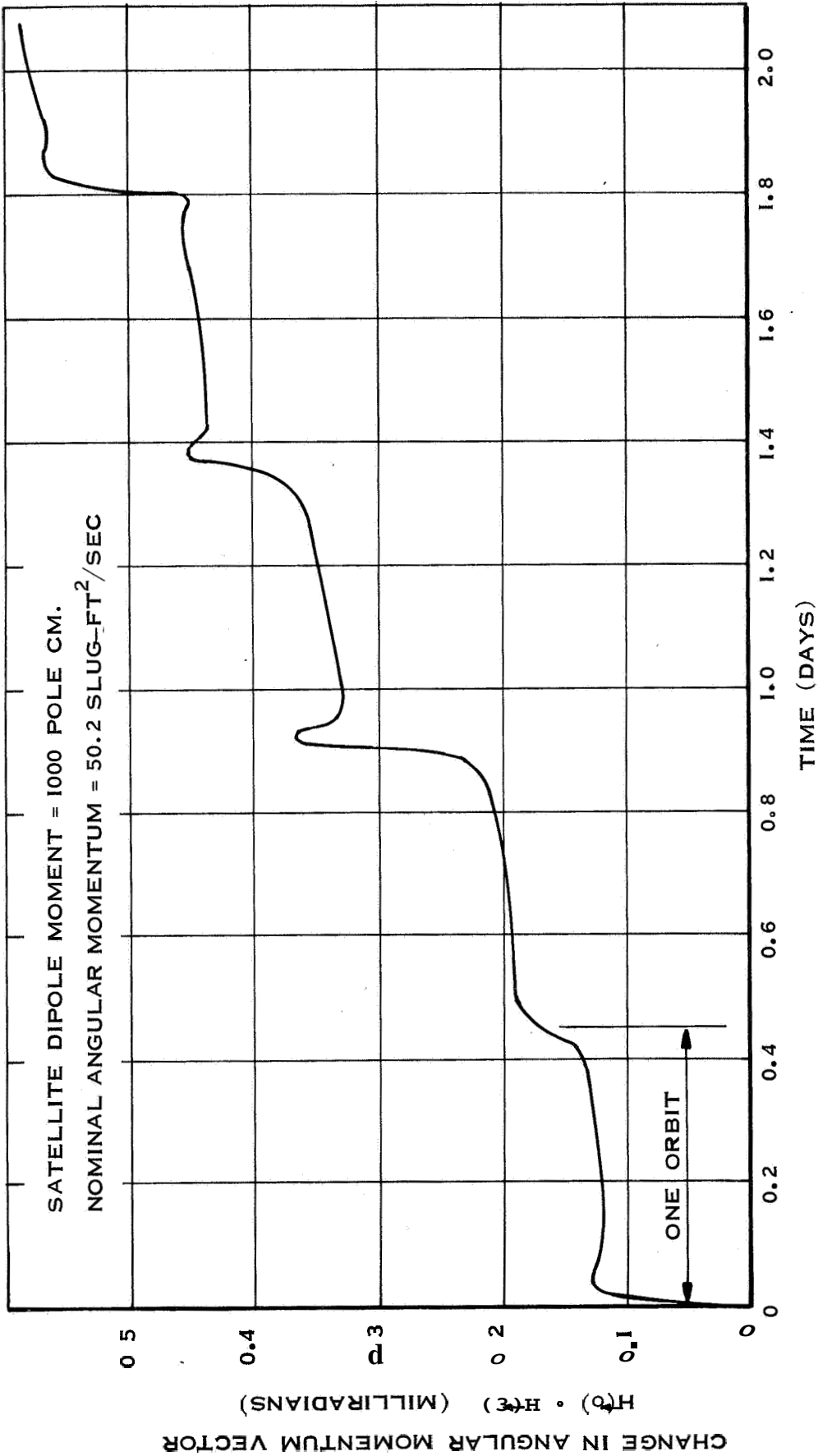


Figure 4-1 Predicted Change in Angular Momentum Vector Due to Magnetic Torques

TABLE 4-1
ONE-YEAR TEST PROGRAM OBJECTIVES

| EXPERIMENT BEING CONDUCTED | MONTH OF PROGRAM | | | | | | | | | | | |
|--|------------------|---|---|---|---|---|---|---|---|----|----|----|
| | I | 2 | 3 | 4 | 5 | 6 | 7 | 8 | 9 | 10 | 11 | 12 |
| 1. SPIN AXIS DETERMINATION FROM STAR DETECTOR DATA | | | | | | | | | | | | |
| 2. SPIN AXIS DETERMINATION FROM RF SENSED FAN BEAMS | | | | | | | | | | | | |
| 3. REFERENCE PULSE DETERMINATION AND SYSTEM CALIBRATION | | | | | | | | | | | | |
| 4. POSITION DETERMINATION FOR A RANGE OF SATELLITE ALTITUDES | | | | | | | | | | | | |
| 5. DETECTION ACCURACY FOR VARIOUS TYPES OF RF FAN BEAMS | | | | | | | | | | | | |
| 6. POSITION DETERMINATION ACCURACY VARIATIONS WITH OBSERVATION TIME | | | | | | | | | | | | |
| 7. EFFECTS OF THERMAL SHOCK ON SPIN AXIS MOTIONS AND FAN BEAM ANTENNAS | | | | | | | | | | | | |
| a. POSITION ACCURACY STUDIES FOR VARIOUS SIMPLIFIED USER TECHNIQUES | | | | | | | | | | | | |
| 9. POSITION ACCURACY STUDIES USING VARIOUS LOWER GAIN RECEIVING EQUIPMENT ON SHIPS, AIRPLANES, ETC. | | | | | | | | | | | | |
| 10. TURN OFF ALL BATTERY OPERATED POWER SYSTEMS AND CONNECT STAR DETECTOR TO PHOTOVOLTAIC POWER SUPPLY. MAKE SECULAR SPIN AXIS MOTION STUDIES FOR APPROXIMATELY 5 YEARS BEFORE DEACTIVATING THE SATELLITE. | | | | | | | | | | | | |

well as the time of launch. As illustrated in Figure 4-2, the minimum inclination with respect to the ecliptic occurs at winter solstice (21 December) for an injection time of local midnight. This observation is of course subject to the constraint that the line of apsides lie along the earth sun line with apogee pointing toward the sun. Subject to this constraint, the midnight launch time will always yield the minimum heliocentric inclination; however, the minimum varies over the yearly cycle from an absolute minimum of approximately 5.5° to a minimum of approximately 51° at summer solstice.

- b. Line of Apsides. The initial orientation of the line of apsides was chosen so as to minimize occultation time per orbit during the early portion of the mission. This requirement together with the low heliocentric orbit plane inclination angle permits maximum solar cell efficiency for the generation of electrical power. In particular, the low inclination angle minimizes the amount of shadowing, by the antennas, of the solar cells. Recall that the satellite is spinning at a 100 rpm rate about its axis of inertial symmetry and that the spin vector lies normal to the orbit plane.
- c. Eccentricity. The eccentricity will be that required to take a vehicle from a 100 nautical mile circular park orbit to a 19,330 nautical mile (synchronous) orbit.
- d. Orbit Stability. Establishing the park orbit with apogee toward the sun will cause the luni-solar effects to raise the perigee over the first half of the solar cycle. This effect will lessen those due to atmospheric drag on the vehicle. As a result, the lifetime of the satellite is well beyond the one year required for the basic experiments and systems evaluation to be performed.

* CONSTRAINT: LINE OF APSIDES LIES ON EARTH-SUN LINE

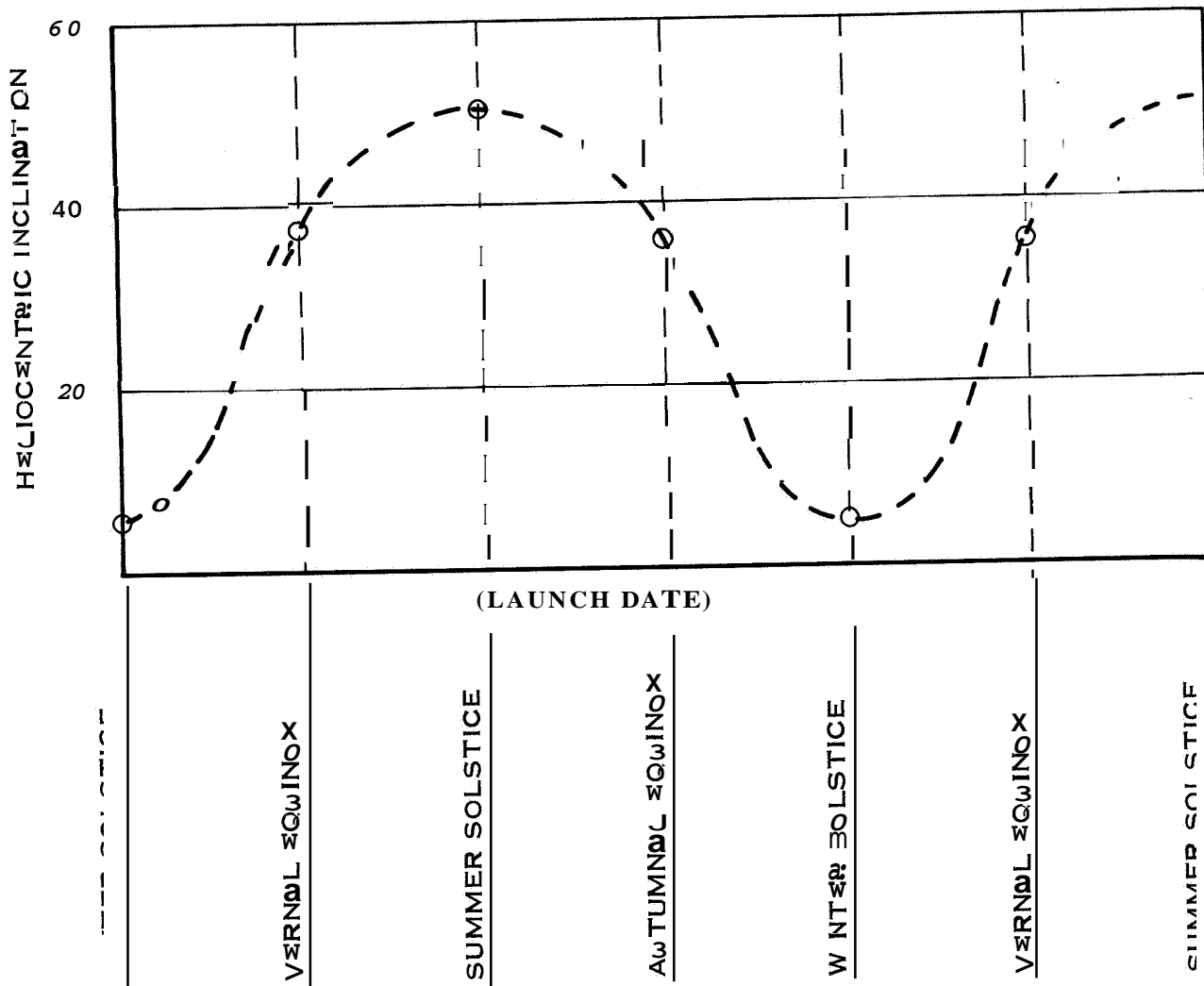


Figure 4-2 Minimum Heliocentric Inclination Angle as a Function of Launch Date

4.2.2 Orbit Profile

The orbit plane trajectory profile is shown in Figure 4-3. The six regions over which the system performance is to be evaluated are clearly defined in this figure. Each region covers an altitude increment of 6,000 kilometers.

The series of experiments and their sequence of performance are discussed in a following section. It suffices to say here that experiments defined for successive altitude regions will not be conducted sequentially.

Figure 4-3 indicates the navigation satellite will spend approximately 42 percent of its orbital period in the 6,000 kilometer altitude increment around apogee. As a result, the maximum time available per experimental region is approximately 21 percent of the orbital period (region 6). Also, as the radial velocity achieves its maximum value at a true anomaly of 90° (excluding zero eccentricity orbits), the minimum time available for experimentation in a given region occurs in region 2. Figure 4-4 verifies the fact that the true anomaly does pass through 90° in magnitude during this region, thus leading to the minimum time available of approximately 25 minutes. Region 6 contains an experimentation time of approximately two hours twenty minutes.

Figure 4-5 contains the radial profile of the orbit as a function of the time since perigee passage. It enumerates the altitude regions and the approximate number of minutes available for experimentation in each region.

A typical ground trace of the subsatellite point for the duration of one orbit is shown in Figure 4-6, assuming a transfer orbit injection at 28.5° latitude. To be specific, the subsatellite trace shown occurs during the first complete orbit after launch. Figure 4-5 also contains the approximate locations of stations in the NASA STADAN Tracking Network.

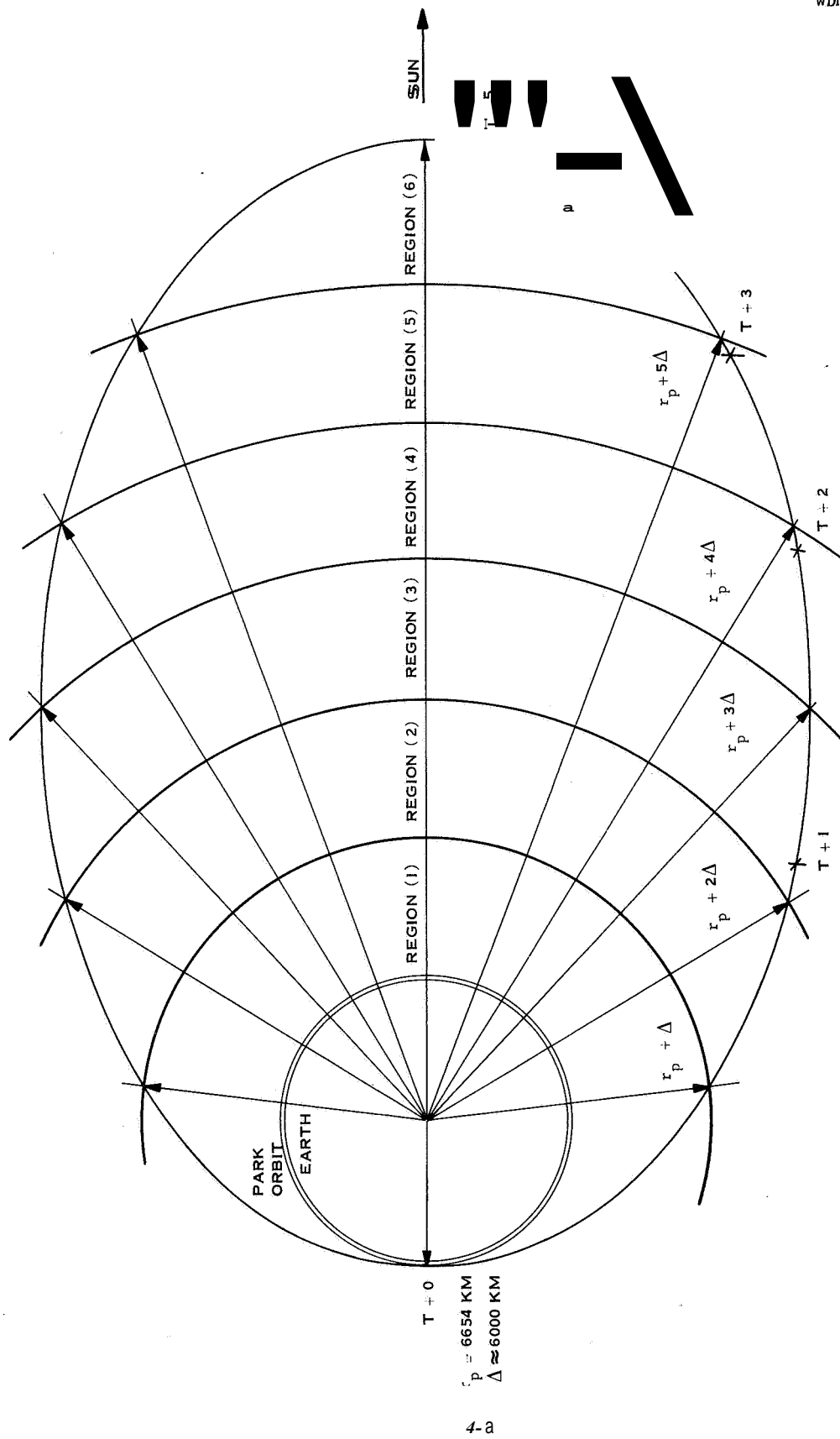
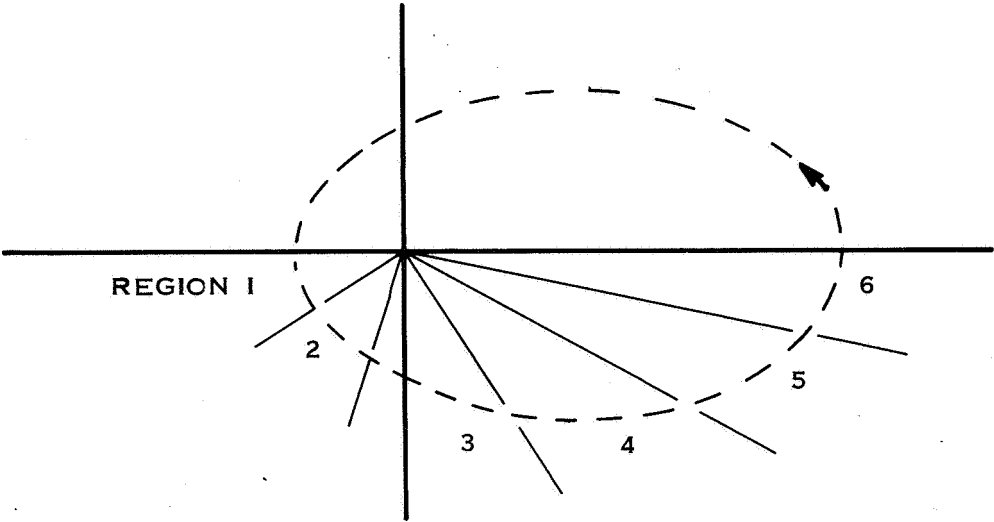
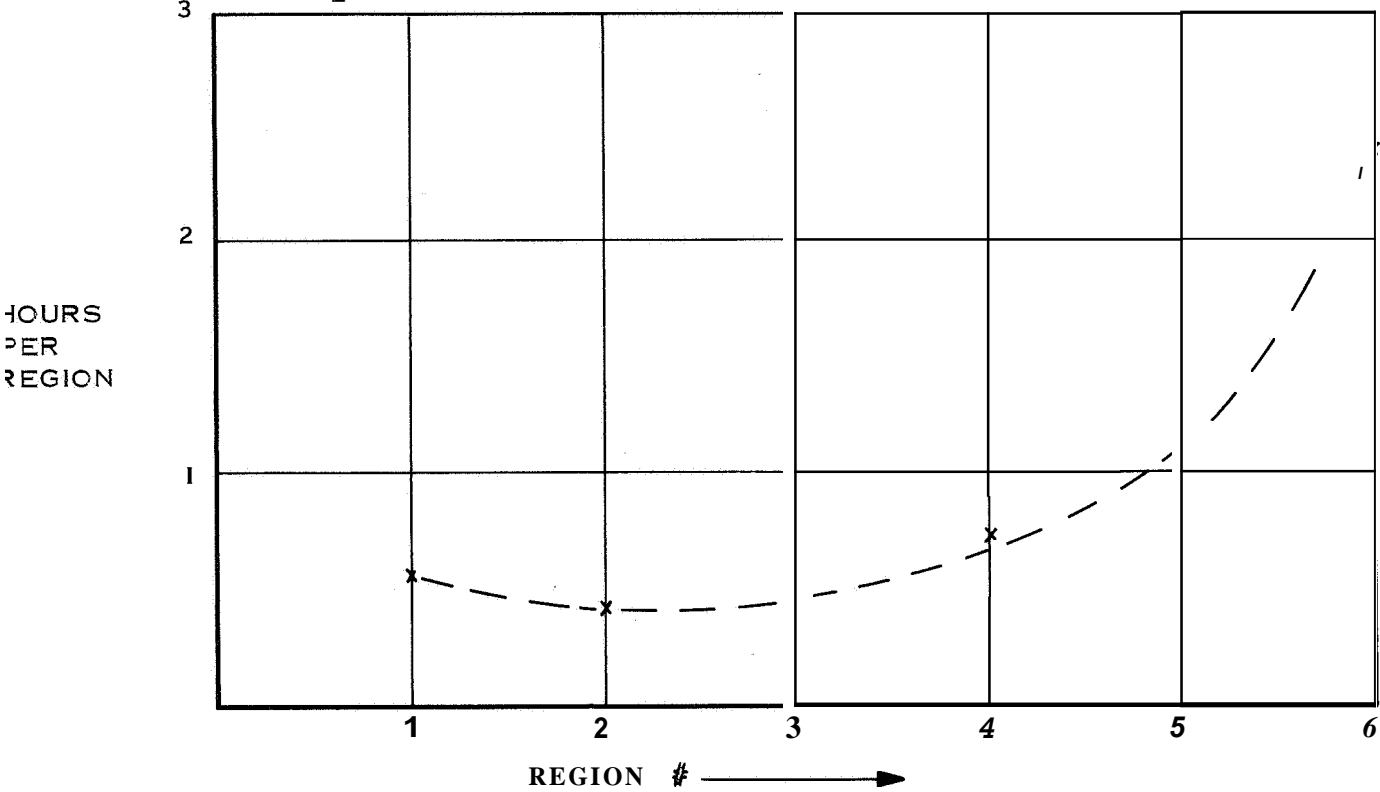


Figure 4-3 Orbit Plane Trajectory Profile

| PHASE # | 1 | 2 | 3 | 4 | 5 | 6 |
|-------------------------------|-----|-----|-----|------|------|------|
| $\frac{\% T/2}{\text{PHASE}}$ | 9.8 | 7.7 | 9.2 | 12.3 | 18.8 | 42.2 |

$\frac{T}{2} \triangleq$ HALF ORBIT PERIOD



$\Delta \parallel \tau \parallel$ IS 6 K PER REGION

Figure 4-4 Available Time for Experiment Evaluation as a Function of Altitude Region

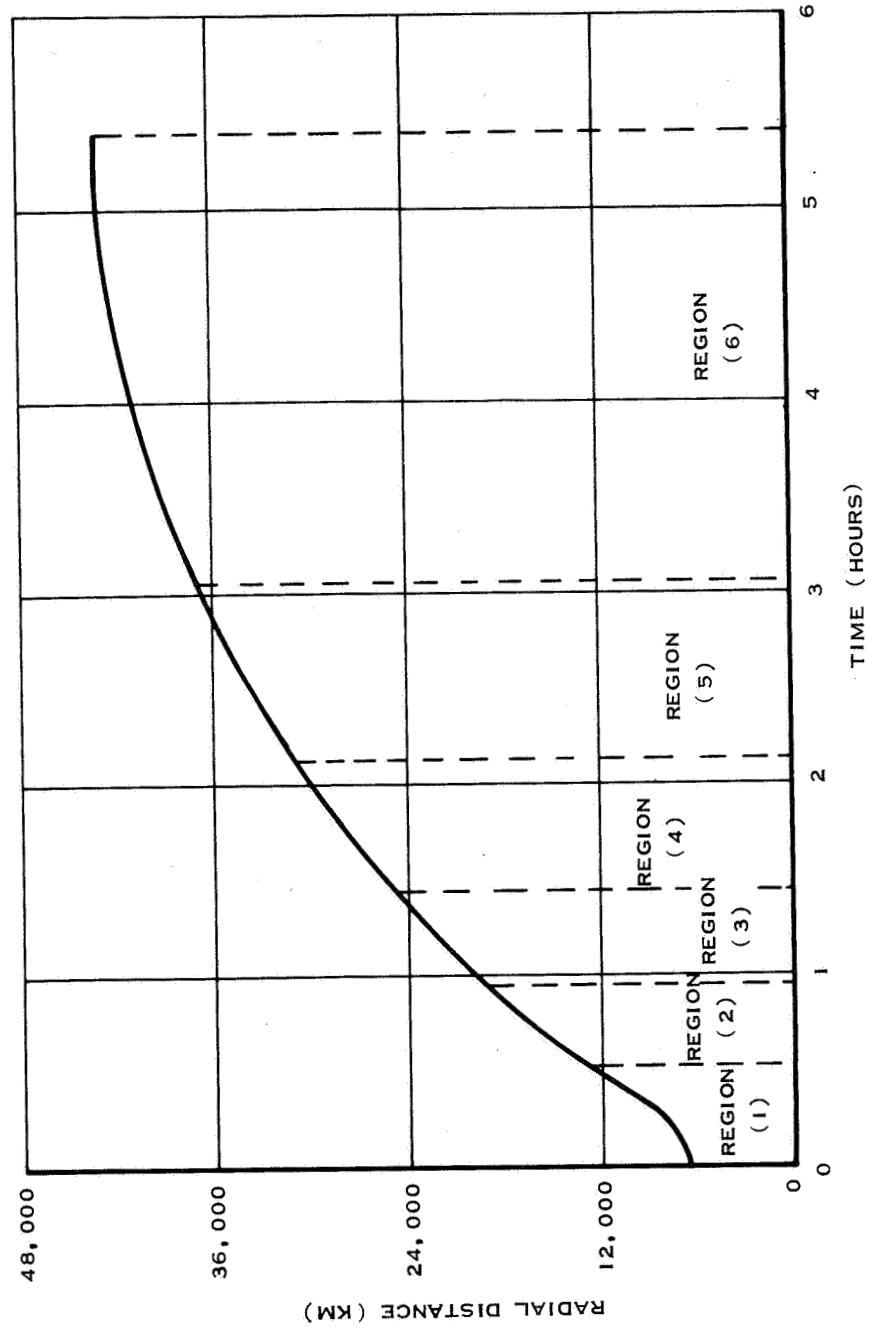


Figure 4-5 Radial Profile as a Function of Time

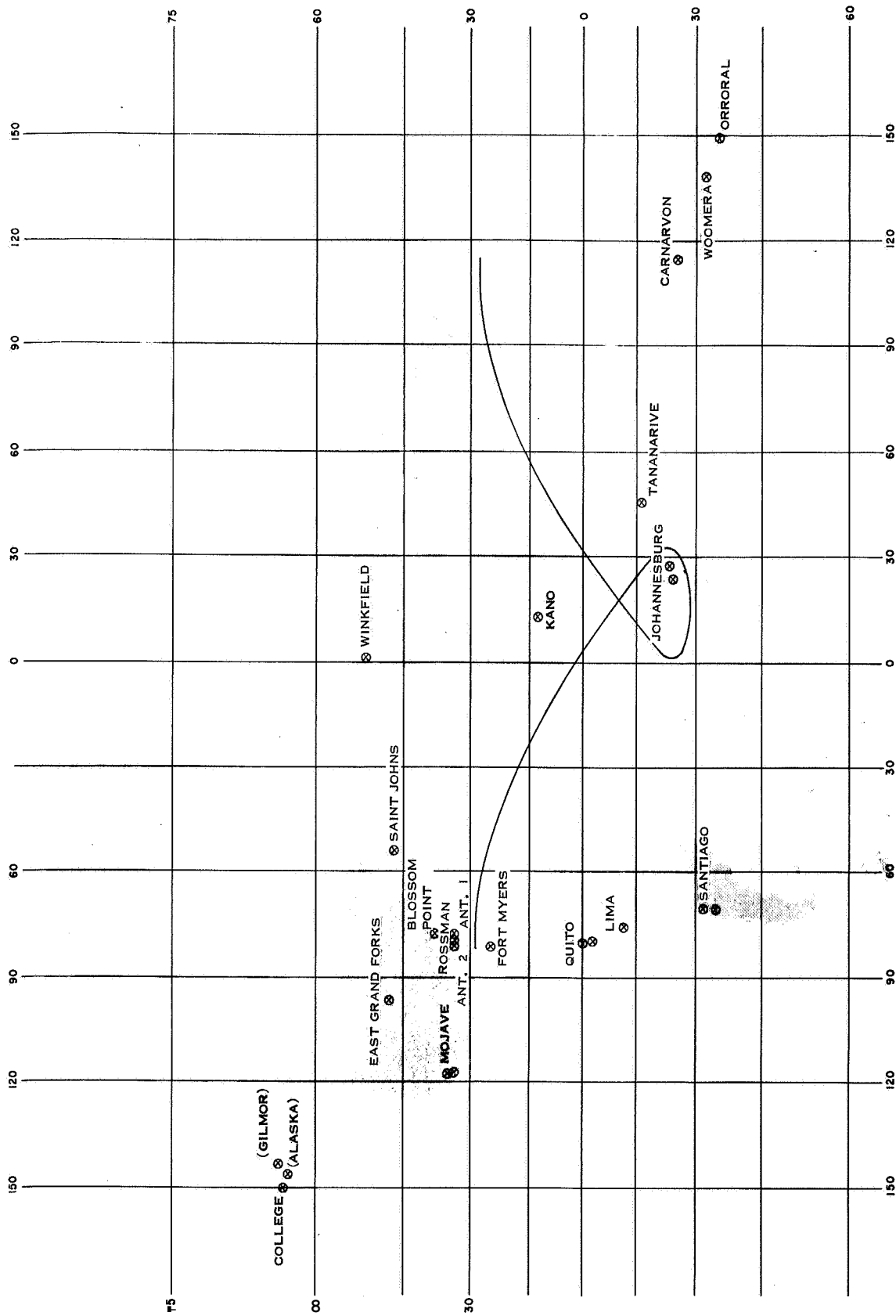


Figure 4-6 Typical Transfer Orbit Ground Trace

It is evident from this figure that complete tracking coverage of vehicles whose subsatellite point traces a curve over the Northern Hemisphere is impossible. Due to this lack of tracking capability, tracking or data acquisition in region one will not always be possible.

A total of approximately 190 to 195 degrees of earth rotation occurs between two successive perigee passes of the navigation satellite. As a direct result of this observation, it may be concluded that, at best, data acquisition and tracking in region one can be obtained only once every other orbit. The large relative velocity of the navigation satellite while near perigee will also complicate tracking and acquisition problems.

Continuous coverage of the vehicle when near apogee is certain. This is evident from Figure 4-6. Tracking coverage from at least one of the Southernmost stations in the STADAN System will always be possible, with two of the stations being able to track or interrogate the system a large portion of the time.

SECTION 5

DATA HANDLING SYSTEM

5.1 DATA HANDLING SYSTEM CONCEPT

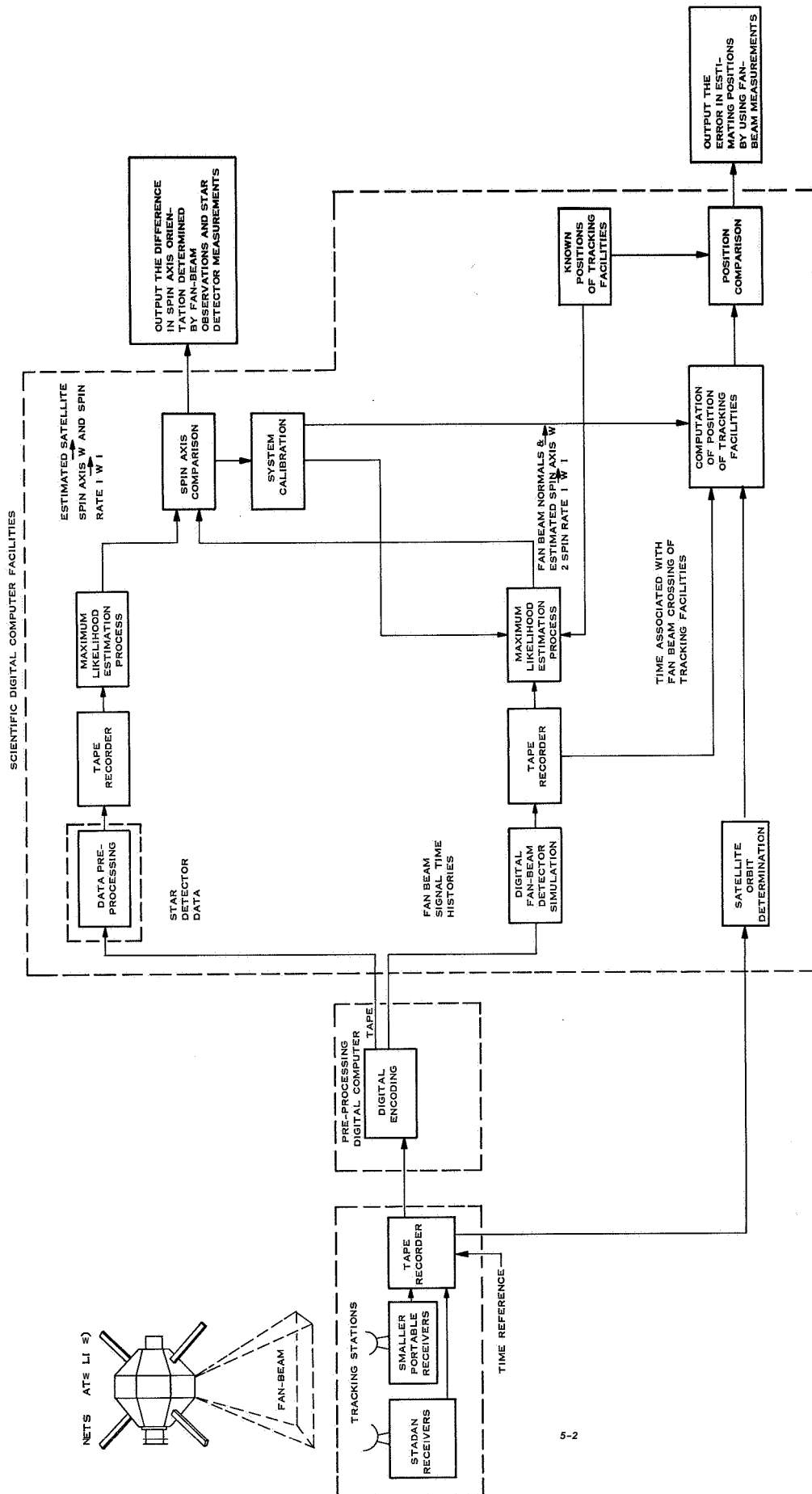
Data handling and processing of telemetered data from the navigation satellite, fan beam time histories, and group tracking (i.e., orbit determination) will be earth-based. That is, no data preprocessing will be done on board the satellite. Telemetered data will consist of the output from the star detector as well as other subsystem outputs not directly related to the observer and spin-axis estimation accuracy experiments to be described here.

The satellite experiments estimation (i.e., orbit determination) portion of the experiment will not be discussed here except to say that all tracking data will be furnished by either the NASA DSN or STADAN systems.

Figure 5-1 describes, in block diagram form, the method and logical flow of data processing to be used for navigation satellite system evaluation studies.

The data processing process has been designed to accomplish five basic objectives:

1. Estimate the inertial orientation of the navigation satellite spin axis from body-fixed star detector outputs.
2. Using the spin axis data determined via star detector measurements and observed fan beam passage times at the observing STADAN tracking facility, estimate the geocentric location of the tracking facility.
3. Using a priori knowledge of the tracker's location, the current best estimate of the satellite ephemeris, and the sensed fan beam crossings, estimate the spin axis orientation of the vehicle (i.e., navigation satellite).



WDL-TR2962(V)

FIGURE 5-1 Block Diagram of Scientific Digital Computer Facilities

4. Compare the star and tracker based estimates of the navigation satellite's spin axis. These results would be used together with a linear model of the antenna-vehicle-star detector configuration to determine position estimate sensitivity as a function of the parameters defining the model (i.e., antenna deflection, mounting angles, etc.). As a direct result of this study an efficient means or method of system calibration can be formulated. Such a method of system calibration would be continuous and self-adaptive *in* that it would monitor and provide its own corrections.

Only the comparison capability will be provided for in the current data processing format. A detailed study of an adaptive calibration scheme will be initiated later.

5. Compare the estimated STADAN tracker location with its actual location in order to properly assess the navigation accuracies attainable via the proposed navigation structure system.

After weighting each of the five basic objectives, it was decided that mission success was primarily dependent upon the feasibility of an onboard star detector. Therefore, a study was initiated to prove its feasibility and, if proven, demonstrate the accuracy to which the spin axis could be estimated. The following section contains a detailed description of the study and the conclusions drawn from it.

5.2 SPIN AXIS DETERMINATION USING STAR DETECTOR DATA

Figure 5-2 illustrates the principles of operation of the defined star detector. The $\hat{1}$ axis of the spacecraft is chosen as the nominal axis about which the spacecraft is spinning.

*_____

The results to be described were in part derived under NASA GSFC Contract No. NAS5-9682.

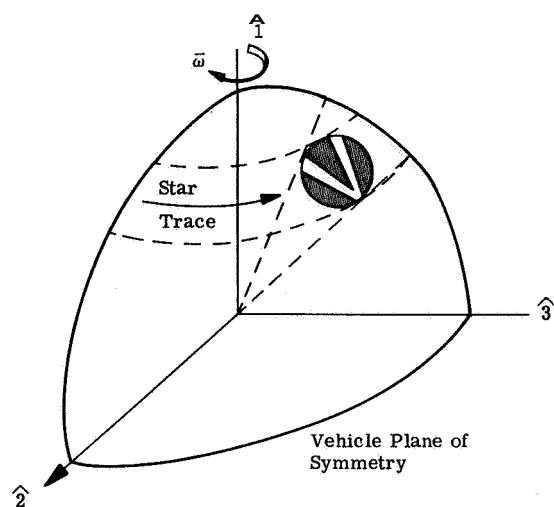
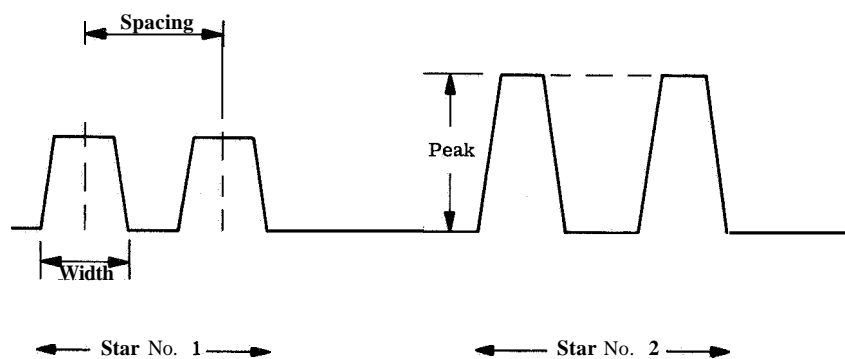


Figure 5-2 Star Detector System, Principle of Operation



PEAK Governed by Star Magnitude

WIDTH: Governed by Reticle Size

SPACING: Governed by Reticle Angle, Star Location and Spin Rate

Figure 5-3 Typical Star Data

An optical sensor with a V-shaped slotted reticle and a restricted field of view is oriented such that it scans a segment of the celestial sphere as the spacecraft spins. As each star passes through the reticle slots, light is focused on a photomultiplier. Hence, as the spacecraft spins, two pulses per star per revolution of the spacecraft are generated. These pulses are modulated on an RF carrier and received, demodulated, and recorded at a ground station.

Figure 5-3 depicts the pulse time sequence for two successive stars. As is illustrated on the figure, the pulse amplitude is determined by the star magnitude (as seen by the optics). The pulse width is dependent on the slot width of the reticle. The time spacing between the two pulses per star is governed by attitude rates, and the star orientation relative to the average spin axis direction over the time between pulses. As will be shown later, the time between the two pulses and an approximate knowledge of the spin rate determines that the average spin axis lies on a prescribed cone about the inertial star direction vector.

Although the technique will not be shown here, the stars can be identified in data preprocessing procedures utilizing this magnitude and relative spacing information.

The data flow required for spin axis estimation based upon star detector outputs is illustrated in Figure 5-1. The raw sensor data (train of pulses) is received at a ground station. After demodulation, these pulses and a time reference signal are recorded on a magnetic tape in analog form. The tape is then fed through a small digital computer wherein the analog information is converted to digital form and stored on a magnetic tape. Special procedures for accomplishing this conversion have been derived to avoid recording of non-useful digital data during periods when the analog data signal is very small.

The digital tape information along with digital tape of the star catalog is then preprocessed on a high speed computer. Following preprocessing, star identification, star crossing times, and star direction information are obtained. The preprocessing is also designed such that obviously erroneous data points are removed. A digital tape containing star identification, time of crossing, and star direction is recorded. Following the preprocessing, the stored data is used as input information to a digital computer implementation of the Maximum-Likelihood estimator.

The results to be discussed later were obtained by means of simulation of the system through the data preprocessing stage. That is, the vehicle dynamics and the detector geometry were simulated and a table of star identification and star passage time was computed. The passage times were then corrupted by the addition of random errors in the table containing the time of reticle slot crossing. The simulated data was used to evaluate the performance of the Maximum-Likelihood iteration technique. It was also used to perform an error analysis relating the various design parameters and the accuracy of the state estimation.

It should be emphasized that the implementation was designed for a flight test experiment. Following the experimental demonstration the whole procedure can be streamlined so that the attitude time history can be computed either onboard the spacecraft or at a tracking site.

The problem was formulated for a Maximum-Likelihood estimation procedure. As is well known, this procedure is readily formulated if one has a mathematical statement relating the states to be estimated to the observations for the case under consideration. The observation is defined to be a value of the independent variable, time. Hence, a slight variation to the more straightforward approach, where the observation at a given time is a function of the state variables, is required. Before discussing this variation, however, the model dynamics will be considered.

The equations of motion of an axially symmetric, spinning body in free precession may be written in the form

$$\hat{n}_b(t) = T_{H_o} \left(\frac{|H_o|}{J_{ns}} t \right) T_{\hat{1}}(ct) \hat{n}_b \quad (1)$$

\hat{n}_b = 3 vector in body coordinates at time zero

J_s = symmetric moment of inertia

J_{ns} = nonsymmetric moment of inertia

c = $(1 - J_s/J_{ns}) P$

P = body rate about $\hat{1}$ axis

\hat{H}_o = a unit vector in the direction of the initial angular momentum; expressed in body coordinates

$|H_o|$ = magnitude of the angular momentum

A transformation, $T_{\hat{a}}(\alpha)$, such as the one used in equation (1), is defined to mean a rotation about the vector \hat{a} through the angle α .

One may also express the vector, \hat{n} , in inertial coordinates by:

$$\hat{n}_I(t) = T_{\hat{2}}(\theta) T_{\hat{3}}(\psi) T_{\hat{1}}(\varphi) \hat{n}_b(t) \quad (2)$$

where :

θ = pitch angle

ψ = yaw angle

φ = roll angle

The transformations, T , given in equations (1) and (2) are orthogonal transformations for the orthonormal basis vectors chosen here.

If we let $\hat{n}_{I_i}(t)$ describe a vector normal to the i^{th} reticle slot, then an expression which is true when the k^{th} star passes the i^{th} reticle is:

$$y_{i,k}(t_{i,k}) = \hat{n}_{I_i}'^*(t_{i,k}) \hat{s}_k = 0 \quad (3)$$

* The prime notation implies the transpose operation.

The unit vector, \hat{s}_k , is directed toward the k^{th} star. The inertial coordinate frame used here is equator and equinox of 1950. Equation (3) simply shows that at the time the k^{th} star crosses the i^{th} reticle slot, the star vector, \hat{s}_k , and the vector normal to the reticle slot, $\hat{n}_{I_i}(t)$, are perpendicular.

By the use of equation (3) the time of observation measurements, $t_{i,k}$, may be related to the state variables.

One may also derive

$$y_{i,k}(t_{i,k}) = \nabla_X \left(y_{ik}(t_{ik}) \right) \bigg|_{t_{i,k}} \bar{x} + \frac{d}{dt} \left(y_{ik}(t_{ik}) \right) \Delta T = h\bar{x} + b \quad (4)$$

$\nabla_X(A) \big|_t$ means the gradient of A with respect to the state variables, X, at time, t. In the formulation used here the gradients and time derivative are evaluated at the time, t_{ik} , of the measured k^{th} star crossing of the i^{th} reticle slot.

In equation (4) the expected value, $E(\Delta T)$, is zero, and

$E(\Delta T)^2$ = the variance of the random error in the time measurement. (Depends on the star magnitude)

We also define

$E(b)^2 = q$ = the variance of the random error in the dot product of the star vector and the reticle slot normal vector

With these definitions the Maximum-Likelihood estimation procedure is readily formulated as:

$$X_{j+1} = X_j + (H'Q^{-1}H + P_o^{*-1})^{-1} H'Q^{-1} \begin{pmatrix} y_1 \\ y_2 \\ y_3 \\ \vdots \\ y_n \end{pmatrix}$$

P_o^{*-1} is nominally set at zero. It was included for purposes of convergence control.

x_j = the j^{th} estimate of the state variables, x

y_n = the dot product residual computed from the j^{th} estimate of x

$$H = \begin{pmatrix} h_1 \\ h_2 \\ \vdots \\ h_n \end{pmatrix} \quad Q = \begin{pmatrix} q_1 & \cdot & \cdot & \cdot & 0 \\ \cdot & q_2 & & & \cdot \\ \cdot & & & & \cdot \\ \cdot & & & & \cdot \\ 0 & \cdot & \cdot & \cdot & q_n \end{pmatrix}$$

n = the number of measurements included-for the j^{th} iteration.

In the procedure used, n is not necessarily the complete set of observations. A test was made on the residuals and if they became larger than an input test value, a new value of x was computed. This simple technique provides a means of insuring convergence of the procedure.

The state variables and their initial values, as used in the simulated data, are shown in Figure 5-4. The first six states do not require explanation. The optic geometry, which defines the next three states, is shown in Figure 5-2. The last state variable is the moment-of-inertia ratio.

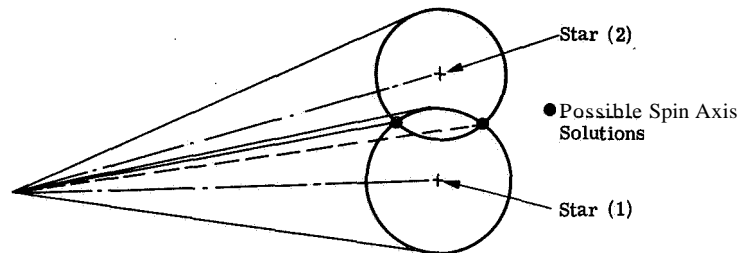
The digital computer implementation was made such that by input selection x_{10} could either be included or neglected.

The starting values of the states are also shown in Figure 5-4. The starting estimate of the first four states is computed from the raw data by an approximate solution to be discussed later. States x_5 and x_6 are assumed to be zero. This is equivalent to stating that no precession exists. The states x_7 and x_8 are defined by alignment and mounting of the optics on the body. x_9 is initially defined to be zero, x_{10} is determined by preflight calculations and perhaps laboratory measurements. The values shown for the last four states correspond to those used for simulating the raw data. Actual values would be determined for a specific satellite and sensor mounting.

* Convergence is defined as occurring when the magnitudes of the computed incremental state vector, \bar{x} was less than some input constant vector, δ .

| | | | | | | |
|---|----------|---|--------------|---|---|---|
| STARTING VALUES ↑ Determined by Approximation Solution ↓ 0 48.5 45 0 1.2 | X_1 | = | θ | = | PITCH | } INERTIAL TO BODY AXIS ANGLES AT EPOCH TIME |
| | X_2 | = | ψ | = | YAW | |
| | X_3 | = | ϕ | = | ROLL | |
| | X_4 | = | p | = | ROLL BODY RATE AT EPOCH TIME | |
| | X_5 | = | q | = | PITCH BODY RATE AT EPOCH TIME | |
| | X_6 | = | r | = | YAW BODY RATE AT EPOCH TIME | |
| | X_7 | = | β | = | PRINCIPAL AXIS TO OPTICAL AXIS ANGLE | |
| | X_8 | = | α | = | ANGLE BETWEEN RETICLES | |
| | X_9 | = | Σ | = | ROTATION OF OPTICAL AXIS FROM CENTERLINE | |
| | X_{10} | = | J_s/J_{ns} | = | RATIO OF MOMENTS OF INERTIA | |

Figure 5-4 State Definition and starting Values



P Estimated by Time to go from Star (1) to Star (2)

Figure 5-5 Approximate Solution

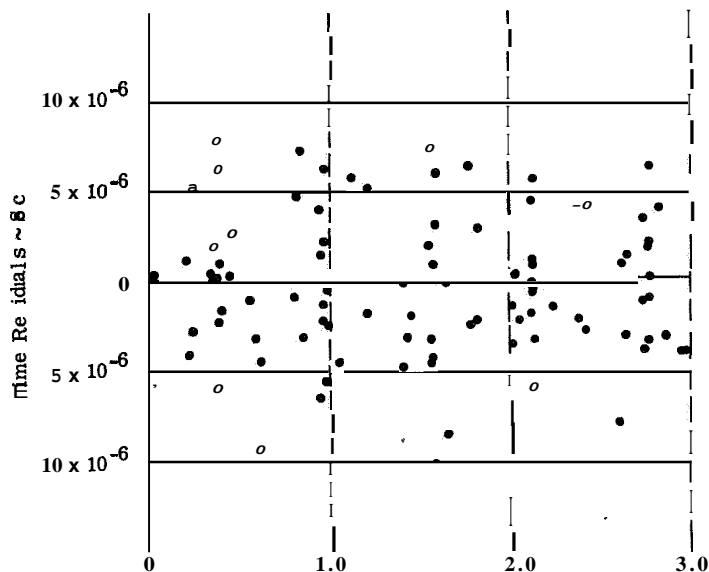


Figure 5-5 pictorially illustrates the manner in which an initial estimate of the first three state variables was computed. As was mentioned earlier, the time interval required for the star to pass both reticle slots can be used to define a cone about the star on which the average spin axis must lie. To compute this, however, one must utilize β and α of Figure 5-4 and have an estimate of the roll rate p (i.e., \dot{x}_4). The roll is estimated by the time to go through a revolution. Revolution, as used here, means the time between the same star's passing over the same reticle slot in sequence.

Hence, using two stars, one can isolate the average spin axis as lying along one of the intersections of the two cones. The correct solution can be readily determined by the time interval between Star No. 1 and Star No. 2 reticle slot passages plus the knowledge of p . Note that the direction of rotation is established by which star has the smallest time for reticle slot passage.

This summarizes the mathematical formulation of the problem. The formulation is simple and results in extremely fast calculations on the IBM 7094 computer.

In order to gain some insight into possible problems with the mathematical formulation, a digital computer simulation was made. In the simulation, ideal star passage times for given input conditions were calculated. The dynamic model used allowed introduction of nonsymmetric inertias as well as a simulation of a "nutation" damper. The results here will include samples of the effect of inertial asymmetry, only. Available time did not permit data to be gathered on the influence of a damper.

The simulation objectives were:

- a. Demonstrate how well the simple body dynamics represented a more accurate model over short time periods.
- b. Demonstrate that the approximate solution gave sufficient accuracy to insure convergence.

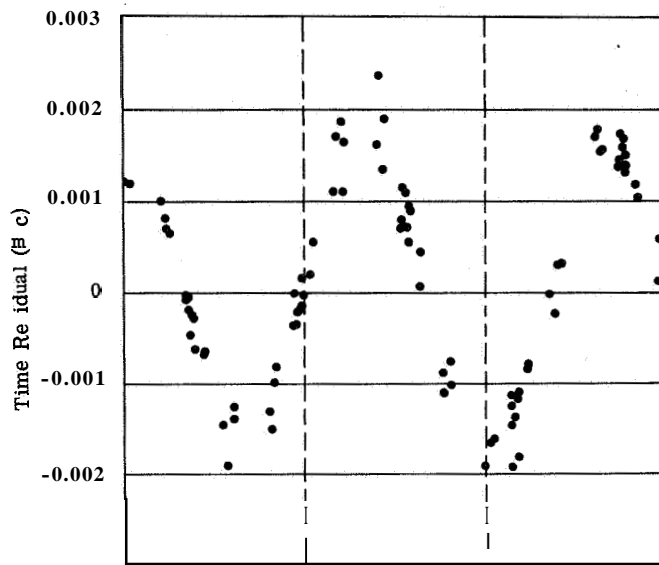
- c. Gain an understanding of how the residual time histories vary with the various real model parameters. That is, where the simplified model is known to disagree with the real model.

Figure 5-6 is a typical illustration of the time residuals for a case where the actual and simulated models were exact. The spin rate was defined to be 100 rpm for all the results shown. In this instance no problem was encountered with convergence for any of the cases tested. Precession cone angles, of the actual model, of varying values up to a few degrees resulted in data similar to that presented. A note should be added that only in the event that the vehicle is precessing can one estimate the inertia ratio J_s/J_{ns} . No problems were incurred in estimating this parameter. Figure 5-6 is also typical of what was obtained (as would be expected) for any real model so long as the precession cone angle was zero.

The quantities shown at the bottom of the figure are differences between the estimated state variables, following a few iterations of the MLE procedure, and the state variables used to compute the simulated star passage time. As is seen for this case and as was true for all of the cases tested, the differences are very small for data taken over only five revolutions of the satellite. Thus, a very precise measure of the vehicle attitude is possible in a short time period when the model agrees with the actual vehicle.

Figure 5-7 illustrates an example in which an inertial asymmetry of 0.01 percent was arbitrarily introduced. Also, the initial angle between the angular velocity and angular momentum vectors was set at 1 degree. For this example, we note considerably larger residuals as well as a periodic error. This should certainly be expected, as the motion of the actual spacecraft cannot be described by the model. The accuracy of the estimate is noted to be considerably worse than the corresponding data on the previous figure. Errors in attitude of milliradians exist in this case.

Figure 5-8 shows a similar case except for a larger variation in the inertial asymmetry (10 percent). In this instance the residuals are still of the same



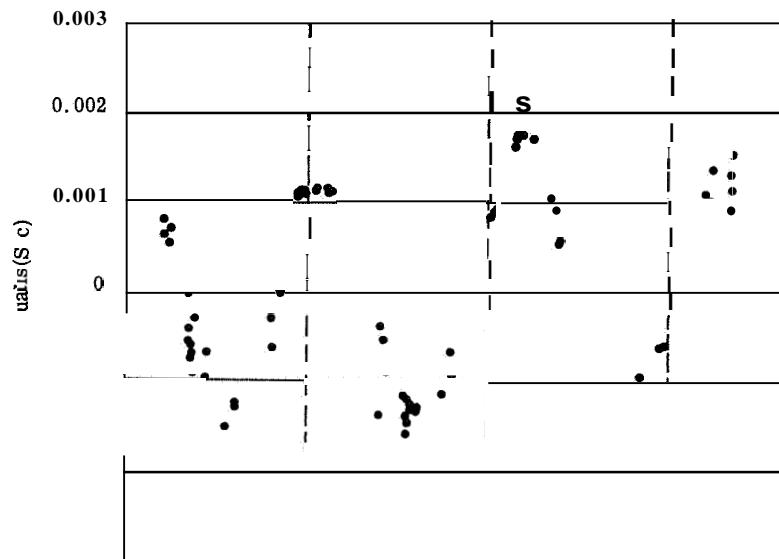
$\bar{X} - \bar{X}_x$ (6 DATA PASSES)

$\theta = 2.01$ MILLIRAD, $\omega_1 = -2.87$ MILLIRAD/SEC, $\beta = -1.62$ MILLIRAD

$\psi = 16.90$ MILLIRAD, $\omega_2 = 26.2$ MILLIRAD/SEC, $\alpha = 13.50$ MILLIRAD

$\phi = 2.13$ MILLIRAD, $\omega_3 = -183.71$ MILLIRAD/SEC, $\Sigma = 2.01$ MILLIRAD

Figure 5-7 Residual Time History for an Imperfect Model
(Initial Cone Angle, 0.0190 Inertial Asymmetry)



$e = 1.05$ MILLIRAD, $\omega_1 = 0.47$ MILLIRAD/SEC, $\beta = -0.75$ MILLIRAD

$\phi = 17.3$ MILLIRAD, $\omega_2 = -21.00$ MILLIRAD/SEC, $\alpha = 11.7$ MILLIRAD

$\psi = -3.45$ MILLIRAD, $\omega_3 = -173.37$ MILLIRAD/SEC, $\Sigma = -0.77$ MILLIRAD

Figure 5-8 Residual Time History for an Imperfect Model
(Initial CME Angle, 10% Inertial Asymmetry)

approximate magnitude as in the previous case. However, the time history of the residuals is different. The accuracy of the estimate is about the same as for the previous case.

A remark should be made that convergence was not achieved in these last two examples when an attempt was made to estimate the moment-of-inertia ratio. This is readily understood if one analyzes the effect of the moment-of-inertia ratio on the dynamic motion. A detailed analysis was not made since obviously one could correct the model by going to a slightly more complex formulation.

These two examples illustrate that the magnitude of the initial angle between the angular velocity and angular momentum vectors is the dominating influence. Since the values assumed are large for a spacecraft with a well-designed nutation damper, it is reasonable to expect that the simplified model would be appropriate for a suitably designed spinning spacecraft.

Also, a large issue should not be made of the simple versus more realistic models of the dynamics. Should the need arise for a more accurate model, it is reasonably obvious that one could do this with corresponding success. Several steps of increasing complexity were considered; however, none have yet been implemented. The only real problem of the more exact model is that the computation time for the estimate will increase.

From the study made to date one can tentatively conclude that:

1. The attitude and rates of a spinning body can be estimated to near exact values by using an appropriately designed star detector and state estimation technique.
2. The simplified model is appropriate for very small precession angles as would be incurred by a satellite with a "nutation" damper.
3. The Maximum-Likelihood procedure appears to have negligible convergence problems. Hence, tolerances on preflight alignment or the accuracy of the initial estimate are not significant factors in the success of the technique.

The results shown are very similar to those encountered in orbit determination. The two problems are of course similar and the analogy is not surprising.

SECTION 6
EXPERIMENT COST

A preliminary cost estimate of the proposed NavSat Experimental Satellite has been prepared for planning purposes. The costs shown are ROM estimates only and are intended to be compatible with the Program Plan shown in Section 2. The basic (SCS) cost is based upon one satellite to be used for both the qualification and the flight model. The assumption has also been made that the satellite be included in a regular production schedule.

Cost Schedule A Cost Estimates for One Satellite
(ROM Estimate)

| <u>Item No.</u> | <u>Description</u> | <u>cost</u> <u>(Thousands of Dollars></u> |
|-----------------|-------------------------------------|---|
| 1 | Basic Satellite | 375 |
| 2 | Engineering and Drawings | 420 |
| 3 | Manufacturing | 100 |
| 4 | Development Test | 60 |
| 5 | Qualification Test | 30 |
| 6 | Retrofit | 100 |
| 7 | Acceptance Test | 20 |
| 8 | Star Detector (See Schedule B) | 305 |
| 9 | Nutation Damper (See Schedule C) | 51 |
| 10 | Launch Operations | 50 |
| 11 | Orbit Operation | 250 |
| 12 | Administration | 100 |
| | TOTAL COST | <u>\$ 1.861</u> |

Schedule B NavSat Star Detector (ROM Estimate)

| Item | Labor Cost | Plus 24% Fringe | Plus 85% Burden | Materials Repro Computer | Sub Total | Plus 8.7% G & A | Total* |
|---|--|-----------------|-----------------|--|-----------|-----------------|----------------|
| 1. Design, fabricate, assemble & test: (a) One each, Mock-up Qual Model Flight Model | 19,000 (Electron.) 3,300 (Thermal) <u>42,000 (All Other)</u> 64,300 | 79,732 | 147,504 | 12,000 (Elec.) 1,800 (Comp.) <u>35,400</u> 49,200 | 196,700 | 213,813 | 213,813 |
| (b) Bench Check-out Equipment | 14,000 | 17,360 | 32,116 | 3,600 | 38,716 | 38,822 | 88,822 |
| 2 Experiment Analysis & Data Handling | 21,000 | 26,040 | 48,174 | -- | 48,174 | 82,366 | 82,366 |
| TOTALS | 99 00 | 123,132 | 227,794 | 52,800 | 280,890 | 305,000 | <u>305,000</u> |

* Does not include fee

Schedule C Nutation Damper

The following ROM Cost Estimate was provided by GM Defense Research Laboratories.

ESTIMATED PRICE BREAKDOWN

Development of a Circular Constraint Fluid-Type
Passive Nutation Damper for a Navigation Satellite

| | <u>Estimated Hours</u> | <u>Estimated Amount</u> |
|-------------------------------|----------------------------|-----------------------------|
| Direct Labor: | | |
| Engineering | 1,545 | \$ 10,430 |
| Drafting | 106 | 528 |
| Technician | 525 | 2,076 |
| Fabrication | <u>330</u> | <u>1,212</u> |
| Total Direct Labor | <u>2.506</u> | 14,246 |
| Burden | | 22,794 |
| Direct Material - Outside | | 1,408 |
| Travel | | 503 |
| Computer | | <u>3,301</u> |
| Total Direct Cost and Burden | | 42,279 |
| General and Administrative | | 3,594 |
| Independent Research | | <u>846</u> |
| Total Estimated Cost | | 46,719 |
| Fixed Fee | | <u>4,672</u> |
| Total Estimated Selling Price | | \$ <u>51.391</u> |